Pontificia Universidad Católica de Chile
Facultad de Física
Instituto de Astrofísica

STOCHASTIC ION ACCELERATION BY THE ION CYCLOTRON INSTABILITY IN COLLISIONLESS PLASMAS WITH A GROWING MAGNETIC FIELD

by

Francisco Javier Ley Quinteros

Tesis presentada a la Facultad de Física de la Pontificia Universidad Católica de Chile, para optar al grado académico de Magíster en Astrofísica.

Supervisor	:	Dr. Andreas Reisenegger
Supervisor	:	Dr. Mario Riquelme
Corrector	:	Dr. Jorge Cuadra
Corrector	:	Dr. Pablo Moya

August 20, 2018

Santiago, Chile

A mis padres

¡Ojalá nunca hubiera ido a vuestras escuelas!
La ciencia, a la que perseguí a través de las sombras
de la que esperaba, con la insensatez de la juventud,
la confirmación de mis alegrías más puras,
es lo que me ha estropeado todo

En vuestras escuelas es donde me volví tan razonable,
donde aprendí a diferenciarme
de manera fundamental de lo que me rodea;
ahora estoy aislado entre la hermosura del mundo
he sido así expulsado del jardín de la Naturaleza,
donde crecía y florecía, y me agosto al sol de medio día

-Hölderlin

Agradecimientos

“Comienzo con una palabra que todos los hombres, desde que el hombre es hombre, han proferido: gracias...”

Aún cuando las palabras muchas veces no son suficientes para expresar sentimientos tan propios como lo es la gratitud, quisiera expresar aquí mi profundo agradecimiento a todos quienes fueron parte de mi vida en esta etapa de mi vida académica.

Parto agradeciendo a los dos profes guía que tuve. Gracias a Mario, por invitarme a colaborar en este proyecto, por introducirme al vasto mundo de la astrofísica de plasmas, y su gran labor y paciencia como mi profesor guía. Cuánto aprendí y crecí este tiempo bajo su tutela es invaluable. Su humildad, talento y tremenda voluntad para enseñar y explicar me acompañarán siempre, y servirán de inspiración constante en el camino de la Ciencia. Gracias a Andreas, por aceptar mi deseo de trabajar con él, por acogerme a la mitad del magíster, por darme la libertad de hacer un proyecto en colaboración con Mario. Gracias también por su enorme guía en los trabajos en conjunto, su entusiasmo por enseñar y su tremenda pedagogía; la manera única de pensar la física es una de las cosas que siempre recordaré y llevaré conmigo como inspiración por el intrincado rumbo de la astrofísica teórica. Gracias también a Franz, Claudio y Johannes, por ser los primeros que me abrieron las puertas en el magíster, su excelente disposición al trabajar y su comprensión respecto a mi cambio de rumbo. A ellos les debo muchísimo de lo que soy ahora, como científico y como persona.

Y antes, agradecezco profundamente a Paulina Lira y Mario Hamuy, quienes me guiaron en mis primeros pasos en la investigación científica, al salir de pregrado, con tanta paciencia y dedicación. A Álvaro Núñez y Gonzalo Palma, por dictar los cursos que más disfruté y a Gonzalo además por ser una figura académica a seguir. Agradezco también a profesores que me marcaron y formaron como ser humano y como ciudadano: gracias a Belfor Aguayo Santis, Alejandro Vargas Cornejo (“Paganini”), Luis Arancibia, Pedro Lazo y Manuel “Barrilito” Pérez. Gracias también a mis profes de inglés, Carolina Santander; sus clases un oasis en medio de la vorágine beauchefiana, y Fran y Brendan; esenciales en la aventura que pronto se inicia.

Una de las cosas más lindas de haber elegido este camino han sido, sin ninguna duda, los amigos. Aquellos que siempre han estado, en los momentos más felices, y en los más tristes. Gracias a mis vioh’s Byron, Eva, Jane, Josu, Jotapel, Nico Meza y Pesce por tantas risas, juntas, matraca, apoyo, cariño y amor. Gracias a los chicocos saliteros Basti, Bica, Bryan, Camilo, Comi, Coni, Fefo, Gattin, Guille, Isma, JG, Jose Limache, Leo, Mauro, Nico Soto, Panchito, Pelo, Pleiva, Suafle por hacer de la salita un lugar amado y acogedor. Gracias a Alfredo, Bas, Checo, Chela, Chico, Claudio, Gato, Roberto, Wolf, Zolezzi, Erick y Pablito Azurduy, por tantos viernes, chelas, terraceos y risas en Beauchef. Gracias infinitas a mis amados workshoppers David, Kike, Lala, Nico y Pablo, por tanto cariño, risas, workshops y karaokes. Millones de gracias a mi oficina, la Bellaka: Camilo, Felipe, Lore, Marilyn, Paz y Ricardo, por hacer de la oficina algo más que eso; un lugar ameno, acogedor, donde pudimos reír y formar lazos de amistad. Gracias finalmente a los de siempre, a los de toda la vida, gracias Matías, Pingo y Aníbal, por estar ahí conmigo siempre, desde el colegio, y gracias Andrés, por ser mi compadre y apañarme en absolutamente todas. A todos ustedes, estarán siempre en mi corazón.

Finalmente, me reservo el final para dar las gracias a mi familia. A mi Madre y a mi Padre, por hacer siempre todo y más por mí, para que pudiera estudiar lo que siempre quise, por creer en mí siempre y apoyarme de manera incondicional. Me siento afortunado y orgulloso de ser su hijo. A Isabel, mi compañera de vida, profundamente agradecido de tu amor, tu cariño y comprensión. En las buenas, en las malas y en las peores, siempre. Y por estar a mi lado en la aventura que pronto comienza. Nada de lo que pueda expresar aquí podrá reflejar la inmensa gratitud que les tengo. Los amo.

Incidentalmente, agradezco la música que me acompañó en este viaje: A J.S. Bach, por brindarme claridad y orden mental en tiempos de confusión, a L. Van Beethoven, fuente infinita de inspiración, a S. Rachmanninoff, por darme bríos y carácter para continuar, y a John Sheppard, Thomas Tallis y Samuel Barber, por contenerme y arrullarme en los momentos más difíciles.

Powered@NLHPC: Esta investigación fue parcialmente apoyada por la infraestructura de supercómputo del NLHPC (ECM-02). Agradecimientos a Proyecto Regular FONDECYT 1150411.

Contents

List of Tables

List of Figures

Resumen

Las partículas no térmicas de alta energía (es decir, cuyas energías exceden la energía promedio en el espacio circundante por varios órdenes de magnitud, conocidas como "rayos cósmicos") constituyen una componente omnipresente del Universo en todas las escalas, desde el Sistema Solar hasta cúmulos de galaxias. El problema de cómo estas partículas alcanzan estas energías ha sido un tópico de gran interés desde su descubrimiento.

La aceleración de Fermi es uno de los mecanismos usualmente mencionados para explicar las leyes de potencia que se observan en las distribuciones de energía de estas partículas. La aceleración de Fermi de primer orden es comúnmente aludida como el principal mecanismo presente en ondas de choque relativistas (v.g. Ondas de choque en remanentes de supernovas). La aceleración de Fermi de segundo orden, también llamada aceleración estocástica, puede ser un mecanismo eficiente en ambientes astrofísicos más generales, siempre que el plasma posea un nivel considerable de turbulencia, como es usual esperar en astrofísica.

En esta tesis se estudia la aceleración de iones en un plasma no colisional, magnetizado y sujeto a un cizalle permanente que a su vez amplifica el campo magnético. A medida que el campo magnético se amplifica, se generan anisotropías de presión ($p_{\perp,i} > p_{\|,i}$, donde $p_{\perp,i}$, $p_{\|,i}$ son la presión de los iones perpendicular y paralela a la dirección del campo magnético, respectivamente) a causa de la invariancia adiabática del momento magnético de los iones ($\mu_i \propto p_{i,\perp}/B$, donde μ_i es el momento magnético de los iones y B es el campo magnético). Esta anisotropía gatilla finalmente inesta-

bilidades cinéticas en el plasma en escala del radio de Larmor de las partículas, como las inestabilidades ion-ciclotrón (IC) y mirror, en donde la primera empieza a interactuar con los iones de manera resonante, produciendo sucesivos cambios aleatorios en el ángulo formado por la velocidad de las partículas y el campo magnético de fondo ("pitch-angle scattering"). Este proceso puede interpretarse como estocástico dado que las partículas sufren interacciones sucesivas y no correlacionadas con ondas IC con velocidades de fase aleatorias.

Se realizan simulaciones de plasma *particle in cell* que permiten estudiar el régimen cinético del plasma (esto es, cuando las escalas características del sistema son del orden del radio de Larmor de las partículas) de manera autoconsistente, considerando la interacción no lineal onda-partícula y el régimen saturado y cuasi-estacionario de las inestabilidades. Se obtiene que la interacción entre las partículas y los modos IC puede acelerar iones a energías no térmicas eficientemente, y la eficiencia de la aceleración depende del valor inicial de $\beta_i = 8\pi p_i/B^2$. Cuando $\beta_i \lesssim 1$ la distribución de energía final de los iones puede describirse como una componente térmica más una cola con una ley de potencia de índice espectral $\alpha_s = 3.4$. Para valores más grandes de β_i, la eficiencia decrece y α_s crece gradualmente. Las implicancias de estos resultados se discuten en el contexto de ambientes astrofísicos de baja colisionalidad (por ej. en el agujero negro supermasivo Sgr A*, en el centro de nuestra galaxia) y en el rol que podrían jugar como partículas energéticas semilla en procesos de reaceleración por ondas de choque.

Abstract

High-energy charged particles (i.e. whose energies exceed the average energy of the ones in their surroundings by many orders of magnitude, commonly known as "cosmic rays") constitute an ubiquitous component of the Universe at all scales from the Solar System to cluster of galaxies. The question about how these particles achieve those large energies has been a topic of great interest since their discovery.

Fermi acceleration is one of the mechanisms usually invoked to explain the observed power laws in the energy distribution of particles. While first-order Fermi acceleration (also known as diffusive shock acceleration), is commonly regarded as the main mechanism active in relativistic shock waves (e.g. supernova remnant shocks), second-order Fermi acceleration, also called stochastic acceleration, can be an efficient mechanism in more general astrophysical environments, as long as the plasma possesses a considerable level of turbulence, as is usually the case in astrophysics.

In this thesis we study the acceleration of ions in a collisionless, magnetized plasma subject to a permanent shear motion, which continuously amplifies the magnetic field. As the magnetic field is amplified by the shear, a pressure anisotropy ($p_{\perp,i} > p_{\|,i}$, where $p_{\perp,i}$, $p_{\|,i}$ are the ion pressure perpendicular and parallel to the magnetic field, respectively) is generated by the adiabatic invariance of the ion magnetic moment ($\mu_i \propto p_{i,\perp}/B$, where μ_i is the ion magnetic moment and B is the ambient magnetic field). This anisotropy ultimately triggers Larmor radius scale instabilities, namely the ion-cyclotron (IC) and mirror instabilities, where the former starts to interact with the ions resonantly and efficiently pitch-angle scatters

them. The process can be interpreted as stochastic as long as the particle undergoes successive, uncorrelated scattering with IC waves of random phase velocities.

We perform particle-in-cell plasma simulations which allow us to study the kinetic regime of the plasma (i.e. when the characteristic scales of the system are of the order of the Larmor radius of the particles) in a self-consistent way, considering the nonlinear wave-particle interaction and the long-term, saturated regime of the instabilities. We obtain that the scattering by IC modes can effectively accelerate ions to non-thermal energies, and the efficiency of acceleration depends on the initial $\beta_i = 8\pi p_i/B^2$, where p_i is the ion pressure. When $\beta_i \lesssim 1$ the final ion energy distribution can be described by a thermal component plus a power-law tail with spectral index $\alpha_s = 3.4$. For larger values of β_i the efficiency steadily decrease and α_s steadily increase. The implications of these results are discussed in the context of low-collisionality astrophysical environments (e.g. Sgr A*) and the role that these accelerated ions may have as seed energetic particles in reacceleration processes by shocks.

Chapter 1

Introduction

It has been 69 years since the seminal paper by Fermi [1] about a physical mechanism to efficiently accelerate the very energetic charged particles observed to pervade Earth's atmosphere from all directions in the sky. Although known since the times of Coulomb back in 1785, it was not until 1912 when Hess suggested that these particles should have a cosmic origin. Now we know that these particles, called "cosmic rays", not only pervade the Earth but all the space around ranging from the interstellar medium (ISM) [2] to the intergalactic medium (IGM), for the ultra high energy cosmic rays [3].

Cosmic rays present many interesting features in terms of their origin, composition, abundances, acceleration and propagation, as well as in their role in the evolution of the Galaxy, which continue to be the focus of active research these days. In particular, the question about the physical mechanisms capable to energize these particles from ~ 1 GeV to $\sim 10^{12}$ GeV still generates debate among scientists.

There are three main mechanisms usually invoked in order to explain how the acceleration process happens. These are the first and second-order Fermi mechanisms, usually called diffusive shock acceleration (DSA) and stochastic acceleration, respectively, and magnetic reconnection. DSA [4, 5] has been investigated in great detail since it naturally predicts a power-law behavior $\propto E^{-\alpha}$ for the energy distribution of the particles, with a spectral index independent of the microphysics of the scattering processes and in relatively good agreement with the observed particle spectra; whereas DSA predicts a spectral index of $\alpha_{\rm DSA} \sim 2$ at the source[1], the observed index here at Earth is around $\alpha_{\rm obs} \sim 2.6$ (see e.g. [6]). This disagreement cannot be neglected and further investigation around DSA has extensively been carried out both analytically and numerically in order to resolve this and other tensions. Efforts in this line have been focused on studying, for instance, the reaction that accelerated particles exert on the shock itself, when their pressure and energy density become comparable with those of the system, giving rise to non-linear theories of DSA. These theories also consider the amplification of the background magnetic field via plasma instabilities triggered by the very process of acceleration, thus motivating further investigation of the role plasma physics has in the whole process of cosmic acceleration (see [7]). Another physical explanation for the difference between the observed spectral index and the simplest DSA prediction is the effect of the escape of CRs from the Galaxy, which is naturally more effective as the energy of particles increases.

On the other hand, stochastic acceleration, the motivation of this thesis, emerges from the interaction between particles and randomly moving plasma waves generated by turbulence. In this process, on average, there is a net energy gain by the particles, whose efficiency is proportional to $\propto (V/c)^2$, where V the phase velocity of the wave[2]. Due to its second order dependence on velocity, the rate of acceleration is typically slower than the acceleration by shocks, which is proportional to V/c. Also, in contrast to the DSA, the spectral indices produced by the stochastic acceleration vary significantly depending on the characteristics of the system. Thus the fairly homogeneous spectral index of cosmic rays over several orders of magnitude in energy does not appear to be a natural feature of this acceleration process.

[1]See Appendix C for an explanation of the basics of the DSA process

[2]See Appendix C for a brief description of the basis of the stochastic acceleration process.

Nevertheless, as shown in this thesis, stochastic acceleration can be efficient under certain conditions, especially in systems where the presence of magnetohydrodynamic (MHD) turbulence is significant.

1.1 Observational features of Cosmic Rays

Here at Earth cosmic rays (CRs) can be detected directly by several facilities that include stratospheric balloon flights, small satellites and the International Space Station (ISS) [8], while others are ground-based, like the Pierre Auger Observatory and AGASA. A cosmic ray energy spectrum gathering many experiments can be seen in figure 1.1. We can see that it is characterized mainly by a broken power-law with an overall spectral index[3] of $\alpha_s \sim 2.6$, in which from 1 to $3{\times}10^6$ GeV the composition is mainly protons.

It is interesting to note how the spectrum declines at lower energies around 30 GeV and below. This is caused by the presence of a magnetized, turbulent solar wind that interacts with CRs at these energies, making their flux and energies fluctuate over time along with the Sun's cycles, and preventing low-energy particles from reaching Earth. This feature is known as the solar modulation of CRs (see e.g. [9] for a review).

At energies around 3×10^6 GeV the power-law turns over to a steeper slope, changing its spectral index from ~ 2.6 to ~ 3.1. This feature is called the "*knee*", and the presence of this break should represent a transition to a different population of CRs. In fact, there is evidence that the CRs have a different chemical composition in this region of the spectrum, with a trend that favors heavier nuclei towards higher energies [10]. Additionally, the change in the slope suggests that the initial mechanism of acceleration that produced the initial spectral index has reached its maximum possible energy, placing its cutoff around this point. These two aspects

[3] The positive spectral index is adopted, so $dN/dE \propto E^{-\alpha_s}$.

give rise to the theory that up to the knee all CR are produced within the Galaxy, and, as is pointed out in [7] and [11], a knee would naturally arise as the superposition of several cutoffs in the spectra of each individual species being accelerated[4].

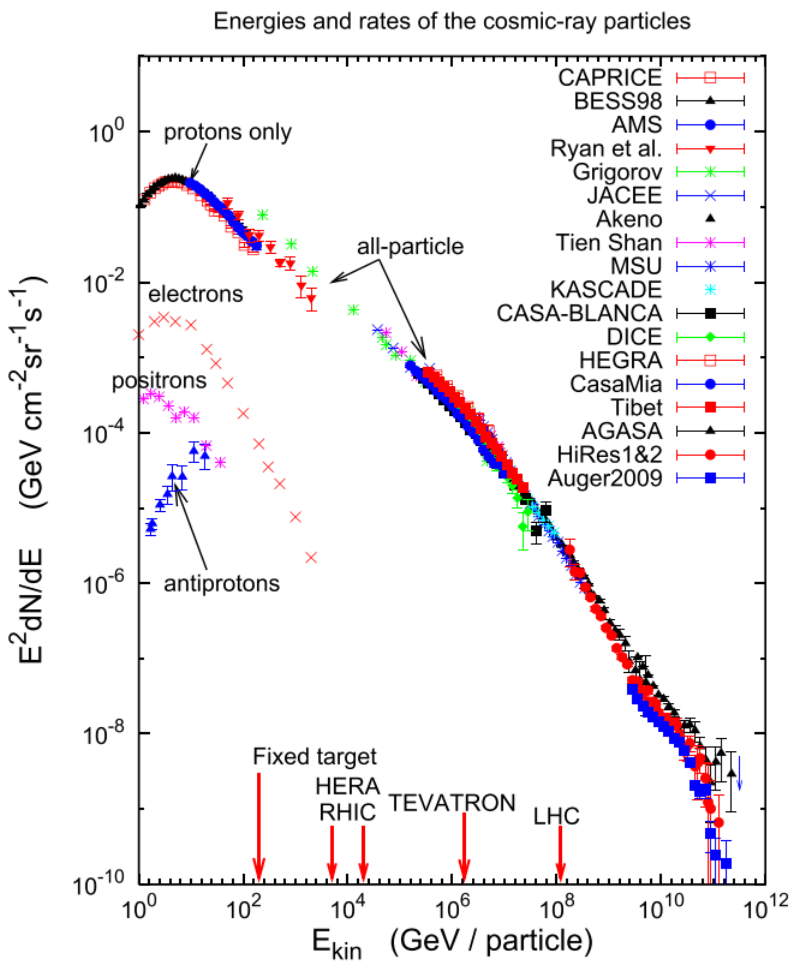

Figure 1.1: Cosmic ray spectrum for several species: protons, electrons, positrons and antiprotons. The maximum energies of some laboratory accelerators is included for reference (red arrows at the bottom). Figure taken from Zweibel, 2013 [6].

[4]In this argument it is assumed that the acceleration process depends on the rigidity of the species $R = R_{L,j}B$, where $R_{L,j}$ is the Larmor radius of the species j and B is the ambient magnetic field. As $R_{L,j}$ depends on the atomic number Z, each different species will have a slightly different energy cutoff ([7]).

Going further, at energies around $\sim 10^9$ GeV another break in the slope arises in which it flattens again to a spectral index of 2.7, a feature called the "*ankle*" . At these energies, the particles have a Larmor radius of the order of kpc, so here it is almost impossible for the Galactic magnetic field $\sim 1.6\ \mu G$ to confine these CR within the Galaxy, so they are expected to have an extragalactic origin.

The electron spectrum can also be seen in figure 1.1. They constitute a small fraction of the total number (~1-2%), and present a spectrum whose slope is steeper than the overall CR spectrum, due to their strong radiative losses, mainly via synchrotron and inverse Compton.

Indirect detections, which use the non-thermal radiation produced by energetic particles, constitute another valuable tool to study CRs. As they interact with matter, magnetic fields, and radiation fields, CRs can emit photons from radio frequencies (synchrotron from electrons) to TeV gamma rays (mainly due to inverse Compton from electrons, and neutral pion decay due to CR protons interacting with the ISM[5]). In contrast to the case of the electrically charged CRs, the trajectories of these photons are not affected by the bending caused by magnetic fields (as it is the case of the charged CRs), allowing in principle to spot the acceleration sites of CRs. In this context, significant progress in our understanding of the origin of CRs has been achieved in the last decade with observatories like VLA (radio), Chandra (X rays), and Fermi-LAT (gamma rays). TeV gamma rays have also become an important messenger thanks to the advent of imaging atmospheric Cherenkov twithelescopes (IACT) like HESS, and of water Cherenkov tank telescopes like HAWC.

The combined power of these observatories has allowed to test in great detail the idea that CRs with energies up to the knee ($\sim$ PeV) are accelerated by shock waves in galactic supernova remnants (SNRs). Although these observations have shown that this hypothesis is at least partially true (see e.g. [14]), it is still unclear whether

[5]This type of interaction can also generate significant neutrino emission, which recently has become another important messenger in the study of CRs [12, 13]

CRs with energy $\lesssim 1$ PeV can be *completely* explained by this paradigm, or if there is still room for other acceleration sites and mechanisms. Furthermore, to date there is no convincing observational evidence that CR acceleration in SNRs can reach PeV energies [15]. Major advances regarding these issues are expected in the next decade with the Cherenkov Telescope Array (CTA), an IACT observatory whose Southern (and larger) array will be located in Chile (`cta-observatory.org`).

The lack of conclusive answers about the sites (and underlying physical mechanism) for CR acceleration is the main motivation for this work. In this thesis we use particle-in-cell (PIC) simulations to show that stochastic ion acceleration by ion-cyclotron (IC) plasma waves is a possibly relevant process in the context of collisionless plasmas being heated through viscosity. Although this mechanism can be realized in different astrophysical contexts, we envision it to be relevant in weakly collisional accretion disks, like the one expected around the supermassive black hole at the center of the Milky Way, Sagittarius A* (Sgr A*).

1.2 Acceleration Mechanisms

Very generally speaking, the study of CR can be divided into how they are produced and accelerated in the source, how they propagate through and interact with the ISM, and how they are detected when reaching Earth. In what follows the first of these areas will be assessed, in which the main acceleration mechanisms will be described, namely, the first and second order Fermi acceleration and magnetic reconnection.

1.2.1 Second-Order Fermi Acceleration

The original idea of Fermi [1] considered charged particles which undergo successive collisions with "magnetic clouds" or "magnetic mirrors" through the interstellar medium. This clouds can be thought of some inhomogeneities in the magnetic field of the Galaxy moving with velocity V, and the particle and the clouds collide with each other in a stochastic manner. Fermi showed that, even though at each encounter the particles could lose or gain energy, on average they end up gaining energy, with an energy increase in each encounter equal to[6],

$$\left\langle \frac{\Delta E}{E} \right\rangle = \frac{8}{3}\left(\frac{V}{c}\right)^2, \tag{1.1}$$

so it is second-order in velocity. It can also be shown that this process leads to a power-law energy distribution for the particles with a spectral index that depends on the specific parameters of the particular source.

Even when second-order Fermi acceleration is an efficient mechanism for energizing particles, when applied to CR in Fermi's original approach, it suffers some severe problems:

- First of all, as it is assumed that the energy comes from the interstellar magnetic clouds, the typical velocities they possess are fairly small compared with the speed of light, $V \sim 10^{-4}c$, so the second-order dependence would give a really tiny amount of energy in each encounter, requiring a large number of scatterings to achieve the observed energies.

- Along with the acceleration process there will always be ionization losses that take energy from the accelerated particles at a rate that depends on their kinetic energy, as at lower energies the cross section is higher. This could prevent the particles to be accelerated from lower energies, or even from the thermal bath. Consequently, there should be another mechanism that injects particles with energies higher than the point where the acceleration rate is equal to the ionization energy loss rate, thus allowing further acceleration.

[6]For a derivation of this result and the power-law energy distribution that this process produces, see Appendix C.

- There is no hint or prediction in the theory telling us that the spectral index should be obtained is 2.6 irrespective of the source or any given parameters. In principle the spectral index can take any value.

Nevertheless, in modern versions of stochastic acceleration, the particles can interact with a variety of plasma waves present in any astrophysical environment with a certain level of turbulence. The particles can gain energy by being scattered resonantly by the waves in a stochastic fashion where, depending on the parameters of the plasma, reasonable rates of acceleration can be obtained, as we shall see in this work.

1.2.2 First-Order Fermi Acceleration

Until the seminal works of Bell [4] and Blandford & Ostriker in 1978 [5] there were no relevant advances in theories of acceleration. In these works, efforts were put to describe a mechanism whose energy gain was first-order in velocity, and that mechanism was found in the context of shock waves like the ones SNRs produce with the surrounding interstellar medium. This process, also called Diffusive Shock Acceleration (DSA), became a cornerstone in acceleration mechanisms because of its efficiency and the prediction of a spectral index of ~ 2 independent of the microphysics of the acceleration.

In this process, the particles are now successively crossing a shock front, and in each of these crossings they are scattered by the motion of the magnetized fluid present withinturbulence the shock and they will gain energy every time they cross it, upstream or downstream. It can be shown that the energy gain in this case is[7],

$$\left\langle \frac{\Delta E}{E} \right\rangle = \frac{4}{3}\left(\frac{V}{c}\right) \tag{1.2}$$

[7]For a derivation of this result and the spectral index of the power-law energy distribution, see Appendix C.

So now it is a process that is first-order in velocity. Strikingly, this process predicts a power-law energy distribution with spectral index equal to $\alpha_s = 2$, independent of the microphysics going on in the system. This definite value of the spectral index provides a nice physical justification for the observed spectral index in different astrophysical environments.

Even when this process constitutes a major improvement over the second-order Fermi mechanism, an important comment deserves to be made with respect to the assumptions and limitations of this initial version of DSA. In the derivation of eq. 1.2 it is assumed the condition of isotropization of the velocity distribution of particles as an essential condition for the process. This assumption is valid only in the nonrelativistic limit, $V \ll 1$. Secondly, it is also assumed that the particles already had high energies so that they do not lose energy through collisions with thermal particles neither be deflected by them, only by magnetic fields. This issue is known as the *injection problem* and even in more sophisticated versions of DSA it is not completely solved and an initial population of already energized particles is needed. This is one of the problems for which this work attempts to give a plausible solution. Lastly, this derivation was performed in the "test particles" approach, in which the accelerated particles do not exert a backreaction on the shock. This is expected to happen, however, as the energization process would eventually generate pressures of the accelerated particles comparable to the kinetic pressures of the incoming fluid. This process inevitably changes the properties of the shock and the whole mechanism becomes intrinsically nonlinear. In recent years there have been a lot of efforts to study the nonlinear behavior of DSA (NLDSA) [16], the injection problem [17, 18] and the geometry of the shock [19].

Finally, to put this in context, it is expected that the astrophysical environments in which these processes of particle acceleration take place are, in general, in a plasma state with an important large-scale magnetic field, they are strongly magnetized plasmas with very low densities and high temperatures. In these conditions, binary interactions between particles are not important or not relevant at all, so these plasmas cannot reach thermodynamic equilibrium easily and energy can remain stored in separated populations. Plasmas of this kind are called weakly-collisional or collisionless. In order to reach equilibrium, these plasmas naturally generate electromagnetic waves which can survive for many cyclotron periods, and if a sufficient number of wave modes manage to exist simultaneously, the plasma enters into a turbulent state. Indeed, the processes that mediate the microphysics of Fermi acceleration, both first and second order, are this kind of waves and their interactions with particles, embedded in these turbulent, collisionless plasmas. Examples of this kind of plasmas in astrophysics are, apart from SNR shocks, low-luminosity accretion disks (e.g. Sgr A^* in the center of the Galaxy), the intra-cluster medium, and the heliosphere.

1.2.3 Magnetic Reconnection

The process of magnetic reconnection is completely different from first- and second-order Fermi mechanisms but nevertheless it constitutes a plausible mechanism for accelerating particles in astrophysical environments. Magnetic reconnection is the process in which magnetic field lines reorganize their topology along with the release and dissipation of the magnetic energy into plasma energy. It has usually been described in the magnetohydrodynamic (MHD) regime[8]. In this regime, magnetic reconnection occurs when the frozen magnetic flux condition breaks down on timescales much shorter than the plasma diffusion time[20]. This breakdown gives rise to an electric field capable of accelerating the particles. In astrophysical environments this process happen regularly whenever two different plasmas with different magnetic flux configurations come into contact. Examples where magnetic reconnection could be present are solar flares [21], pulsar wind nebulae [22, 23, 24], γ-ray

[8]Although it is not restricted to MHD; in collisionless plasmas or in non-MHD regimes it can develop as well, see e.g. [20].

bursts[25, 26] and accretion flows around supermassive black holes [27].

Magnetic reconnection is commonly invoked as the underlying mechanism that powers explosive, flaring astrophysical phenomena. The released magnetic energy can result in heating and acceleration of particles, which in turn becomes relevant in order to understand the different emission of these sources. For instance, in the case of the supermassive black hole in the Galaxy, Sgr A*, magnetic reconnection in the trans-relativistic case[9] could be relevant for explaining its flaring state [29]. Magnetic reconnection in the ultra-relativistic regime has also been invoked as a plausible explanation for the gamma-ray flares in the Crab Nebula by means of the emission of particles being accelerated by this mechanism [30].

Another interesting feature of magnetic reconnection is the interplay it develops with turbulence. This is especially important in astrophysical environments, where Reynolds numbers are usually high, so turbulence is expected to be present. The turbulence can arise even from the reconnection itself, so this state is usually called turbulent reconnection[31]. In this turbulent state, particle acceleration can also be triggered, and even first- and second-order Fermi acceleration could be present.[32, 31].

1.3 Outline of the Thesis

This thesis is organized as follows. In chapter 2 we describe the numerical framework and the specific setup we used in this study. An overview of the particle-in-cell method is provided followed by the setup and initial configuration of the simulations we ran for this study. In chapter 3 we present the results of the simulations, in which we show how the plasma microinstabilities are triggered and develop, how the energy distribution of ions develop a nonthermal power-law tail of stochastically

[9]the trans-relativistic regime is defined when the magnetization parameter, defined as the ratio of the magnetic energy density to the enthalpy density is of the order of unity, see [28].

accelerated ions and the way these ions are gaining energy through the interaction with these instabilities. We finish this section with a discussion of the astrophysical implications of this phenomenon and some guidelines for future work. Finally, in chapter 4 we provide the conclusion of this work.

Chapter 2

Simulation Setup

2.1 Collisionless Plasmas

As we mentioned in section 1.2.2, in this thesis we will study collisionless plasmas, which constitute a suitable environment for particle acceleration in the Universe. A collisionless plasma is characterized by the absence of Coulomb binary interaction, so the dominant phenomena are collective behaviors of the plasma. The collisionless regime occurs when the mean free path between Coulomb collisions is much larger than the scales of the system and when the timescale of Coulomb collisions is much larger than the characteristic timescale of the plasma; this could correspond, for instance, to the time scale at which energy is being dissipated by some MHD turbulence.

The evolution of a collisionless plasma can be described by the Vlasov equation:

$$\frac{\partial f}{\partial t} + \frac{\vec{p}}{\gamma m} \cdot \frac{\partial f}{\partial \vec{r}} + q\left(\vec{E} + \frac{\vec{v} \times \vec{B}}{c}\right) \cdot \frac{\partial f}{\partial \vec{p}} = 0, \tag{2.1}$$

which is nothing more than the conservation of density in phase-space in absence of collisions. Here, $f(\vec{r}, \vec{v}, t)$ is the distribution function of the particles in the six-dimensional phase-space and time, $\vec{r}$ the position and $\vec{p} = \gamma m \vec{v}$ the momentum, and

q the electric charge. The electromagnetic fields $\vec{E}, \vec{B}$ are evolved with Maxwell's equations:

$$\nabla \cdot \vec{E} = 4\pi\rho \tag{2.2}$$

$$\nabla \cdot \vec{B} = 0 \tag{2.3}$$

$$c\nabla \times \vec{E} = -\frac{\partial \vec{B}}{\partial t} \tag{2.4}$$

$$c\nabla \times \vec{B} = 4\pi\vec{J} + \frac{\partial \vec{E}}{\partial t}, \tag{2.5}$$

where the net charge density ρ and the current $\vec{J}$ are defined by the respective moments of the distribution function:

$$\rho(\vec{r}, t) = \sum_j q_j \int_v f_j(\vec{r}, \vec{v}, t) d\vec{v} \tag{2.6}$$

$$\vec{J}(\vec{r}, t) = \sum_j q_j \int_v \vec{v} f_j(\vec{r}, \vec{v}, t) d\vec{v}. \tag{2.7}$$

In equations 2.6 and 2.7, the sum is over all particle species and the integration is over all velocity space. Hence, Vlasov equation for $f(\vec{r}, \vec{v}, t)$ along with Maxwell's equations for the fields constitute the full set of coupled equations to describe a collisionless plasma from very first principles. As a first attempt, one would want to simulate the full evolution of Vlasov equation through all phase space. This can be done by considering phase space as a continuous fluid and then solve Vlasov equation with an appropriate scheme (being Eulerian or Lagrangian, see e.g.[33]). However, this approach is computationally too expensive for astrophysical applications for current facilities since it requires to evolve the full 6D phase space. Alternatively, this problem can be tackled by the Particle-In-Cell (PIC) method, which is computationally much less expensive, easy to implement and parallelize, and at the same time it keeps the fundamental properties of the system. In the description of the PIC method we will closely follows a recent nice review by Sironi & Cerutti [34].

2.2 Particle-In-Cell Simulations: The Essentials

The Particle-In-Cell method (PIC) [35, 36] indirectly solves Vlasov equation by a particle approach, in which the distribution function is "discretized" into several elements which we will call "macroparticles":

$$f(\vec{r}, \vec{v}, t) = \sum_p f_p(\vec{r}, \vec{v}, t). \tag{2.8}$$

Each one of this "chunks" of the distribution function represents a large amount of particles that travel through phase space near each other. Then, what PIC does is to integrate the discrete trajectories of these macroparticles using the self-consistently generated electromagnetic fields and Newton's second law. This procedure is equivalent to solve Vlasov equation by the method of characteristics, in which the characteristic curves are these macroparticle trajectories.

Given this discretization, in order to characterize these macroparticles, they are given a definite functional form which is used to determine their contribution to charge density $\rho(\vec{r}, t)$ and electric current $\vec{J}(\vec{r}, t)$. In principle, any function can be chosen. As a first attempt, we can try a delta function-like distribution:

$$f_p(\vec{r}, \vec{v}, t) = N_p \delta(\vec{r} - \vec{r}_p)\delta(\vec{v} - \vec{v}_p), \tag{2.9}$$

where N_p is the number of physical particles present in the macroparticle (like a particle weight) and δ is the Dirac delta function. However, this functional form is not desirable as it reproduces a very spiky distribution function, giving rise to spurious short range interactions. As we want to simulate the non-collisionality, this scheme is unfavorable and so other functional forms that give the macroparticles a finite size[1] are usually preferred:

[1] There are several advantages for using finite-sized macroparticles, the most important is that this shape suppresses the short-range interactions, reducing the occurrence of spurious collisions and therefore contributing to the modelling of the non-collisionality.

$$f_p(\vec{r}, \vec{v}, t) = N_p S_x(\vec{r} - \vec{r}_p) S_v(\vec{v} - \vec{v}_p), \tag{2.10}$$

where S_x and S_v are the so called shape functions defined to characterize the macroparticles. These shape functions will further determine some of the properties of the numerical method, as they will be present in the expressions for the charge density and electric current.

2.2.1 The computation cycle of PIC

Having defined the particles, now we will describe the cycle of three steps the code performs per timestep Δt. We can see the cycle depicted in figure 2.1. The three steps are: first, Newton's equations with the relativistic Lorentz force are solved for each particle. That allows to move the particles to their updated positions and velocities. Secondly, the algorithm gathers the contribution of each particle to the charge and current densities and deposits them into the grid in which the EM fields are defined. Finally, Maxwell's equations are solved on the grid with the source information of the previous step and then the updated values for $\vec{E}$ and $\vec{B}$ are obtained.

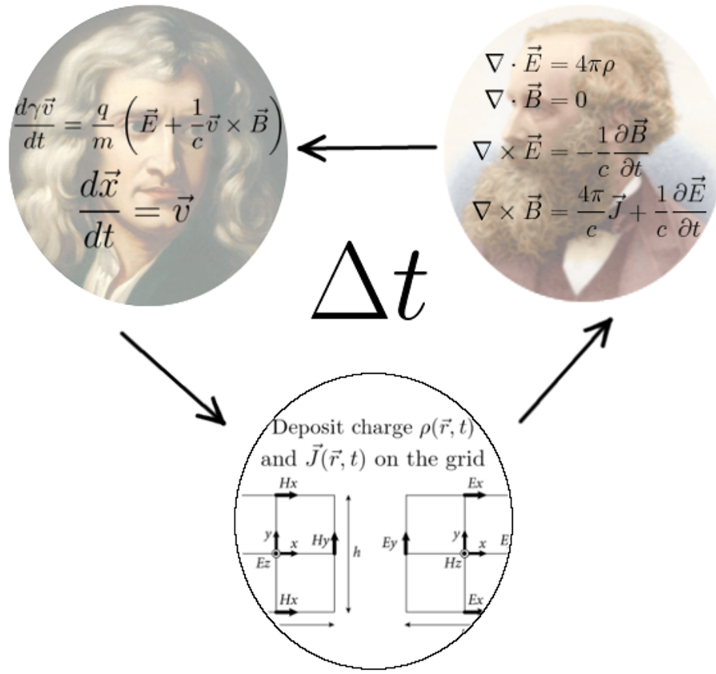

Figure 2.1: The three stages that PIC solves to advance one timestep Δt. First, Newton's equations for the Lorentz force are solved for each particle, then the charge and current densities are collected and deposited in the grid and then Maxwell's equations are solved.

We will briefly describe each one of these three steps:

i) **Particle Pusher:** Here the Newton's equations are solved for each of the particles,

$$\frac{d\gamma m\vec{v}}{dt} = q\left(\vec{E} + \frac{\vec{v}\times\vec{B}}{c}\right) \tag{2.11}$$

$$\frac{d\vec{r}}{dt} = \vec{v} \tag{2.12}$$

With $\gamma = \sqrt{1 - v^2/c^2}$ the gamma factor. One of the most used algorithms for solving Newton's equations (and the one that is implemented in the code used in this thesis) is the Boris Pusher [37, 38]. It is a leapfrog integration method with very nice properties (Second-order accurate, stable, fast, among others). The discretization of Newton's equations reads:

$$\frac{(\gamma\mathbf{v})^{n+1/2} - (\gamma\mathbf{v})^{n-1/2}}{\Delta t} = \frac{q}{m}\left(\mathbf{E}^n + \frac{\mathbf{v}^n \times \mathbf{B}^n}{c}\right) \tag{2.13}$$

$$\frac{\mathbf{r}^{n+1} - \mathbf{r}^n}{\Delta t} = \mathbf{v}^{n+1/2} \tag{2.14}$$

where we denote vector quantities now with bold letters to keep the notation simple. Now, in order to transform $\mathbf{v}^n$ in the RHS into half the timestep, we take the average of the two others, $(\gamma\mathbf{v})^n = ((\gamma\mathbf{v})^{n+1/2} - (\gamma\mathbf{v})^{n-1/2})/2$. This way equation 2.14 can be solved for $\mathbf{v}^{n+1/2}$, with the aid of some convenient auxilary variables [37].

For the position we solve for $\mathbf{r}^{n+1}$:

$$\mathbf{r}^{n+1} = \mathbf{r}^n + \Delta t \mathbf{v}^{n+1/2} \tag{2.15}$$

ii) **Charge and current deposition**: Having advanced each particle to their new position, we need to calculate the source terms in order to solve Maxwell's equations. In order to do so, PIC uses a spatial grid that allows to reduce the number of operations per timestep to $\mathcal{O}(N)$, with N the number of particles (instead of the $\mathcal{O}(N^2)$ of binary interactions). This means that the particles feel each other through the EM fields, and not by binary Coulomb interactions. Recalling our definition of macroparticles, the charge and current densities can be calculated as:

$$
\begin{aligned}
\rho(\mathbf{r},t) &= q\int_v \sum_p f_p(\mathbf{r},\mathbf{v},t)d\mathbf{v} && (2.16)\\
&= \sum_p q\int_v N_p S_{\mathbf{r}}(\mathbf{r}-\mathbf{r}_p)S_{\mathbf{v}}(\mathbf{v}-\mathbf{v}_p)d\mathbf{v}\\
\mathbf{J}(\mathbf{r},t) &= q\int_v \sum_p \mathbf{v}f_p(\mathbf{r},\mathbf{v},t)d\mathbf{v} && (2.17)\\
&= \sum_p q\int_v \mathbf{v}N_p S_{\mathbf{r}}(\mathbf{r}-\mathbf{r}_p)S_{\mathbf{v}}(\mathbf{v}-\mathbf{v}_p)d\mathbf{v}
\end{aligned}
$$

It is common to assume a delta distribution for velocities in the shape function of $f_p(\mathbf{r},\mathbf{v},t)$, so $S_{\mathbf{v}}(\mathbf{v}-\mathbf{v}_p) = \delta(\mathbf{v}-\mathbf{v}_p)$. In this case the above expressions can be written as:

$$
\rho(\mathbf{r},t) = \sum_p qN_p S_{\mathbf{r}}(\mathbf{r}-\mathbf{r}_p) \tag{2.18}
$$

$$
\mathbf{J}(\mathbf{r},t) = \sum_p qN_p \mathbf{v} S_{\mathbf{r}}(\mathbf{r}-\mathbf{r}_p) \tag{2.19}
$$

The shape function allows the particles to distribute their charges over the grid. It is desirable to deposit this charge density in a smooth way on the grid, so an appropriate functional form for $S_{\mathbf{r}}(\mathbf{r}-\mathbf{r}_p)$ should be chosen. To illustrate this, let us analyse first the deposition to lowest order, or the so called "Nearest grid point" deposition.

In figure 2.2 we can see how this method works in 1D. Essentially, all the charge that a particle carries is concentrated in its position after being pushed. So if the particle ends inside a specific cell of size Δx, no matter in which position inside the cell, all the charge of that particles goes into that specific cell. This method turns out to be the simplest and fastest case, but with the cost of having a very spiky and noisy solution.

The next order is to consider the charge uniformly distributed within the particle finite size, or any other functional form to distribute the charge. This method is

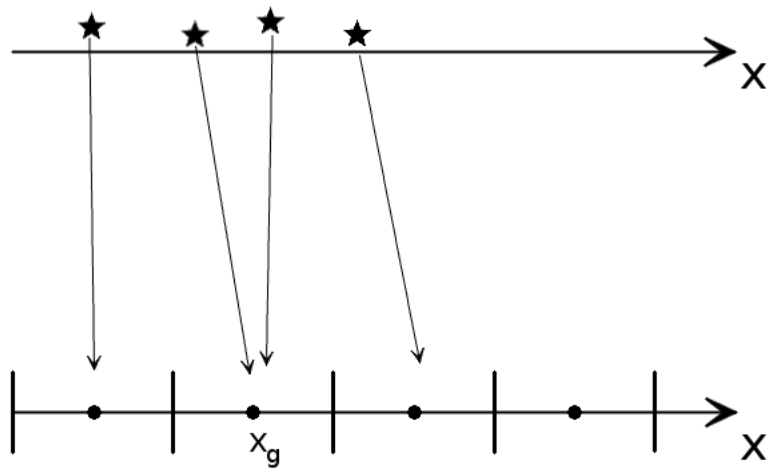

Figure 2.2: Schematic diagram of the Nearest Grid Point method in 1D to deposit charge and current densities into the grid where the electromagnetic fields are defined. All the charge in concentrated in the position of the particle (stars) in its continuous space (upper x-axis) and the entire contribution will be deposited into the single nearest cell to its position(lower x-axis). Figure modified from `https://static.ias.edu/pitp/2016/sites/pitp/files/pictutorialas2016.1.pdf`

called “Cloud-in-cell” deposition. In figure 2.3 we can see a version in which the charge is uniformly distributed. This way, if the particle ends midway between two cells, for instance, the corresponding amount of charge will go to both of these cells proportionally. There exists higher order shape functions for the particle size based on convolutions of this initial uniform shape. It is desirable to have a shape function of an order high enough to reduce the noise without being so computationally expensive.

iii) **Fields Evolution**: To evolve the electromagnetic fields, they are spatially discretized in a grid and Maxwell’s equation are solved by the Finite Difference Time-Domain Method (FDTD) proposed firstly by Yee [39]. The method is robust, simple and second-order accurate in space and time. The idea is to discretize the electric and magnetic field such that every component of the electromagnetic field is decentered. This way, additionally to be decentered in time

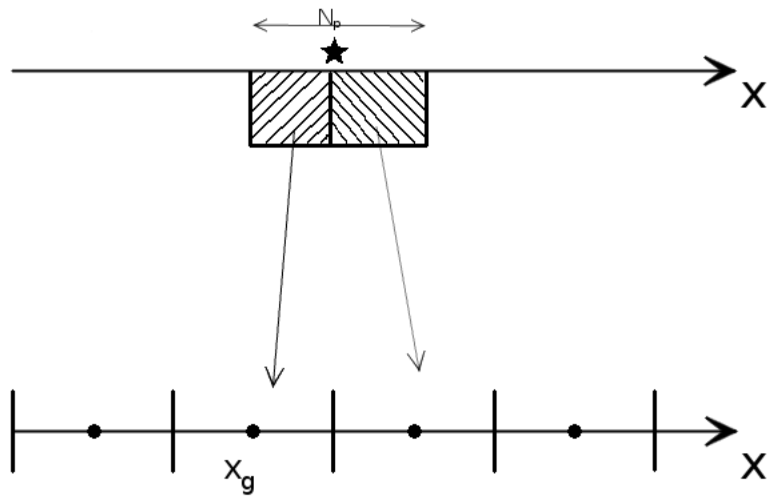

Figure 2.3: Schematic diagram of the Cloud In Cell method deposition in 1D. The charge is uniformly distributed within the size of the particle in its position (star) and the amount of charge goes into the cell according to its position. Figure modified from `https://static.ias.edu/pitp/2016/sites/pitp/files/pictutorialas2016.1.pdf`

they are now decentered in space, using the same leapfrog scheme. It can be proved that this ensures the condition $\nabla \cdot \mathbf{B} = 0$ to machine precision. The grid in the FDTD model (Yee mesh hereafter) is shown in figure 2.4.

We can see that the components of $\mathbf{B}$ are centered on the faces of the cell while the components of $\mathbf{E}$ lie on the edges of the cell. The reason behind this configuration becomes clear when we deal with the integration of Faraday's and Ampère's Laws. For instance, when doing a contour integration of $\nabla \times \mathbf{E}$, its components on the edges of the specific cell can be directly used to obtain the desired component of $\partial \mathbf{B}/\partial t$, as can be seen in figure 2.4 above the cell. The same can be shown for the integration of Ampère's Law.

There are also some constraints on the value of the timestep Δt and the grid spacing Δx_g. In first place, it can be shown that the method is stable if the following conditions, called the *Courant-Friedrichs-Lewy* conditions, are fulfilled:

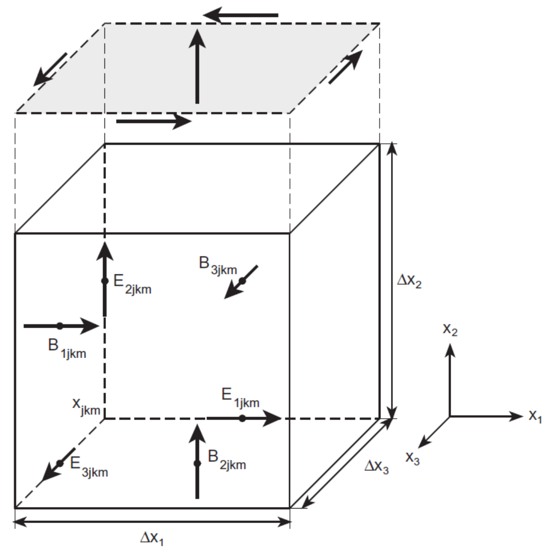

Figure 2.4: Yee mesh and the fields components defined on it. Note that the **B** components are defined on the faces of the cell and the **E** components are defined on the edges of the cell, totally decentered. Indices i, j, k denote the orthogonal directions of any set of coordinates. In the upper part it can be seen a contour integration in which the **B** component is normal to the surface and the **E** components match exactly the circulation around the surface being integrated. Figure taken from [40].

$$\left(\frac{c\Delta t}{\Delta x}\right)^2 < 1 \tag{2.20}$$

$$(c\Delta t)^2 \left(\frac{1}{\Delta x^2} + \frac{1}{\Delta y^2}\right) < 1 \tag{2.21}$$

$$(c\Delta t)^2 \left(\frac{1}{\Delta x^2} + \frac{1}{\Delta y^2} + \frac{1}{\Delta z^2}\right) < 1 \tag{2.22}$$

Physically speaking, by the way, it is desirable that the code is capable to resolve all the relevant scales of the system. Whether we want it or not, phenomena such as the plasma oscillations and the Debye screening will be present in any plasma, so it is naturally to impose the conditions of $\omega_{p,e}\Delta t \ll 1$ and $\Delta x_g/\lambda_D \ll 1$ as well.

Although the framework behind PIC codes has been around for, at least, 30 years now, it is quite recently that the computational capabilities have been powerful enough to allow this codes to simulate astrophysical conditions in a more realistic way. Efforts along these lines have been made, for instance, in the context of efficiently parallelizing these codes. The scheme usually used (which is the one implemented in the code employed in this thesis) is domain decomposition, with the different parallel processes communicating with each other using the Message Passing Interface (MPI).

2.3 Numerical Setup

In this section the setup of the simulation used in this thesis is described. We used the Particle-In-Cell, electromagnetic and relativistic code TRISTAN-MP [41, 42] in 2D and 1D. Details about the 1D implementation can be found in Appendix B. In this code we simulate a collisionless, magnetized plasma composed of ions and electrons. The simulation box is a square box in the $x-y$ plane, containing the plasma and an initially homogeneous magnetic field $\vec{B}_0 = B_0\hat{x}$. The system is subject to an imposed, incompressible shear motion so that the mean particle velocity is $\vec{v} = -sx\hat{y}$, with x the distance along $\hat{x}$ and s the shear parameter with units of frequency. Consequently, by flux conservation, the mean magnetic field is amplified such that the y-component of $\vec{B}$ evolves as $\partial\langle B_y\rangle/\partial t = -sB_0$. Additionally to the growth of $|\langle\vec{B}\rangle|$, due to the conservation of the particles' magnetic moment $\mu_j \propto v_{\perp,j}^2/2B$, a pressure anisotropy arises such that $\Delta p_j \equiv p_{\perp,j} - p_{\parallel,j} > 0$. A schematic diagram of the shear motion can be seen in figure 2.5.

The relevant varying physical parameters that characterize our simulations are the initial plasma beta $\beta_{i,\text{init}} = 8\pi p_i/|\vec{B}|^2$, for which we will explore two regimes, $\beta_{i,\text{init}} = 0.5$ and $\beta_{i,\text{init}} = 2$, the ion magnetization, quantified by the ratio of the initial cyclotron frequency and the shear frequency $\omega_{c,i}/s$ and the mass ratio of ions and electrons m_i/m_e and the ion temperature kT_i/m_ic^2 (in all of our runs we use

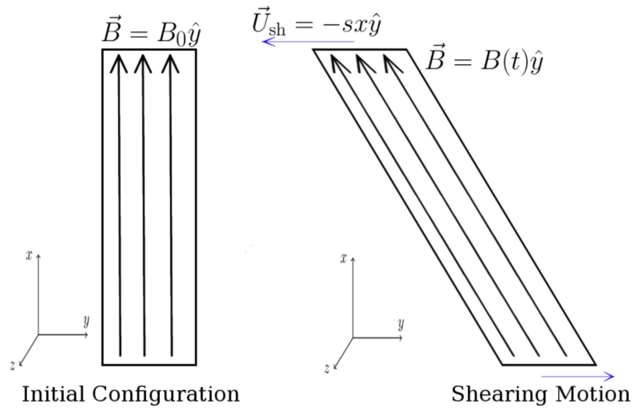

Figure 2.5: Schematic diagram of the simulation box subject to the shear motion $U_{\rm sh} = sy\hat{x}$. The y-component of the mean magnetic field evolves as $\partial\langle B_y\rangle/\partial t = -sB_0$ resulting in an amplification of the mean magnetic field $\langle\vec{B}\rangle$.

β_e=β_i). Even though we consider here $\omega_{c,i}/s \gg 1$[2], due to computational limitations their values are still much smaller than in astrophysical environments. The same happens with the mass ratio, their values are still much smaller than the proton-electron mass ratio $m_p/m_e = 1836$. Nevertheless, we perform careful convergence tests to make sure the net effect was not very sensitive to these parameters.

A fixed parameter in our simulation is $k_BT_i/m_ic^2 = 0.05$ (with k_B the Boltzmann's constant, T_i the ion temperature and m_i the ion mass). The numerical parameters are the number of macroparticles per cell, $N_{\rm ppc}$, the ion skin depth in terms of the grid spacing $c/(\omega_{p,e}/\Delta_x)$ and the box size in terms of the initial ion Larmor radius $L/R_{L,i}^{\rm init}$ (with $R_{L,i}^{\rm init} = v_{th,i}/\omega_{c,i}$ and $v_{th,i}^2 = k_BT_i/m_i$). A compilation of a representative set of the run simulations are listed in Table 2.1. In order to do some convergence tests, many more simulations were run, but only the simulations used to show the results in chapter 3 were considered in Table 2.1.

The analysis of the outputs of every simulation were performed using routines written by the author in Python. The analysis included the convergence tests for the numerical parameters, for the dimensionality (1D to 2D comparison), the dependence

[2]In a realistic environment, like the one close to Sgr A*, one can estimate $\omega_{c,i}/s \sim 10^8$ [29]

Runs	m_i/m_e	β_{init}	$\omega_{c,i}/s$	$c/\omega_{p,e}/\Delta x$	N_{ppc}	$L/R_{L,i}$	Dimension
R1	2	0.5	800	15	160	67	2D
R2	2	2	1600	7	160	198	2D
R3	2	0.5	800	15	640	113	1D
R4	2	0.5	800	30	320	52	1D
R5	4	0.5	1200	30	480	76	1D
R6	4	0.5	1600	30	320	44	1D
R7	8	0.5	1600	30	320	33	1D
R8	2	0.5	800	30	320	52	1D
R9	2	0.5	3600	30	320	112	1D
R11	2	0.5	1600	15	640	114	1D
R12	2	0.5	1600	7	160	74	2D
R13	2	2	800	7	160	198	2D
R14	2	0.5	800	7	160	148	2D
R15	2	0.5	800	15	1280	54	1D
R16	8	0.5	800	15	1280	63	1D
R17	32	0.5	800	15	1280	66	1D
R18	8	0.5	1600	15	1280	63	1D
R19	8	0.5	3200	15	1280	63	1D
R20	2	0.5	800	15	80	67	2D

Table 2.1: A representative set of the simulations analyzed in this work with their respective physical and numerical parameters, corresponding to the mass ratio m_i/m_e, the initial plasma beta $\beta_{i,\text{init}}$, the magnetization $\omega_{c,i}/s$, the skin depth in terms of the grid spacing $c/\omega_{p,e}/\Delta x$ (Δx is the separation between grid points), the number of macroparticles per cell N_{ppc}, the size of the numerical box in terms of the initial ion Larmor radius, $L/R_{L,i}$, ($R_{L,i} = v_{th,i}/\omega_{c,i}$ and $v_{th,i}^2 = 3p_i/\rho$, with ρ the mass density of the ions) and the dimension of the simulation box. Convergence tests were performed and confirmed for numerical resolution of $c/\omega_{p,e}/\Delta x$, N_{ppc} and $L/R_{L,i}$.

of the results with the mass ratio m_i/m_e and the magnetization $\omega_{c,i}/s$ and all the results shown in the next chapter.

2.4 Simulating the Pressure Anisotropy-driven Instabilities

In our simulations we seek to capture the growth and non-linear evolution of pressure anisotropy-driven instabilities in a self-consistent way. This is important because in realistic astrophysical settings, the instabilities are in their saturated, non-linear regime most of the time, with the initial, exponential regime of the unstable modes being only a short transient in the evolution of the plasma. In order to achieve this, our simulations do not start with an already anisotropic velocity distribution of particles. Instead, the plasma will initially have an isotropic, Maxwellian distribution for ions and electrons. Given the action of the imposed shear motion in the plasma, and due to magnetic flux freezing, the magnetic field starts to be amplified steadily, so the magnetic energy grows linearly with time.

For its part, the adiabatic invariance of the magnetic moment of each individual particle $\mu_j = v_{\perp,j}^2/2B$ in collisionless plasmas makes $p_{\perp,j}$ grow as $\langle\vec{B}\rangle$ grows, that creates a pressure anisotropy $p_{\perp,j} > p_{\parallel,j}$, which can make the plasma unstable and willing to return to its previous, isotropic state. This instability of the plasma manifests itself through the rapid growth of a variety of electromagnetic waves that, after reaching a large enough amplitude, can efficiently pitch-angle scatter the particles, producing a decrease of the pressure anisotropy. This stage of efficient scattering is what we will refer to as the saturated, non-linear regime of the pressure anisotropy-driven instabilities. Given that the magnetic field amplification is maintained through the entire simulation, its effect in trying to increase the particles' pressure anisotropy also continues. This implies that the saturated stage of the instabilities is characterized by the competition between the anisotropy growing effect of the magnetic field amplification, and pitch-angle scattering due to the unstable modes. As we will see below, this competition ends up setting the amplitude of the modes, which needs to be large enough to pitch-angle scatter the particles at a rate comparable to the growth rate $\sim s$ of the background magnetic field.

Chapter 3

Results

In our study, where the pressure anisotropy of the ions is of the form $p_\perp > p_\parallel$, two plasma instabilities can arise, the mirror instability and the ion-cyclotron (IC) instability [43, 44]. As we continuously drive the growth of $\langle \vec{B} \rangle$, we expect that the pressure anisotropy growth competes with the action of these instabilities to isotropize the pressures.

Figure 3.1 shows the three components of the magnetic and electric field fluctuations $\delta B_j \equiv (B_j - \langle B_j \rangle)/B_0$ (j denotes the three spatial components and the $\langle\rangle$ denotes spatial average), at $t \cdot s = 2$, for simulations R14 (upper row) and R13 (lower row), which correspond to $\beta_i = 0.5$ and $\beta_i = 2$, respectively. The arrows denote the direction of the mean magnetic field on the $x - y$ plane and we can see that $|\langle B_y \rangle| \approx 2|\langle B_x \rangle|$.

In panels 3.1c and 3.1f it can be seen that the field fluctuations that start to develop propagate nearly parallel to $\langle \vec{B} \rangle$. This parallel propagation is a characteristic feature of the IC modes[45]. On the other hand, panels 3.1b and 3.1e (δB_y component) show in the two simulations the presence of oblique modes, whose orientation is typical of the mirror instability [46]. Panels 3.1a and 3.1d show a mixture of the IC and mirror modes. The reason why the IC modes show up so clearly in the δB_z component is because the magnetic fluctuations associated to the mirror modes tend

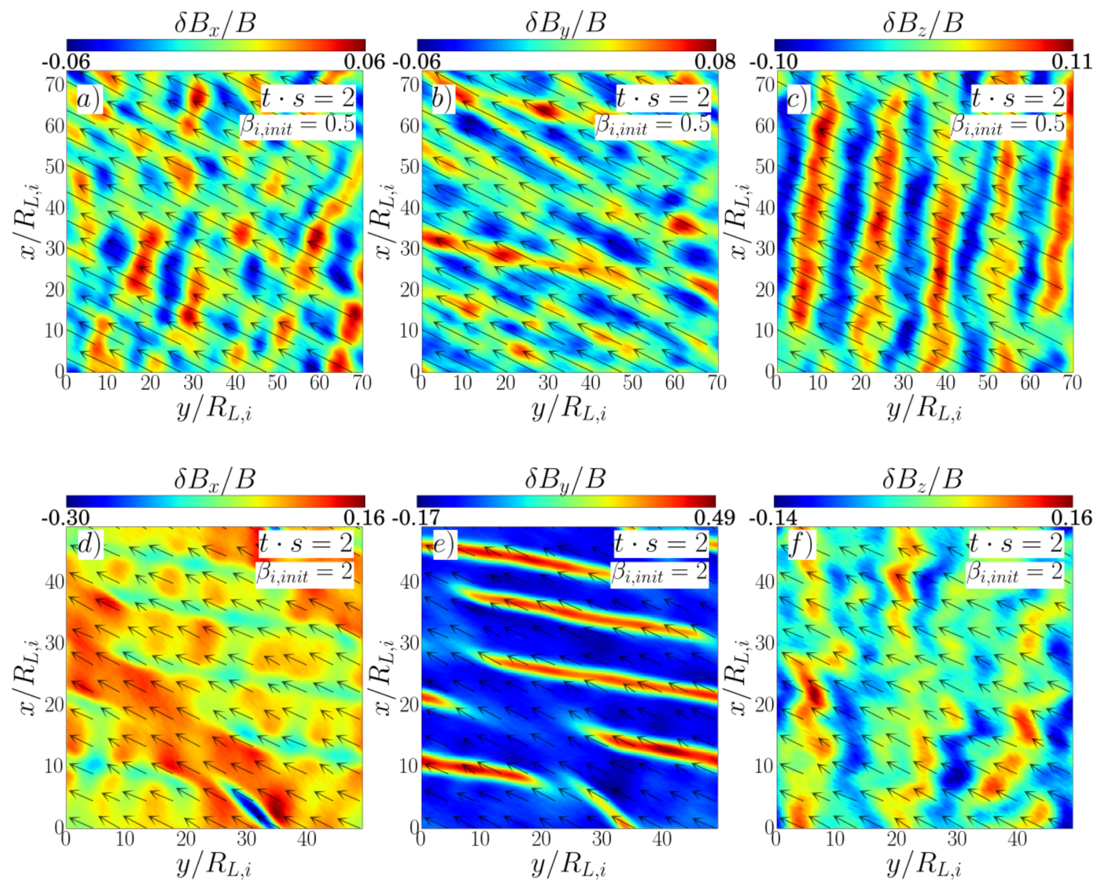

Figure 3.1: The three components of $\delta\vec{B}$ (upper row) for simulation R14 ($m_i/m_e = 2$ and $\beta_{i,\text{init}} = 0.5$), and the three components of $\delta\vec{B}$ for simulation R13 ($m_i/m_e = 2$ and $\beta_{i,\text{init}} = 2$), at time $t \cdot s = 2$ (bottom row). The field fluctuations are normalized by the background magnetic field B at $t \cdot s = 2$ and the black arrows denote the direction of the mean magnetic field on the simulation plane. The IC modes propagates with dominant wave vectors nearly parallel to $\langle\vec{B}\rangle$. In the $\beta_{i,\text{init}} = 0.5$ case, the amplitude of the IC modes (wave-vectors quasi-parallel to $\langle\vec{B}\rangle$) is comparable to the amplitude of the mirror modes (wave-vectors oblique with respect to $\langle\vec{B}\rangle$). The opposite is true in the $\beta_{i,\text{init}} = 2$ case.

to be mainly coplanar with their wave vector k and the background field B [47]. One important difference between the cases with $\beta_i = 0.5$ and $\beta_i = 2$ is that for the $\beta_{i,init} = 0.5$ case the IC modes contribute to the fluctuations comparably to the other fluctuation components, whereas in the $\beta_{i,init} = 2$ case they are not dominant.

For the triggering of the instabilities, however, the system has to surpass certain thresholds for the anisotropies [48]. The system, therefore, will evolve steadily at first, with the pressure anisotropy $\Delta p_i = p_{\perp,i} - p_{\|,i}$ steadily growing as well, until it reaches the threshold for the triggering and growth of the IC and mirror instabilities. This marks the end of the initial phase. This regime is essentially the same in the two $\beta_{i,\mathrm{init}}$ cases.

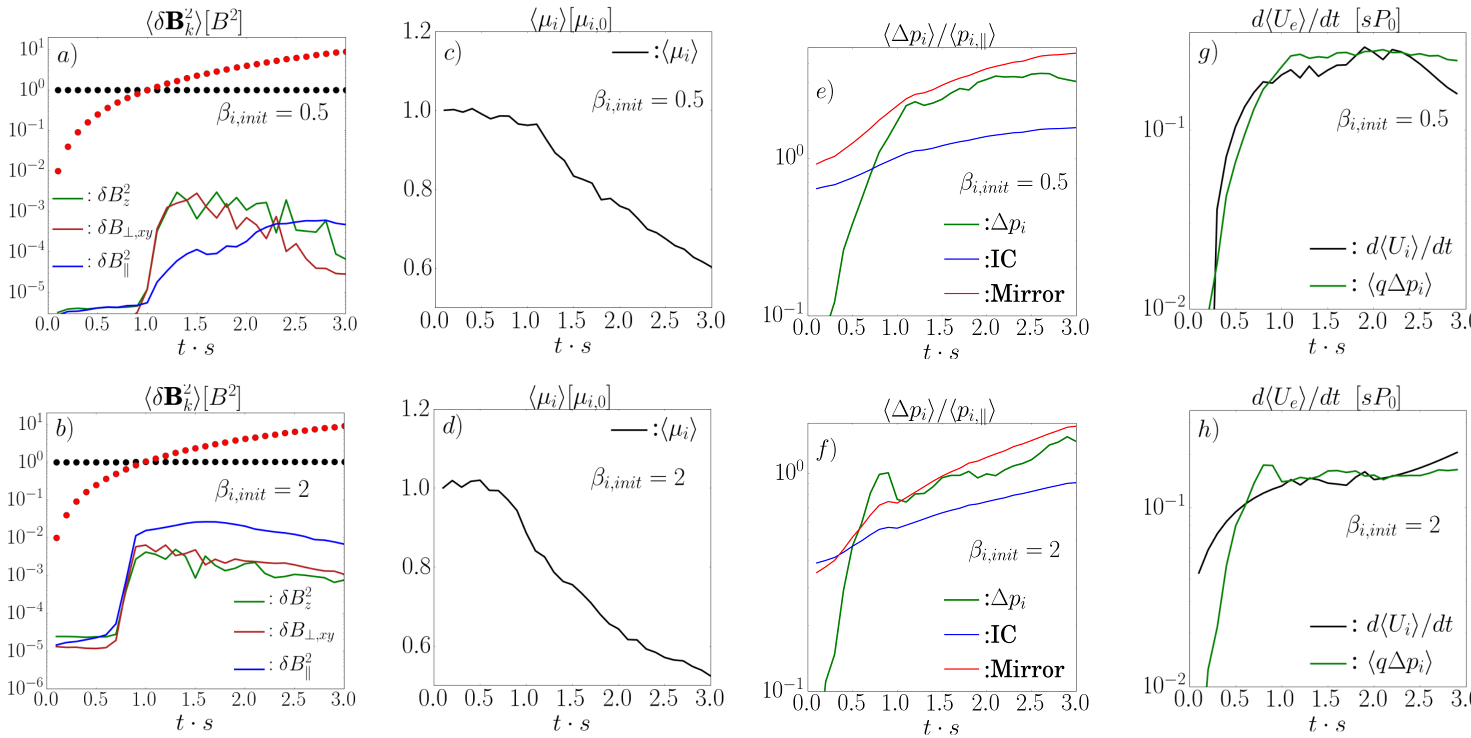

Figure 3.2: Evolution of relevant volume-averaged quantities for the same simulations R1 ($\beta_{i,\mathrm{init}} = 0.5$) , R13 ($\beta_{i,\mathrm{init}} = 2$) in figure 3.1. In the upper row there are the quantities for simulation R1 and in the second row the ones for simulation R13. In the first column the energy stored in $\delta \vec{B}$ is shown, normalized by B^2 for the z component (δB_z, green line), the perpendicular component in the $x - y$ plane ($\delta B_{\perp,xy}$, dark-red line) and parallel component ($\delta B_\parallel$, blue line) to $\langle \vec{B} \rangle$. Black and red dotted lines show $\langle B_x \rangle^2$ and $\langle B_y \rangle^2$, respectively. The second column shows the ion magnetic moment μ_i, while in the third column there is the ion pressure anisotropy (green line) with the linear ion-cyclotron threshold (blue line) and mirror threshold (red line) for growth rates $\gamma_\omega = 800/\omega_{c,i}$. The fourth column shows the evolution of the time derivative of the volume-averaged internal energy of the ions ($d\langle U_i \rangle/dt$) normalized by sP_0, with P_0 the initial ion pressure, and the expected rate of heating by the anisotropic viscosity $q\Delta p$.

We can clearly identify this point in figure 3.2. Panels 3.2e and 3.2f shows the evolution of the normalized pressure anisotropy throughout the two simulations. We can see that around $t \cdot s \approx 0.8$ the pressure anisotropies, $\Delta p_i/p_{i,\|}$, stop their rapid initial growth, and reach a quasi-stationary, saturated state. The role played by the mirror and IC instabilities can be appreciated by comparing the ion anisotropy in the saturated state with the threshold anisotropy for the growth of the mirror and IC instabilities with a growth rate $\Gamma_{growth} = 800\omega_{c,i}$ (red and blue lines, respectively).[1] This growth rate was chosen so that this comparison gives us an idea of whether the ion pressure anisotropies in the simulations are capable to make the instabilities grow at a rate comparable to the rate at which Δp_i is driven ($\sim s = 800\omega_{c,i}$). If the threshold of an instability is larger than the ion anisotropy, it means that the role played by that instability in the regulation of Δp_i is most likely weak. This is indeed what happens in the case of the run with $\beta_i = 0.5$, where the mirror threshold is larger than the obtained anisotropy. This implies that the isotropization of the pressure is mainly caused by the IC instability, whose anisotropy threshold is smaller than $\Delta p_i/p_{i,\|}$. We point out, however, that the ion anisotropy in the simulation is a factor ~ 2 larger than the threshold for the growth of the IC modes. This is possibly a consequence of the departure from a bi-Maxwellian distribution of the ions in the saturated IC state, as has been proposed by a previous study in order to explain a similar discrepancy between linear theory and solar wind observations [50]. Similarly, in the $\beta_i = 2$ case, the pressure anisotropy is still larger than the IC threshold (consistent with the presence of IC modes), but is significantly closer to the mirror threshold than in the $\beta_i = 0.5$ case. This last feature is consistent with the much more prominent growth of the mirror modes in the larger β_i simulation. This point also determines the end of the regime where μ_i is conserved, as shown in panels 3.2c and 3.2d. This violation of μ conservation is indicative of the particles

[1] These thresholds were provided by our collaborator Daniel Verscharen, who calculated them using the linear Vlasov solver developed in [49].

experiencing fluctuations in the magnetic fields due to the IC and mirror modes that occur on time scales that are short enough to break the condition for adiabatic invariance of μ_i. This exponential growth of $\delta\vec{B}$ is present in both $\beta_{i,\text{init}}$ cases, as seen in panels 3.2a and 3.2b, but in the $\beta_{i,\text{init}} = 0.5$ case (panel 3.2a) we can see that $\delta B_\perp$ clearly dominates, being consistent with the arising of the nearly parallel IC modes, while in the $\beta_{i,\text{init}} = 2$ case (panel 3.2b) both components grow at the same rate, because the mirror modes become important and contribute to $\delta B_\parallel$ [51]. However, once the instability enters to the nonlinear regime around $t \cdot s \approx 1.2$, a different evolution arises in the two cases. Around that time, the growth of $\langle\delta\vec{B}\rangle$ saturates and continues in a quasi-stationary regime. At this point, we can see that the mirror mode dominates at larger values of $\beta_{i,\text{init}}$ in the nonlinear regime, something already detected in previous works and expected to happen [52, 51]. In contrast, in panel 3.2a there is a stage in which $\delta B_\perp$ is clearly dominant, leaving time for the IC modes to grow, until enough time has passed to $\delta B_\parallel$ to grow and surpass $\delta B_\perp$. This dominance of the mirror modes over IC modes in nonlinear stages can be happening because of the departure from the Maxwellian distribution the ions initially have, that in turn can increase the threshold needed for the anisotropy to generate the IC instability [50]. However, despite this late-time dominance of the mirror modes, it is important to emphasize that during most of the non-linear stage of simulation R1, the IC modes dominate over the mirror modes. This dominance of the IC instability, as we will see below, will have important consequences for the evolution of the energy distribution of the ions.

It is quite interesting that the rapid initial stage of growth of the pressure anisotropy and the energy in $\langle\delta\vec{B}\rangle$ reaches a quasi-stationary state when the plasma instabilities are present, in a way in which the last ones somehow self-regulates the pressure anisotropy.

3.1 Ion heating

Before going into the analysis of the energy spectra of the particles, another essential effect in collisionless plasmas will be described, namely, the ion heating by anisotropic viscosity. In a homogeneous, incompressible plasma with no heat flux, the internal energy density of the ions U_i changes as (see Appendix A):

$$\frac{dU_i}{dt} = q\Delta p_i \tag{3.1}$$

where $\Delta p_i = p_{i,\perp} - p_{i,\|}$ and $q = (dB/dt)/B$ is the growth rate of the mean magnetic field. As already seen, in a collisionless, magnetized plasma with a growing magnetic field we have $p_{i,\perp} > p_{i,\|}$, so the net effect is an increase in the ion internal energy, i.e., an ion heating. The anisotropy, as we have seen, cannot grow unlimitedly as kinetic microinstabilities arise and limit its growth. To quantify this contribution in the simulations, we compare the variation of the total internal energy of the ions with the expected ion heating rate by the anisotropy in panels 3.2g and 3.2h , where we can see that, aside from numerical noise, the two curves follow the same trend, indicating that the internal energy is growing due to this anisotropic heating. Moreover, we can see that, as U_i is the total internal energy, virtually all the ion heating is produced by this anisotropic viscosity, then being the only source of energy of the system, that ultimately comes from the imposed shearing motion.

3.2 Energy Spectra

In this section we show the evolution of the ion energy distribution throughout the simulation with $\beta_i = 0.5$ and $\beta_i = 2$. This is one of the most important results of this work and also the key feature that distinguishes the two $\beta_{i,\mathrm{init}}$ cases in study.

3.2.1 Case $\beta_{i,init} = 0.5$

We can see the energy spectra for the simulation R1 for this case in figure 3.3a. It can be seen that once the IC instability is developed around $t \cdot s \approx 0.7$ there is a rapid growth to a nonthermal energy tail. By $t \cdot s = 3$ the tail can be approximated fairly well by a a power law $dn/d\gamma \propto (\gamma - 1)^{-\alpha_s}$ with an spectral index $\alpha_s \sim 3.4$, plus the presence of two bumps at $\gamma - 1 \sim 0.5$ and we can see that the spectral index continuously decreases even by the end of the simulation, at $t \cdot s = 3$. The peak of the spectrum also shifts to larger energies by a factor of ~ 1.6, due to the ion heating contribution that moves the entire spectra to larger energies.

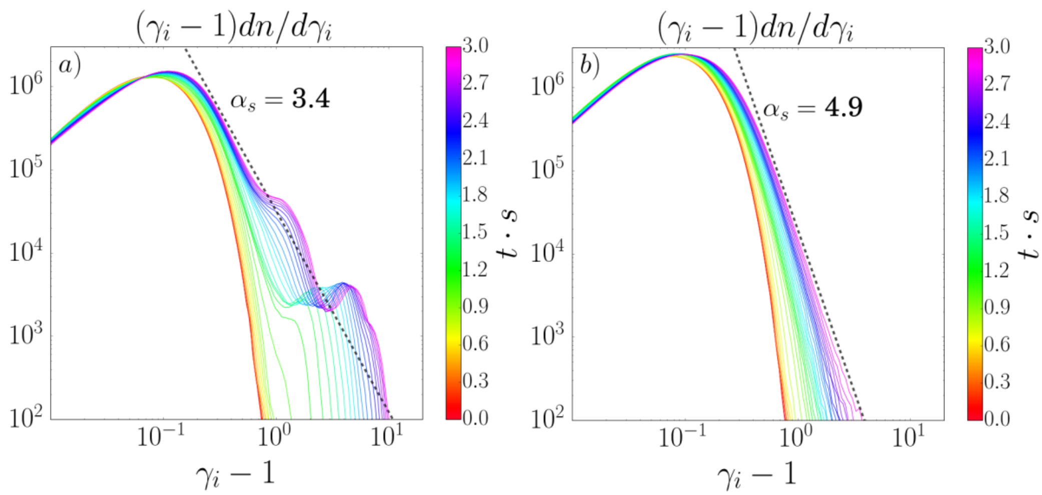

Figure 3.3: Evolution of the ion energy distribution with time indicated by the colorbar for simulation R1 ($m_i/m_e = 2$, $\beta_{i,init} = 0.5$, panel *a*) and simulation R13 ($m_i/m_e = 2$, $\beta_{i,init} = 2$, panel *b*). In panel *a* there is a rapid growth to a nonthermal energy tail once the IC instability is developed and the IC modes reach saturation around $t \cdot s \sim 1$. By $t \cdot s = 3$ the tail can be approximated by a power law $dn/d\gamma \propto (\gamma - 1)^{-\alpha_s}$ with a spectral index $\alpha_s \sim 3.4$ plus two bumps. On the other hand, in panel *b* the growth of the nonthermal energy tail is also present but with a slower growth throughout the whole simulation. By $t \cdot s = 3$ the tail can be approximated by a power law $dn/d\gamma \propto (\gamma - 1)^{-\alpha_s}$ with an spectral index $\alpha_s \sim 4.9$

3.2.2 Case $\beta_{i,init} = 2$

We can see the energy spectra for the simulation R13 for case $\beta_{i,\mathrm{init}} = 2$ in figure 3.3b. In this case, we can also see a nonthermal energy tail growing continuously during all the simulation, but now noticeably more slower than in the previous case, although by $t \cdot s = 3$ the spectral index is still decreasing as well. We can approximate the tail by a a power law $dn/d\gamma \propto (\gamma - 1)^{-\alpha_s}$ with an spectral index $\alpha_s \sim 4.9$. The peak of the spectrum also shifts to larger energies by a factor of ~ 1.2. Quite intriguingly, in this case no bump is present at all; the growth of the nonthermal tail is completely smooth.

3.3 Test Particles

In this section the question about the nature of the acceleration mechanism is addressed. Up to now we have seen that there exists a population of ions that is accelerated to higher energies from the thermal pool, forming a power-law of spectral index $\alpha_s \sim 3.4$ at $t \cdot s = 3$ in the most efficient case. However, we still do not know where this energy is coming from, whether it is from the IC and mirror waves themselves that get damped while transferring their own energy to the ions, or whether the interaction is rather between the two population of particles and the waves act as a mediator to transfer the energy from thermal to nonthermal ions.

In order to tackle this questions we perform a “test particles” analysis. This corresponds to running the simulation once and then identifying different population of particles with specific final energies, say, selecting all particles that ended with energies in one or more definite ranges of $\gamma - 1$. This selection can be easily done by inspecting the final energy distribution of the particles. Then, with these particles already identified, we re-run the same simulation exactly as the first time but now tracking the evolution of each one of these particles, saving all their properties in each timestep. That allows us to analyse how the particles, for instance, are being energized throughout the whole simulation, and see whether they are losing energy or gaining energy, how much and by which mechanism. The nice thing about this type of analysis is that in TRISTAN-MP it is relatively easy to follow the evolution of any macroparticle; they can be uniquely identified and, as it is completely self-consistent, every interaction any particle suffers can be tracked by looking at its properties and the values of the electromagnetic fields nearby.[2]

We perform this analysis in the simulation R20, continuing with the focus on the $\beta_{i,\text{init}} = 0.5$ only. The ranges of $\gamma - 1$ we have selected are listed in Table 3.1.

To see how these particles have gained energy, we have to identify the physical entities that are doing mechanical work on the particles. There are only two agent in the system capable to do work, namely, the anisotropic viscosity, that is driven by the shear motion and has the effect of heating the ions (see Appendix A), and the electric field associated with the waves generated by the IC and mirror instability[3]. Therefore, for each selected particle of both subsets we calculated the work done by the anisotropic viscosity, $q\Delta p_i$, and the electric field of the waves, $W_{\vec{E}}$, and we also calculate the energy gain $\Delta\gamma(t) = \gamma(t) - \gamma_{\text{init}}$ and compare these three quantities throughout the whole simulation.

The evolution throughout the simulation of these quantities can be seen in figure 3.4 for the three subsets. We see that the average energy gain is roughly zero until $t \cdot s \sim 1$ where the instabilities develop. The average energy gain is positive in both

[2]Note that the name we have given has little to do with the “Test Particle” analysis in linear Diffusive Shock Acceleration, where the particles that are called “test particles” do not do any backreaction at all to the system. Here the particles that we are calling test particles have no special status, we have not introduced any new kind of particle, we simply select any macroparticle the simulation itself creates, and therefore they naturally do a backreaction in the rest of the system and participate in the whole dynamic process.

[3]More precisely, in a shearing plasma there exists another electric field associated with the motion of the plasma as a whole. Nevertheless, as our simulations are performed in the frame of reference of the shear motion, this electric field vanishes. Therefore, the electric field present in the simulation is entirely due to the IC and Mirror waves.

Subset	Energy Range
Thermal Ions	$1.0999 < \gamma - 1 < 1.1$
Nonthermal Ions in 1st bump	$3.1 < \gamma - 1 < 3.5$
Nonthermal Ions in 2nd bump	$5.8 < \gamma - 1$

Table 3.1: Energy ranges for selecting the Test Particles in 2D

cases as well, being consistent with the continuous energy injection by the external shear motion. For the thermal subset of test particles, we can see that their average energy gain is dominated by the anisotropic heating, whereas the nonthermal subsets are clearly dominated by the work of the waves' electric field.

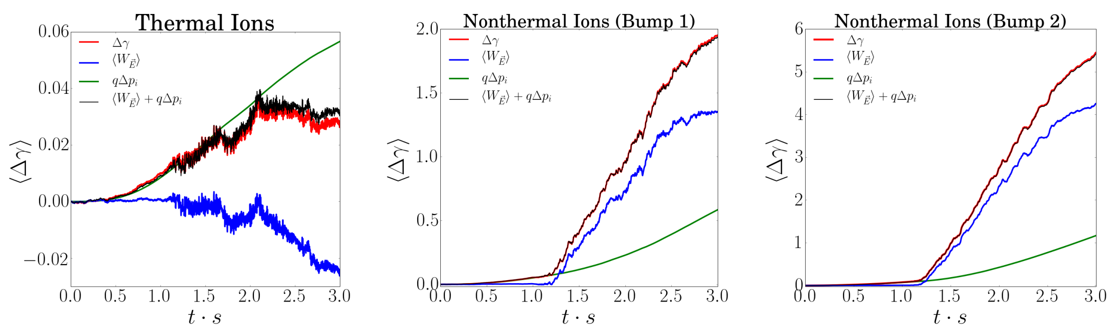

Figure 3.4: Evolution of the average energy gain by the test particles (red line), the average work done by the electric field of the IC waves (blue line), the average work done by the anisotropic viscosity associated to the shear (green line) and the sum of the electric field work and anisotropic viscosity work (black line) for thermal ions (left panel), nonthermal ions in the first bump (middle panel) and nonthermal ions in the second bump (right panel) as a function of time in simulation R20. (The $\langle\rangle$ denotes average over $N \sim 100$ particles and the pressure anisotropy Δp_i corresponds only to the selected test particles.) Note the difference of the scale in the $y-$axis of each figure. Note also that $\langle W_{\vec{E}}\rangle_p$ is negative for thermal ions whereas for nonthermal ones it is positive and dominates the energization.

The most notable feature comes when we compare the behavior of $\langle W_{\vec{E}}\rangle_p$. In the thermal subset $\langle W_{\vec{E}}\rangle_p$ is clearly negative, meaning that the waves are, on average, extracting energy from the thermal population. Conversely, as it is mentioned in the previous paragraph, in the nonthermal subsets $\langle W_{\vec{E}} \rangle_p$ is clearly positive and the main agent of energization of the particles; the contribution of the anisotropic heating is negligible in comparison. Therefore, and as there is no other agent in the system that could be doing work, the interpretation of the result is that the waves associated to the instabilities are acting as a mediator, and not transferring their own energy (e.g. à la Landau damping) between the two populations; the waves extract energy from the thermal particles and then transfer this energy to the smaller nonthermal population. This effect has been studied in the context of electron acceleration mediated by whistler waves in the radiation belts [53, 54, 55], and it would be very interesting to see if we are seeing here the same type of mechanism. The high energies that nonthermal particles can achieve compared with the average energy gain of the thermal ones is possible as the number of thermal particles is much larger than the number of nonthermal particles, so the waves can extract little energy per particle but having a huge population to do this, and then they give that energy to a very few nonthermal particles, so the net energy transfer could be significant.

As the real agent driving the acceleration of the particles could be the electric field associated to the waves, it is of interest to compare its behavior in the two $\beta_{i,\mathrm{init}}$ cases. In figure 3.5 we can see the fluctuations of the z component (i.e. the component out of the simulation plane) of the electric field for the two cases. These fluctuations show a clear spatial correlation of the electric field with the IC modes (see Figures 3.1c and 3.1f for comparison). This implies that the electric field associated to the IC modes is what is causing the non-thermal acceleration of the ions. This scenario is consistent with the fact that the amplitude of the z-component of the electric field is larger in the $\beta_i = 0.5$ case (the x- and y-components of the electric field show similar amplitudes), which corresponds to the case with the most efficient acceleration.

As the instability modes interact with the particles and start transferring energy between each other, this allows some fraction of them to accelerate to higher energies making the power-law tail. However, the purely growing nature of mirror modes

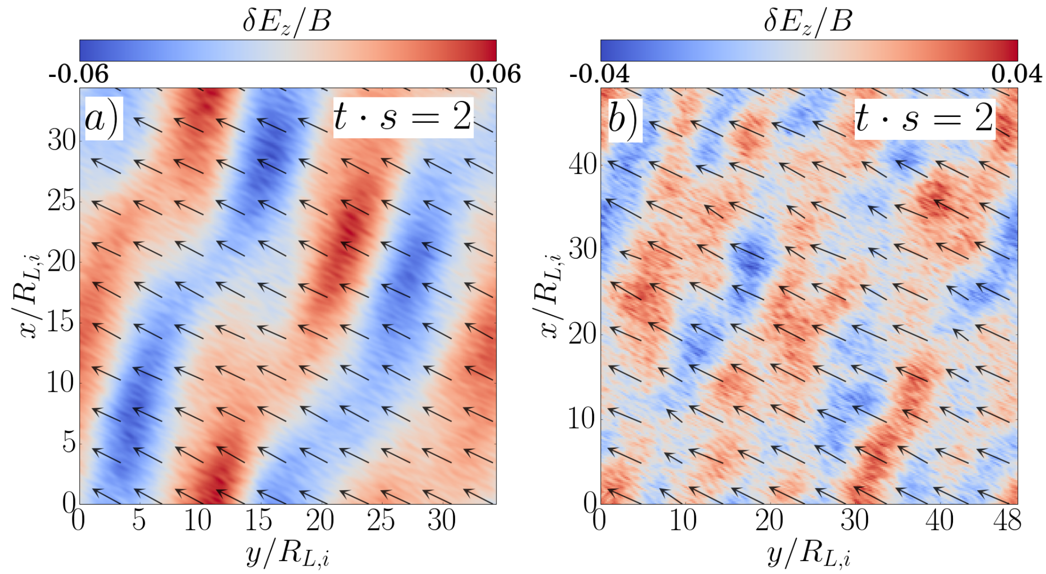

Figure 3.5: The z component of the electric field fluctuations normalized by B of simulation R1 for the $\beta_{i,\text{init}} = 0.5$ case (panel a) and simulation R13 for the $\beta_{i,\text{init}} = 2$ case (panel b) at $t \cdot s = 2$. The black arrows denote the direction of $\langle \vec{B} \rangle$. In both cases the electric field is clearly correlated with the IC modes, as can be seen from their orientation quasi-parallel to $\langle \vec{B} \rangle$.

(their real frequency is zero) makes them not to generate any electric field capable to do work on the particles. Conversely, the IC modes have a finite real frequency, which makes them capable to propagate and therefore have a net electric field associated. This electric field, which is given by the phase velocity of the IC waves, is responsible for the energy transfer and further acceleration of particles.

3.4 1D Simulations

Up to this point, in this work we have presented results of 2D simulations of the system in study. This scheme is desirable, as two dimensions are needed to capture the physics of IC and Mirror instabilities, with emphasis in the latter, because they always have wave vectors oblique to the mean magnetic field $\langle \vec{B} \rangle$, as seen in figure 3.1 (panels g,h). Unfortunately, PIC simulations, along with being capable to capture the evolution of the plasma in a self-consistent way, they have a computational cost that scales very quickly with simulation parameters and dimensionality, turning sometimes computationally intractable up to now. That limitation made us to perform the 2D simulations with values of relevant parameters not physically realistic. This is the case for the mass ratio m_i/m_e and the magnetization $\omega_{c,i}/s$. The dependence of the results on these two parameters is necessary to be studied, in order to ensure the effect is physically relevant and not only present in these space of parameters. In this section we show the results in 1D simulations of the same setup in order to push the values of the mass ratio m_i/m_e and the magnetization $\omega_{c,i}/s$ as far as possible (as 1D simulations are computationally much less expensive) in order to make sure that the main features seen before are not heavily dependent on these two parameters.

The simulation setup for 1D simulations is explained in detail in Appendix B , but it is essentially the same as 2D but now collapsing the dimension that is perpendicular to the direction of the mean magnetic field $\langle \vec{B} \rangle$, so now we just capture the dynamics occurring along the direction of $\langle \vec{B} \rangle$. This has the notable property that it allows us to keep capturing the development and further propagation of the IC modes, as they propagates parallel to $\langle \vec{B} \rangle$. This is key for the usefulness of 1D simulations, as the IC modes are the main actor in accelerating the ions. On the other hand, as mirror modes has wave vectors oblique to the mean magnetic field, in 1D we are not able to capture them. Therefore, our 1D simulations will be used only to study the case $\beta_i = 0.5$, where we know that the IC instability dominates for most of the simulation time and, therefore, where the non-thermal acceleration of the most efficient.

Our way to simulate a shearing plasma in 1D is new, and the present work constitutes the first time that this simulation method is being used. Thus, in order to show its accuracy, in what follows we compare our 2D results for $\beta_i = 0.5$ with analogous calculations using our 1D setup.

First, we compare the ion energy spectra of 1D simulation R3 and 2D simulation

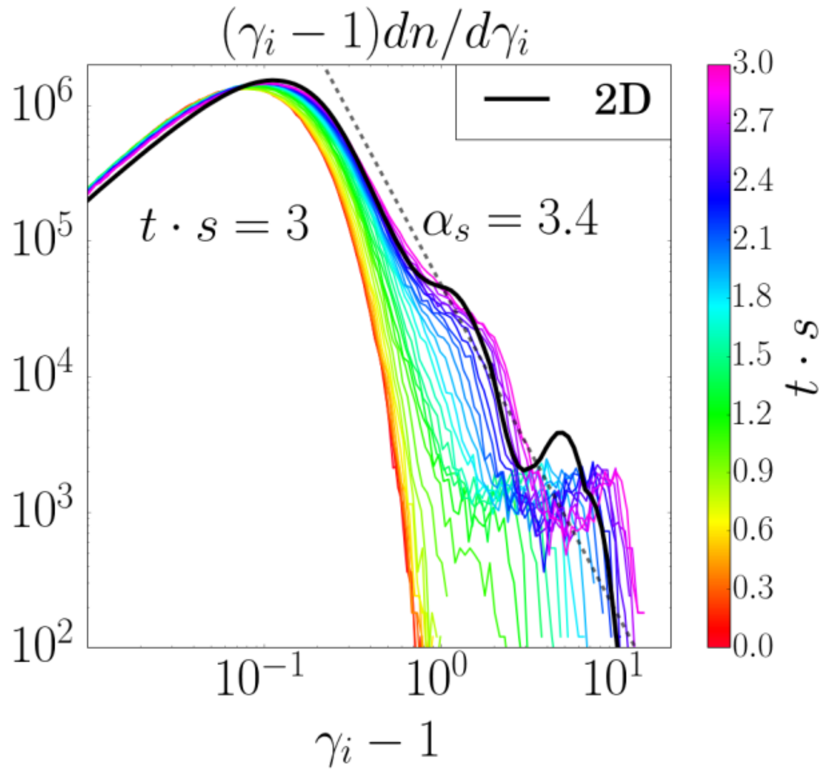

Figure 3.6: Ion energy distribution for simulation R3 for 1D (rainbow colors) with time indicated by the colorbar and the final energy distribution for simulation R1 for 2D (black thick line). At $t \cdot s = 3$, both 1D and 2D spectra can be described reasonably well by a power-law tail $dn/d\gamma \propto (\gamma - 1)^{-\alpha_s}$ with spectral index $\alpha_s = 3.4$ (dashed line) plus two bumps. The 1D spectra are scaled vertically so that both peaks coincide.

R1 at $t \cdot s = 3$ in figure 3.6. We can see that, aside from the noise in the 1D spectrum, both behaves almost exactly the same: we obtain the same nonthermal energy tail with the same spectral index α_s. Consequently, this is a strong indication that we are effectively capturing the same process of acceleration in 1D simulations.

Secondly, in figure 3.7 we compare the magnetic fluctuations in the z direction δB_z, where we can see more clearly the IC modes, in terms of the scales of the simulation box normalized by the initial Larmor radius of the ions. We compare here simulation R4 for 1D with simulation R1 for 2D. It can be seen that the wavelength of the IC modes are of the same order between 1D and 2D simulations.

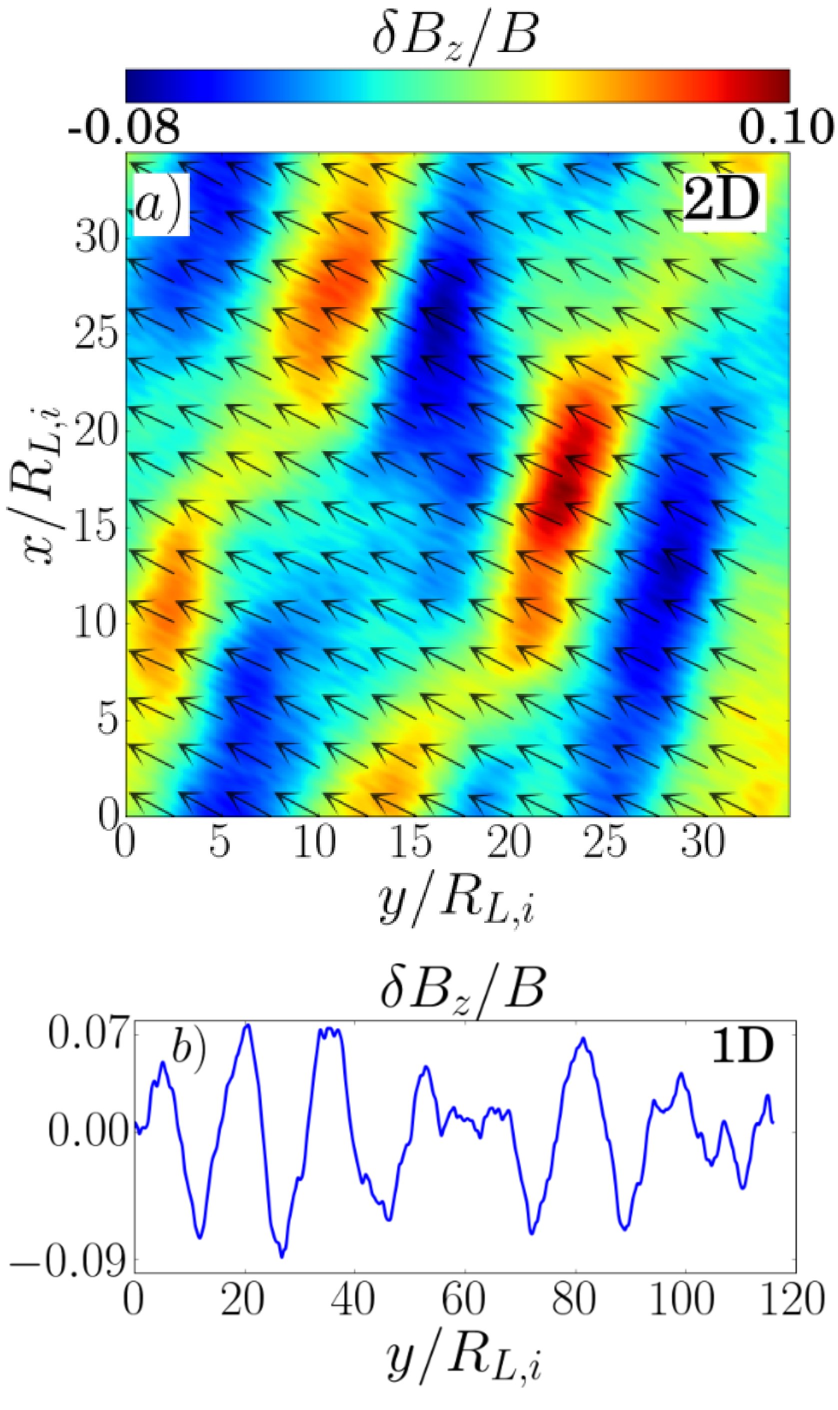

Figure 3.7: The magnetic fluctuations in the z direction δB_z normalized by B at $t \cdot s = 2$, for simulation R4 for 1D (panel b) and simulation R1 for 2D (panel a), both with $m_i/m_e = 2$, $\beta_{i,\text{init}} = 0.5$ and $\omega_{c,i} = 800$. Note that in both cases the dominant wavelength for the IC modes is roughly $\lambda_{IC} \approx 15R_{L,i}$.

In figure 3.8 we compare the evolution of the energy stored in $\delta\vec{B}$ for δB_z and $\delta B_\parallel$ components, that are the ones meaningful to compare with 1D simulations. The simulations shown here are the same as in figure 3.7. For the case of δB_z, in which the presence of the IC modes is more clearly revealed, the same growth is seen in the beginning but once the nonlinear regime is reached, the energy in this component is maintained in 1D while in 2D it drops to a lower value. This is produced by the fact that in 1D the mirror modes cannot be captured so they do not appear as they do in 2D, where they can develop and demote the IC modes to a subdominant role in later times.

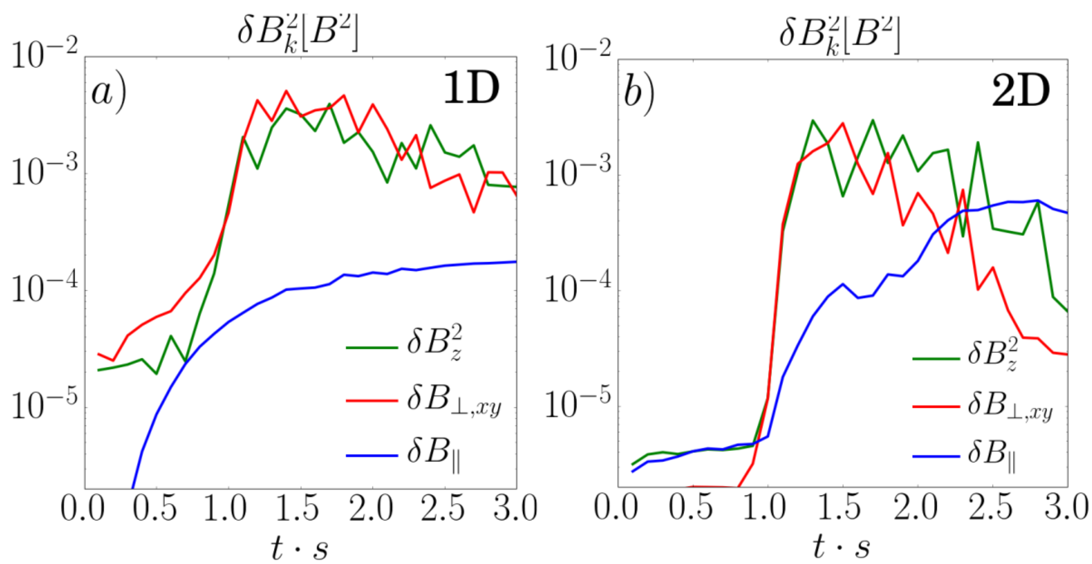

Figure 3.8: Evolution of energy stored in $\delta\vec{B}$ for simulations R4 in 1D (panel a) and R1 in 2D (panel b) for the components δB_z (green line), $\delta B_{\perp,xy}$ (red line) and $\delta B_\parallel$ (blue line). The different energies are normalized by B^2. The evolution is quite similar between 1D and 2D.

In the case of $\delta B_\parallel$, where mirror modes are expected to have a predominant presence, we see that in 2D they can develop and the energy can grow in later times while in 1D the energy in this component is very small at the beginning and it can grow up to $\delta B_\parallel \sim 10^{-3}$, being clearly sub-dominant. As for the case of the $\delta B_{\perp,xy}$ component, it captures part of the IC modes (as they are circularly polarized) and mirror modes, so in 1D they follow the same trend as the δB_z component as the mirror modes are clearly sub-dominant, while in 2D they decay quicker than δB_z, as IC modes start to fade away in favor of mirror modes at later times.

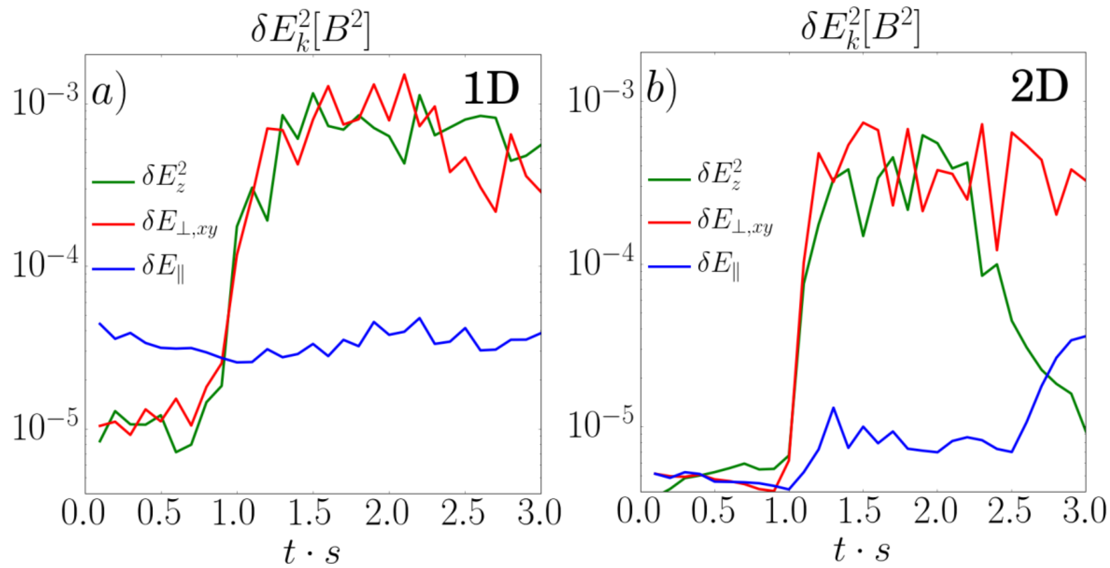

Figure 3.9: Evolution of the energy in $\delta \vec{E}$ for simulations R4 in 1D (panel a) and R1 in 2D (panel b) for the components δE_z (green line), $\delta E_{\perp,xy}$ (red line) and $\delta E_\parallel$ (blue line). The different energies are normalized by B^2. The evolution is quite similar between 1D and 2D.

Additionally, we also compare the evolution of the energy stored in $\delta \vec{E}$ in 1D and 2D in figure 3.9 for the same components as before: δE_z^2, $\delta E_{\perp,xy}^2$ and $\delta E_\parallel$. We can see that in both cases δE_z^2 and $\delta E_{\perp,xy}^2$ reach the same amplitude, with the 1D case presenting a slightly larger amplitude (panel 3.9a), and evolves similarly until $t \cdot s \sim 2.2$, where the main difference happens. After that time, δE_z^2 quickly drops in the 2D case (panel 3.9b), whereas in 1D it remains in the same level. This drop in 2D coincides with the rise of $\delta B_\parallel^2$, meaning that at later times mirror modes start to dominate over IC modes in the 2D case, whereas in 1D they do not appear as they cannot be fully captured. This absence of mirror modes in 1D also explains the overall larger amplitude of the perpendicular components δE_z^2 and $\delta E_{\perp,xy}^2$ in 1D compared to 2D.

Finally, we compare the evolution of the pressure anisotropy and the time derivative of the internal energy compared with the expected rate of heating by anisotropic viscosity in figure 3.10. The comparison is again using the same simulations R1 and R4. In the case of the anisotropy, in panel 3.10a, we can see qualitatively the same behavior both in the linear regime and when it saturates, and both curves coincide fairly well, except that the 1D curve evolves below the 2D curve (by about 10%) until almost the end of the simulation. In the case of the time derivative of the internal energy, in panel 3.10b, we see that in both 1D and 2D simulations the behavior is quite similar, so the effect of anisotropic heating is very well captured in 1D and 2D simulations.

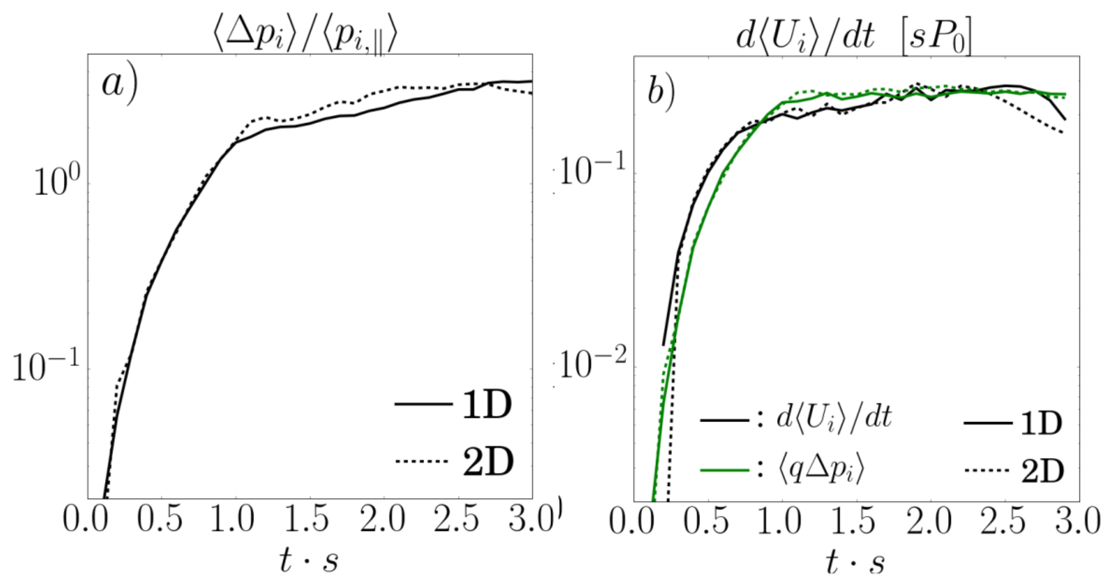

Figure 3.10: Evolution of the pressure anisotropy (left panel) and the time derivative of the internal energy of the ions along with the expected rate of heating by anisotropic viscosity (right panel) for simulations R4 for 1D (solid line) and R1 for 2D (dashed line). For both 1D and 2D runs the behavior of these quantities is quite similar.

Having passed these tests, we can ensure that the correct and relevant physics is properly captured when going to 1D simulations. Although it is inevitable to leave out the physics of mirror modes; in the case of simulations with $\beta_{i,\mathrm{init}} = 0.5$ this is not relevant since our main concern is to capture the physics of the ion acceleration. Now in 1D, we can push physical parameters further and, as we will see below, it turns out that the ion acceleration persists and does not suffer major changes in behavior.

3.5 Mass Ratio/Magnetization Dependence

In this section we show the results of 1D simulations and the scaling of our main results with larger mass ratios and magnetizations. We will see that the acceleration feature is robust under the scaling of these parameters; the net rate of acceleration is maintained and do not heavily depends neither of these two parameters. This is key for trying to justify this acceleration mechanism as a astrophysically relevant one.

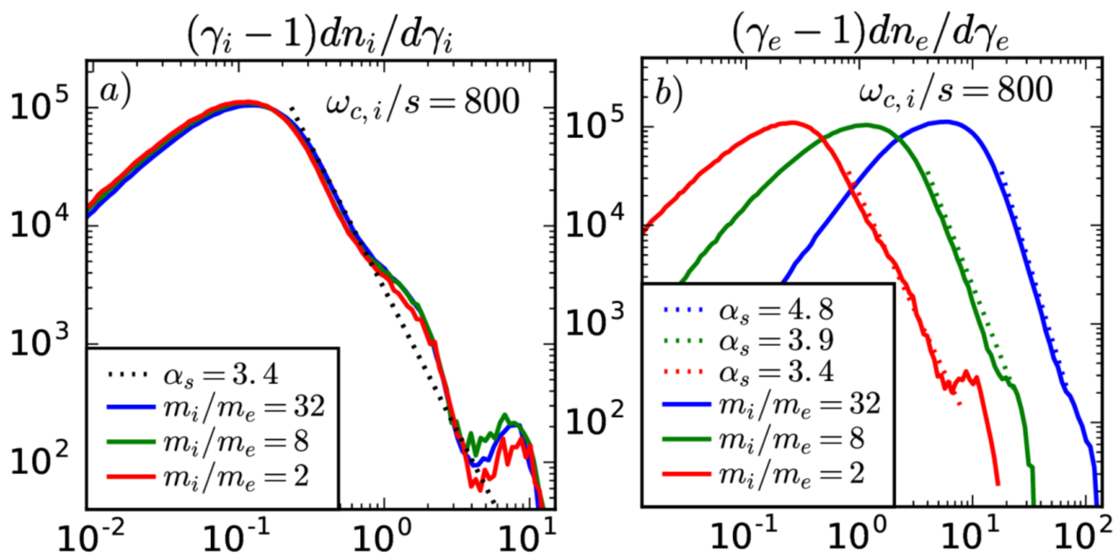

Figure 3.11: The energy distribution of ions (left panel) and electrons (right panel) for three different mass ratios of simulations R15 ($m_i/m_e = 2$), R16 ($m_i/m_e = 8$) and R17 ($m_i/m_e = 32$) with $\omega_{c,i} = 800$ at $t \cdot s = 3$. Not how the anisotropic heating is remarkably more relevant for electrons than for ions. The power-law tail becomes softer when increasing mass ratios in the case of electrons whereas in the case of ions it remains the same.

In order to know how the acceleration rate scales with the mass ratio, we compared three different 1D simulations, R15, R16 and R17 with three different mass ratios, $m_i/m_e = 2$, $m_i/m_e = 8$ and $m_i/m_e = 32$ respectively and the same magnetization of $\omega_{c,i}/s = 800$. This comparison can be seen in figure 3.11. Even though this thesis is focused in the dynamics of ions, in this case the evolution of the electrons is also shown to evidence how different the populations respond to the increase of the mass ratio and to emphasize the fact that R15, R16, R17 are indeed three different simulations with different mass ratios and not three runs with the same parameters. This is indeed what the spectra in figure 3.11a may suggest, given the remarkable overlap between the three curves.

In the case of ions, it can be clearly seen that the effect of the acceleration and the formation of the nonthermal tail is not sensitive to mass ratio at least in this range. Unfortunately, due to computational limitations we could not further increase the mass ratio to larger values. Nevertheless, this diagnostics supports the claim that the development of a nonthermal tail does not strongly depends on the mass ratio between ions and electrons. In the case of electrons, on the other hand, the mass ratio is critical, as it affects both the heating of the distribution as a whole and the hardness of the power-law tail, becoming softer as the mass ratio is increased.

Finally, we compare the behavior of the acceleration rate in the energy distributions for different, increasing magnetizations of $\omega_{c,i} = 800$, $\omega_{c,i} = 1600$ and $\omega_{c,i} = 3200$ for mass ratio of $m_i/m_e = 8$ for simulations R15, R18 and R19, respectively. The comparison can be seen in figure 3.12

We can see that the left "thermal" half of the distributions converge reasonably well, while when we go to the nonthermal tail we can see discrepancies for different magnetizations, especially to the end of the tail. The larger the magnetization, the harder is the tail. Although clearly in 1D we are not converging in magnetization, and therefore within this range of parameters we cannot say if the spectral index would converge to a definite value, the trend goes in the regime where the tail become harder, leaving interesting questions about the behavior of the acceleration to larger

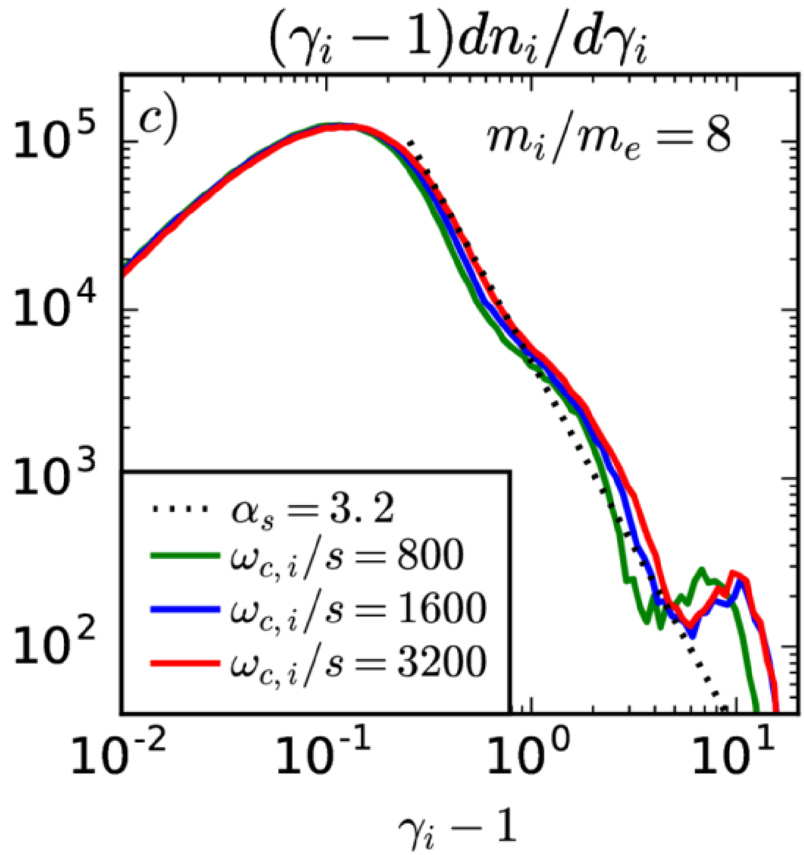

Figure 3.12: Ion energy distributions for three different magnetizations, $\omega_{c,i} = 800$, $\omega_{c,i} = 1600$ and $\omega_{c,i} = 3200$ and mass ratio of $m_i/m_e = 8$ at $t \cdot s = 3$ of simulations R15, R18 and R19 respectively.

and more realistic values of $\omega_{c,i}/s$.

We have seen that the growth of a nonthermal energy tail in the energy distribution of ions is a robust effect that weakly depends on the two most relevant physical parameters of the simulation, namely, the mass ratio $m_i/m_e = 2$ and the magnetization $\omega_{c,i}/s$. Although the values here evaluated are fairly modest compared with more realistic ($m_i/m_e \approx 1836$) and astrophysically relevant ($\omega_{c,i}/s \gg 1$) quantities, the trend is very clear; the acceleration rate tends to reach equal or larger values, giving the same or slightly harder nonthermal tails in the ion spectrum. Giving this, we can state that this acceleration mechanism can be an efficient way to energize particles in astrophysical environments with $\beta_i \lesssim 1$.

3.6 Test Particles in 1D

In section 3.3 we calculated the viscous heating and the work done by the electric field of the mirror and IC waves on different populations of ions in the 2D simulation R20. Our conclusion was that the small population of nonthermal ions got accelerated ultimately gaining energy from the larger population of thermal ions, and this process is mediated by the IC waves, in other words, the waves only act as a channel through which the thermal ions, on average, give energy to the waves and these waves, in turn, transfer that energy to the nonthermal population, accelerating them.

Here we perform the same analysis using the 1D simulation R11, again focusing in the $\beta_{i,\mathrm{init}} = 0.5$ case only. The ranges of $\gamma - 1$ we've selected are listed in Table 3.2.

Subset	Energy Range
Thermal Ions	$1.098 < \gamma - 1 < 1.102$
Nonthermal Ions	$2 < \gamma - 1 < 4$

Table 3.2: Energy ranges for selecting the Test Particles in 1D

The evolution throughout the simulation of these quantities can be seen in figure 3.13 for the three subsets. Essentially, we see the same behavior as in the 2D simulations described in section 3.3. As we enter to the nonlinear regime at $t \cdot s \sim 1$, the average energy is positive for both thermal and nonthermal particles, the thermal particles are dominated by the anisotropic heating and the nonthermal particles, both in the first and second bump, are dominated by the work of the electric field of the IC waves.

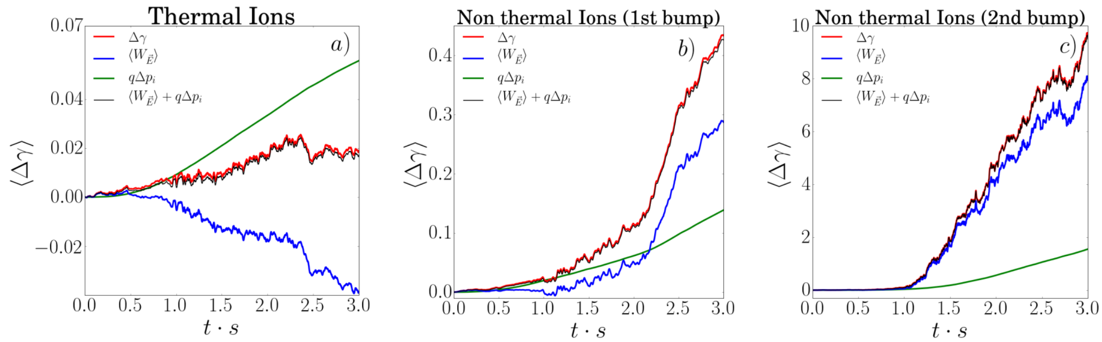

Figure 3.13: Evolution of the average energy gain by the test particles (red line), the average work done by the electric field of the IC waves (blue line), the average work done by the anisotropic viscosity associated to the shear (green line) and the sum of the electric field work and anisotropic viscosity work (black line) for thermal ions (left panel), nonthermal ions in the fist bump (middle panel) and nonthermal ions in the second bump (right panel) as a function of time in simulation R11. (The $\langle\rangle$ denotes average over $N = 100$ particles and the pressure anisotropy Δp_i corresponds only to the selected test particles.) Not the difference of the scale in the $y-$axis of each figure. Note also that $\langle W_{\vec{E}} \rangle_p$ is negative for thermal ions whereas for nonthermal ones is positive and dominates the energization.

Likewise, we also see here the same behavior as before relative to the work of the electric field associated to the IC waves; in the case of the thermal ions this work is negative, whereas in the two populations of nonthermal particles the work is positive as well. This way, in 1D simulation we also see that the IC waves are acting as a mediator between thermal and nonthermal particles, so on average thermal particles give energy to the nonthermal ones. With this final analysis we can be sure we are effectively capturing all the essential phenomena in our 1D simulations.

3.7 Ion Cyclotron Wave-Particle Interaction

We've seen that the ions interact with the IC waves in a fashion that on average ends with a strong energization of a small population of particles to higher energies. Now we will describe how this interaction is happening. Although there exists extensive literature for this specific type of wave-particle interaction and others, it involves complicated calculations from quasilinear formalism for treating these kind of velocity-space instabilities at the fully kinetic regime (e.g. see [56, 57]) that will rather obscure the discussion, so we will keep the discussion simple and focus on the physics of the interaction and referring to the corresponding literature for further exploration.

The Ion cyclotron instability [45, 58], sometimes also called the Ion cyclotron anisotropic instability [44] is triggered when we have a weakly collisional, magnetized plasma of electrons and ions in which the velocity distribution of ions becomes anisotropic, or, when averaging over velocity space, results in a pressure anisotropy $\Delta p = p_\perp - p_\parallel > 0$, or equivalently, $p_\perp > p_\parallel$. Given a plasma of these kind, the instability rests in the resonant interaction of ions with small-amplitude, left-hand polarized IC waves[4] propagating through the plasma, that is, when an IC wave with frequency ω encounters an ion rotating around the magnetic field with cyclotron frequency $\Omega = eB/mc$ and parallel velocity $v_\parallel$ such that the Doppler-shifted frequency of the wave to the reference frame of the ion, ω_s, matches the corresponding cyclotron frequency of the ion [59]:

$$\omega_s = \omega(\vec{k}) - k_\parallel v_\parallel = \Omega \tag{3.2}$$

When this condition[5] is fulfilled, the particle and the wave can exchange energy

[4]Ion cyclotron wave is part of the shear Alfvén waves branch, so it is a fundamental mode of a magnetized plasma. In particular, left-hand polarization is referring to electromagnetic waves with circular polarization in which the electric field rotates counterclockwise around the magnetic field, the same sense of ions.

[5]In general, the condition is written as $\omega_s = \omega(\vec{k}) - k_\parallel v_\parallel = l\Omega$, with l the lth harmonic of the cyclotron frequency, i.e., the electric field rotates l times around the magnetic field per cyclotron round. This way, the resonant interaction can happen with any harmonics. It is interesting to note that $l = 0$ corresponds to the well-known Landau resonance, and the cyclotron resonance here studied corresponds to $l = 1$.

efficiently. This energy exchange can result in a ion energization and consequent wave damping or the other way around, an energization of the wave at the expense of the ion, depending on the parallel velocity $v_{\parallel}$ of the ion. Analogously to Landau damping, if the ion has slightly larger parallel velocities compared to the phase velocity of the IC wave, $v_{\parallel} > v_{\phi} = \omega/k$, the ion lose energy to the wave. Therefore, additionally to the resonance condition, it is necessary to have a distribution function with more ions moving at higher speeds than the phase velocity of the wave, so the net effect is to transfer energy to the waves to be generated and therefore feed the instability. It is because of this that it is initially needed an anisotropic velocity distribution for the ions; it can be shown that this type of distribution is unstable to the generation of IC waves, in which the free energy that goes into the wave generation is stored in the anisotropy [60].

As we have seen in section 2.4, once the IC instability is developed and saturates, a quasi-stationary state is reached, in which the consequent ion acceleration also begins. In this state, the pressure anisotropy suffers, on one side, the continuous growth from the shear motion and, on the other side, the reduction of the anisotropy by the instability itself, that tries to regulate the level of anisotropy in the system. This regulation process is done by the pitch-angle scattering of ions by the IC waves, that, additionally to the energy transfer seen in section 3.3, it tries to randomize the velocity distribution of the ions, therefore reducing the level of anisotropy [59].

There are several works that claim that, in any system composed of waves and particles which also present linear wave growth or wave damping will tend to reach a quasi-stationary state, or marginally stable state [59, 50] in which there is no longer net growth or damping of the IC waves (i.e. the IC dispersion relation would have $\gamma(k) = 0$ for all k, where $\gamma(k)$ is the imaginary part of the complex wave frequency $\omega = \omega_r + i\gamma$). Although this state is expected at least theoretically, there are reasons to doubt if this is actually the case in our simulations. One important reason is related with the nature of the shear motion; as the box is being sheared continuously and the IC waves are generated and propagate parallel to $\langle \vec{B} \rangle$, and this magnetic field is also continuously changing its direction, there is a continuous growth of new IC waves at every timestep, as well as there's a continuous damping of the old ones at the same time, contrary to the scenario previously discussed. Therefore, even when there's a quasi stationary state in which a population of IC waves is maintained throughout the simulation, the population is continuously "recycling" itself, damping the first ones and growing new ones. Additionally, the newer waves should have different properties compared with the older ones, as at least a fraction of them would be generated by already accelerated particles, that in turn would resonate at other frequencies.

3.8 Plausible Astrophysical Applications

In this section we discuss several astrophysical contexts in which this acceleration of ions could take place. First of all, we discuss the long term behavior of the shearing motion since, although our simulations arbitrarily stop at $t \cdot s = 3$, there is no physical reason for the system to stop at that time. Questions regarding the inverse process of unshearing motion from an already sheared configuration and the combination of these two motions in a shearing-unshearing cycle are also addressed in light of discussing what would happen to the spectral index of the final power-law in the ion energy distribution. Secondly, we discuss the possibility of these accelerated ions to be initial seeds for other processes of acceleration such as Diffusive Shock Acceleration in shock waves. Finally we analyze the feasibility of having the acceleration process here studied in real astrophysical environments such as in the neighbourhood of Sgr A*.

3.8.1 Long-term Evolution of the System

Although all of our 2D and 1D simulations stop at $t \cdot s = 3$, there is no physical reasons at all to assume something special happens at this time, so it is of great interest to know what would happen in the long term. One of the most interesting questions in this regard is the behavior of the spectral index α_s with the shear. We've seen that the spectrum in our simulations still grows when we reach $t \cdot s = 3$ (see fig. 3.3), so it is still an open question if a convergence is reached at some point in the spectral index or not. If a further shearing implies a larger acceleration rate, the observed power-law tail could reach a harder spectral index in practice, given that in some astrophysical environment the system could have many more shearing times than just three.

Another interesting feature to analyse is the inverse process, namely, the unshearing of the box starting from an already sheared initial configuration. This is relevant because in the context of turbulent motion (A rather common ingredient in astrophysical environments) it is expected that the system suffers both shearing and unshearing motions at these scales. In the process of unshearing, the magnetic field now would decrease, and the anisotropy would be then $p_{\|,i} > p_{\perp,i}$, so there would be no cyclotron or mirror instabilities triggered, and the firehose instability would possibly arise instead [61]. This makes the process a completely different one that in principle could or could not continue accelerating the particles.

Finally, a more realistic approach to this problem would be to see the long term evolution of a system with several cycles of shearing and unshearing motions, in the context of a turbulent astrophysical environment. It is uncertain if this process would have any kind of convergence in the acceleration of the ions, but it can be argued that if in both shearing and unshearing motions a certain acceleration is present, the final spectral index would probably be harder than the $\alpha s \sim 3.4$ obtained in this study, making this mechanism a very promising process of acceleration.

3.8.2 Seed particles and the injection problem

In the context of Diffusive Shock Acceleration (DSA), there exists the so called "injection problem", in which it turns out that DSA can only accelerate particles whose energies are already several times the typical thermal energy, so the particles need to achieve a minimum energy first in order to be injected into DSA, otherwise they cannot be accelerated in the first place (see e.g. [62]). The question of how thermal particles can achieve that threshold energy cannot be explained within DSA theory. In this context, there have been several efforts to understand the evolution of DSA in a system with already accelerated particles, sometimes called "seed particles". This problem is relevant as long as the process of acceleration here studied could be a plausible mechanism for generating these seed particles by accelerating them from the thermal pool. Furthermore, this scenario could be of relevance in astrophysics, for instance, in the context of the shock propagation of SNR into the ISM, which is already filled with some population of cosmic rays. In this line, the work of Caprioli et al. [18] is worth to mention. They tackled the problem numerically, using hybrid plasma simulations (i.e. kinetic ions & fluid electrons). They include a population of thermal ions and seed particles already accelerated in a shock, and they found interesting differences in the development of DSA with respect to the case with thermal particles only. They found an enhancement of the acceleration efficiency for oblique shocks, unlike the old case in which for angles $\vartheta \gtrsim 60°$ the acceleration efficiency becomes negligible. This happens because the reaccelerated seed particles drive a non-linear back-reaction into the plasma triggering the streaming instability and amplifying the magnetic field, introducing turbulence into the system. Furthermore, in this non-linear regime and for quasi-perpendicular shocks now ($\vartheta \gtrsim 70°$), two intriguingly new phenomena arise: the acceleration of ions by turbulence (and not DSA anymore!) driven by the seed particles themselves and a re-acceleration of these seed particles to a spectrum that does not depend on the compression ratio only, as DSA classically predicts. Consequently, the mechanism of acceleration studied in this thesis could be a promising candidate to explain the origin of these seed particles, as an alternative to the assumption of the pre-existence of an already energetic population of particles (e.g. cosmic rays within the ISM). This mechanism can be even part of the same DSA process, as a secondary acceleration by turbulence in the same region where shock acceleration is acting or nearby. A more careful analysis of this ideas could be a very interesting pathway for future works.

3.8.3 The case of Sgr A*

Sagittarius A* (Sgr A*) is a bright and compact radio source located at the Galactic Center. Observations of the dynamics of nearby S-stars have determined that it coincides with the location of the Supermassive Black Hole (SMBH) of the Galaxy, with a mass of $4 \times 10^6 M_\odot$ and a bolometric Luminosity of $L_{bol} \approx 10^{36}$ erg s^{-1} in the quiescent state. This luminosity is ~ 9 orders of magnitude lower than the Eddington luminosity for a SMBH of that mass [63], whereas its accretion rate is ~ 7 orders of magnitude lower than the Eddington accretion rate [64].

Observationally speaking, Sgr A* has been detected mainly in radio, sub-mm, NIR and X-ray. It presents a strong, rapid variability in NIR and X-rays and periodic episodes of very bright flares [65]. This variability is also temporally correlated between sub-mm, NIR and X-rays [29]. This indicates that the source of these emissions could be a population of relativistic electrons near the SMBH which emits synchrotron radiation from radio to NIR, while X-rays arise from inverse Compton or synchrotron self-Compton scattering [66].

Recent observational and theoretical works have suggested that in order to fully explain the emission from Sgr A* , non-thermal populations of electrons (for sub-mm, NIR and X-rays)[29, 67] are necessary. Furthermore, in 2006 The HESS collaboration reported gamma-ray emission in an extended region around Sgr A. The spatial correlation found between them and molecular gas indicates that the origin of this emission is hadronic [68]. Additionally, a more recent study has shown evidence for the extended emission around Sgr A* to be originated by hadronic CRs accelerated within 10 pc from Sgr A*, which points to the accretion flow in this system as a viable source of acceleration of these particles [69]. Remarkably, whatever is accelerating CRs within this region, is being able to accelerate them to PeV energies, which is what is needed to explain the spectrum of cosmic rays until the so called "knee". To date, the standard paradigm for the acceleration of CRs to PeV energies −namely, DSA at supernova remnant shocks− has not shown convincing evidence of being able to reach such high energies [15], which emphasizes the importance of what is found in [69].

The conditions of low luminosity and low accretion rate of Sgr A* cannot be explained by the common geometrically thin, optically thick models [70], which predict a typical luminosity $L \approx 0.1\dot{M}_B c^2 \sim 10^{41}$ erg s^{-1}, five orders of magnitude larger than the observed luminosity of Sgr A* (see e.g. [71]). Instead, these types of environments are well described by Radiatively Inefficient Accretion Flow (RIAF) and Advection-Dominated Accretion Flow (ADAF) models, which consider instead a geometrically thick, optically thin disk where a very small fraction of the gravitational potential energy is converted into radiation as the material is accreted; the majority of it is converted to thermal energy and advected into the black hole instead [72].

This way, Sgr A* can be described as a hot, low density, ionized plasma. In these conditions, it is expected that protons and electrons have different temperatures. Assuming that the majority of the energy goes into thermal energy and the system is virialized,

$$\langle KE \rangle \sim k_B T_s \sim \frac{GMm_s}{R_S} \tag{3.3}$$

With T_s the temperature of the species s, m_s the mass of the species s, $M \approx 4 \times 10^{-6} M_\odot$ the mass of the SMBH of Sgr A* and $R_S = 2GM/c^2 \sim 10^{12}$ cm its

Schwarzschild radius. Therefore, the expected temperature for protons is $T_p \sim 10^{12}$ K near the black hole horizon. The estimate of the electron temperature cannot be estimated by the same reasoning as protons, however. These two species are expected to decouple to each other due to the absence of Coulomb collisions between them. This, plus the fact that electrons cool down more efficiently than ions, implies that electron are in principle significantly cooler than the ions. This thermal decoupling betwen ions and electrons can be checked, to orders of magnitude, by comparing the typical thermalization times between electrons and ions[6], t_{thermal}, with the typical accretion time t_{acc} in ADAF models, from a distance of the order of the black hole horizon, let's say around $R \sim 100R_s$,

$$t_{\text{thermal}} = \frac{1}{\nu_{eq}^{e-i}} = \frac{3(2\pi)^{1/2}\pi m_e m_i (4\pi)^{-2}(v_e^2 + v_i^2)^{3/2}}{e^2 q_i^2 n_e \ln \Lambda^{(e,i)}} \tag{3.4}$$

$$t_{\text{acc}}(R) \sim \frac{R}{v_R} = \frac{R}{\alpha c_s} \tag{3.5}$$

Where m_e, m_i are the masses of electrons and ions, respectively, $v_s \sim \sqrt{k_B T_s/m_s}$ the velocity of the species s, e the electron charge, q_i the electric charge of the ions, n_e the density of electrons, $\ln \Lambda^{(e,i)}$ is the Coulomb logarithm and $v_R \sim \alpha c_s H/R$ is the radial velocity of the flow, where we have set $H/R \sim 1$ as disks are geometrically thick in ADAF models [72]. Finally, $c_s = \sqrt{k_B T_e/m_i}$ is the sound speed of the gas and α is the usual dimensionless Shakura-Sunyaev viscosity parameter [70].

The typical density is well constrained at the Bondi radius $R_B \sim 10^5 R_S$ by X-ray observations, and it is found to be $n_B \sim 100$ cm^{-3} [74]. Closer to the SMBH the values are uncertain, but by means of GRMHD simulations, several works have been found scalings for the density profile of $n \propto r^{-1}$ [75, 76]. Adopting such scaling, at distances of $R \sim 10 - 100R_s$ the density has the value $n(R) \sim 10^6$ cm^{-3}. In these conditions, considering $T_p \sim 10^{12}$ K, a rough estimate for $T_e \sim 10^{10}$ K and $\ln \Lambda \sim 20$,

[6] For this thermalization time we use the inverse of the thermalization frequency defined in eq. C14 of [73].

we obtain $t_{\text{thermal}} \sim 10^3$ yr. Furthermore, adopting $\alpha \sim 0.01$ we obtain $t_{\text{acc}} \sim 10^{-1}$ yr, so we can safely consider the plasma surrounding Sgr A* as a collisionless plasma. Furthermore, Sgr A* is believed to be magnetized ($B \sim 30$ G [77]). These facts, along with the discovery of the first PeVatron in the vicinity of Sgr A*, which means that acceleration of particles (and in particular ions) is indeed present, makes this environment a suitable one to test the kind of acceleration processes like the one studied in this thesis. In particular, there exist regions in accretion disks where $\beta \lesssim 1$, for instance in the corona [78], and also in ADAF [28]. This is important as we have seen that the mechanism of acceleration is more efficient around those values of the plasma beta.

Although it is still too soon to give a direct prediction of how efficient this mechanism would be to accelerate protons in the surroundings of the Galactic Center given our limitations on mass ratio, magnetization and dynamical ranges, we can at least compare the timescales for the development of the IC instability, $t_{IC} \sim s^{-1}$ (i.e. when $t \cdot s = 1$, see section 2.4) in our system and the typical lifetime of a particle in the accretion disk, t_{acc},

$$t_{IC} = s^{-1} = \frac{2}{3}\left(\omega_0(r = 100R_s)\right)^{-1} = \frac{2}{3}\sqrt{\frac{(100R_s)^3}{GM}} \sim 10^{-4} \text{ yr} \tag{3.6}$$

Where we have considered the shear frequency $s = 3\omega_0(r)/2$ for the case of a Keplerian disk [79] with the angular velocity at $r = 100R_s$. We can see that t_{IC} is much smaller than t_{acc}, so in the accretion disk of Sgr A* the IC instability has plenty of time to develop and generate enough turbulence to start to pitch-angle scatter the particles. With this brief analysis we can confirm that the Galactic Center is one of the best candidates for testing this and other mechanisms of acceleration driven by turbulence in collisionless plasmas.

Chapter 4

Conclusions

In this Master thesis we've performed 2D and 1D Particle-In-Cell (PIC) simulations to study the acceleration of ions by the resonant interaction with ion-cyclotron (IC) waves generated by the IC instability in a collisionless, magnetized plasma with a growing magnetic field. Many astrophysical plasmas have densities sufficiently low to have a particle mean free path much larger than the scales of the system, or the collision frequency much smaller than the inverse of the typical macroscopic time scale of the system, so they behave as collisionless plasmas. In absence of collisions, the plasma becomes inefficient in distributing the energy and it is expectable that populations of energetic particles (i.e. with energies far exceeding the thermal energy of the plasma) naturally start to arise. Furthermore, evidence of the existence of energetic and very energetic particles (mostly protons) in the Universe is nowadays profuse and conclusive, constituting a ubiquitous component of the Universe at almost all scales from the Solar System to the ICM. Here we studied a prospective mechanism of stochastic acceleration of ions by the scattering of IC waves in a magnetized, collisionless plasma subject to an imposed shear motion which can mimic a very general astrophysical situation, such as the differential rotation of a low-luminosity accretion disk around a compact object or an incompressible, large-scale MHD turbulence.

After giving a broad introduction on the properties of cosmic rays and a description of the two most classical mechanism of acceleration, namely, first and second order Fermi mechanisms (See Chapter 1), along with an introduction of the essentials of the Particle-In-Cell numerical method, the numerical setup and initial configuration of our simulations was presented along with a list of a representative set of the simulations run for this study (see Chapter 2). On Chapter 3 we present our main results, in which we initially run 2D simulations where we explored two regimes of initial plasma beta, $\beta_{i,\mathrm{init}} = 0.5$ and $\beta_{i,\mathrm{init}} = 2$. Although in both cases a net acceleration is present so we could see the growth of a nonthermal power-law tail in the ion energy distribution, in the $\beta_{i,\mathrm{init}} = 2$ case the acceleration was fairly weak compared with the $\beta_{i,\mathrm{init}} = 0.5$ case, for which a spectral index of $\alpha_s = 3.4$ was obtained. A thorough analysis of the numerical convergence of these simulations was carried out, ensuring the results were robust numerically speaking. Another analysis of physical convergence was also carried out for the mass ratio parameter, m_i/m_e and magnetization parameter $\omega_{c,i}/s$, because initially we used fairly unrealistic values for each of them compared to astrophysical environments, due to the computational limitations current facilities impose in our simulations. In order to do these tests, we perform 1D simulations which are cheaper computationally speaking, so we could be able to push these parameters to higher values and check if the net acceleration of ions and power-law tail growth was maintained so our results could be relevant in astrophysical environments. Before doing that, however, we had to make sure the 1D implementation of the code should be capturing all the relevant physics present in 2D. In 1D simulation, only the dynamics along the shearing, amplifying mean magnetic field $\vec{B}$ is resolved, so we could follow the growth of the IC instability and further propagation of IC waves as before in 2D, but with the caveat of losing resolution in resolving mirror modes, which are oblique to the mean magnetic field. This last factor, nevertheless, didn't play a major role on the energization of ions in the plasma. Instead, the further growth of IC waves is slightly damped in the saturated regime, so the absence of them in 1D simulation only result in an artificial, slightly higher growth of IC waves, resulting in a slightly higher acceleration of ions. Nevertheless, the effect is rather small and did not interfere with the main results.

Once we made sure that 1D simulations were capturing the relevant physics of the acceleration, we could test how the mass ratio m_i/m_e and magnetization $\omega_{c,i}/s$ affect the results. Comparing values of $m_i/m_e = 2$, $m_i/m_e = 8$ and $m_i/m_e = 32$ we could observe that the power-law tail is maintained and even grows a little in the latter case, whereas for the magnetization we compared $\omega_{c,i}/s = 800$, $\omega_{c,i}/s = 1600$ and $\omega_{c,i}/s = 3200$ and the power-law tail was also maintained, with little discrepancies especially to the end of the nonthermal tail but towards the positive side; the larger the magnetization, the slightly harder the tail. This effect leaves interesting questions about the behavior of the tail for larger values of $\omega_{c,i}/s$. This way, even when the parameter values were not close to real ones, we could confirm that the effect is robust and could happen under suitable conditions in astrophysical plasmas.

We also wanted to shed light on how the ions were energized. For this purpose we use a "Test Particle" technique in which a convenient subgroup of particles can be followed throughout the whole simulation and see how properties such as their velocity, energy and values of the electromagnetic field nearby their positions vary as the particles move around the plasma. In particular, we wanted to compare the evolution of the energy of the so called thermal particles (i.e. the ones that stay in the low-energy side of the energy distribution at the end of the simulation) with the nonthermal ones (the ones in the tail). The two only agents responsible to energize the particles were the anisotropic heating coming from the shear and the electric field associated with the IC waves, that when interacts with the particles resonantly could interchange energy efficiently. Quite intriguingly, aside from the anisotropic heating acting on all the particles in the same way, a notable difference was discovered in the behavior of the electric field. When dealing with thermal particles, the work done by this electric field was negative on average, whereas for nonthermal particles it was clearly positive. This scenario can be interpreted as the IC waves extracting energy from the thermal particles and giving it to the nonthermal ones, so this process is different from the typical wave-particle interaction in which the wave gets damped at the expense of giving its energy to the particle. Instead, here the IC waves act as a mediator between thermal and nonthermal particles, taking energy from the former and giving it to the latter. We have also seen that the energy gain of the nonthermal particles are about an order of magnitude larger than the energy gain or lose of the thermal particles. Conversely, the nonthermal population is about $\sim 10\%$ of the total, so even when the average energy the IC waves take from a thermal particle is small, the contribution of the whole thermal population can on average transfer a huge amount of energy to the small population of nonthermal particles.

After this analysis, we explored some plausible astrophysical applications of this acceleration mechanism and how can we test them by laying down guidelines to future work. First, we discussed the long-term evolution of the system. Since there are no astrophysically motivated reasons for running our simulations until $t \cdot s = 3$, it will be part of the future analysis to study the evolution of the system with more shearing times. Secondly, it was discussed what would happen in a system subject to a inverse shearing motion, or to "unshear" the box, so instead of amplifying the magnetic field, it would be reduced. This is motivated by the fact that in a system subject to MHD turbulence (e.g. MRI) or with differential rotation, both the shearing and unshearing motions are possible. Certainly this effect would no longer trigger mirror or IC, since the anisotropy now would be $\Delta p_i < 0$, but instead, the firehose instability could arise and then it would be very interesting to see if that instability could produce a type of acceleration mechanism by itself. Finally, a more complete and astrophysically relevant picture of the analysis can be done by considering both shearing and unshearing motions continuously happening, as this should be closer to the real scenario of a turbulent astrophysical environment.

Another interesting application it was discussed was in the context of the injection problem in Diffusive Shock Acceleration (DSA). It turns out that DSA needs an already energetic population of particles in order to be sufficiently efficient in the process of acceleration, the so called “seed particles”. In consequence, particles extracted directly from the thermal pool are not able to enter into the shock front and be further accelerated. However, we could see that the mechanism of acceleration studied in this thesis is able to accelerate particles from an initial thermal population, so if the conditions in the surrounding of a collisionless shock are fulfilled for this type of acceleration to be efficient, this mechanism is a promising candidate for generating the seed particles in first place that can further enter in DSA afterwards. The inclusion of seed particles in the process of DSA has been studied recently [18] and it can considerably change the results compared with the process of DSA without seed particles.

Finally, we discussed if Sgr A* , the supermassive black hole at the center of the Galaxy, can be a plausible astrophysical environment that can harbour an acceleration process like the one here studied. We showed that the plasma that surrounds Sgr A* has conditions that makes it collisionless at distances of the order of hundreds of the Schwarzschild radius, and it is fairly magnetized as well. Furthermore, there are regions in ADAF where the condition of $\beta_i \lesssim 1$ is fulfilled. Even when we are aware of the limitations on the physical parameters used in the simulations, we compared the timescales for the development of the IC instability in Sgr A* with the typical timescale it takes to the plasma to be accreted into the SMBH in order to know if the instability has enough time to develop properly. It turns out that the IC instability has plenty of time to develop and saturates compared with the accretion timescale, so we can expect to have the IC instability present and saturated. With this analysis, Sgr A* constitutes a promising environment in which the acceleration mechanism studied can be tested.

Appendices

Appendix A

Some results of Plasma Physics

A.1 Adiabatic Invariance of Magnetic Moment

One key feature in our simulations is the invariance of the ion magnetic moment $\mu_i = \frac{m_i v_{i,\perp}^2}{2B} = W_{i,\perp}/B$, that allows the perpendicular momentum $p_\perp$ to be amplified, so the pressure anisotropies can grow. Here we outline a brief but insightful derivation of this key feature of weakly collisional plasmas. A formal derivation of adiabatic invariance in general make use of Hamiltonian mechanics and Poincaré invariants $\oint pdq$ (See e.g. [80]).

The idea behind adiabatic invariance is that in any periodic motion, there are some quantities which are conserved under a slowly enough variation of relevant parameters of the system, with "slowly enough" meaning that the typical frequency of the periodic motion is much larger than the rate of change of these relevant parameters. In the case of μ_i, the periodic motion is clearly the gyromotion of the ion around the magnetic field, and the invariance is under a slow variation of B (i.e. $\omega_{c,i} \gg \frac{d\ln B}{dt}$). It can be formally shown [80] in general that the change in μ_i is $\Delta\mu_i \propto \exp(-\omega_{c,i}/\Omega)$ with Ω the frequency at which B varies. Let us find, then, the change in μ_i over one orbit of the ion around the magnetic field. It is easier to show this in the frame of reference moving longitudinally with the ion. In this frame of reference we have a changing magnetic field and consequently an electric field satisfying $c\nabla \times \vec{E}' = -\partial \vec{B}'/\partial t$. Let's denote the variation in time of a quantity f over one gyro-orbit as:

$$\Delta f \equiv \int_0^{2\pi} \frac{d}{dt} f(\phi) d\phi \tag{A.1}$$

We have,

$$\begin{aligned} \Delta W_{i,\perp} &= \Delta(\mu_i B) \\ &= B\Delta\mu_i + \mu_i \Delta B \end{aligned} \tag{A.2}$$

So then,

$$\begin{aligned} \Delta\mu_i &= \frac{1}{B}\int_0^{2\pi} \frac{d}{dt}\left(\frac{1}{2} m_i v_{i,\perp}^2\right) d\phi - \frac{1}{B}\mu_i \Delta B = \frac{1}{B}\int_0^{2\pi} m_i \frac{d\vec{v}_\perp}{dt} \cdot \vec{v}_\perp d\phi - \frac{1}{B}\mu_i \Delta B \\ &= \frac{1}{B}\int_0^{2\pi/\omega_{c,i}} m_i \frac{d\vec{v}_\perp}{dt} \cdot \vec{v}_\perp \omega_{c,i} dt - \frac{1}{B}\mu_i \Delta B \\ &= \frac{\omega_{c,i}}{B}\int_0^{2\pi/\omega_{c,i}} q\vec{E}' \cdot \vec{v}_\perp dt - \frac{1}{B}\mu_i \Delta B \\ &= \frac{\omega_{c,i}}{B}\oint q\vec{E}' \cdot d\vec{\ell} - \frac{1}{B}\mu_i \Delta B = -\frac{q\omega_{c,i}}{cB}\int \frac{\partial \vec{B}}{\partial t} \cdot d\vec{S} - \frac{1}{B}\mu_i \Delta B \\ &= \frac{q\omega_{c,i}}{cB}\frac{R_{L,i}^2}{2}\int_0^{2\pi} \frac{\partial B}{\partial t} d\phi - \frac{1}{B}\mu_i \Delta B = \frac{q\omega_{c,i}}{cB}\frac{R_{L,i}^2}{2}\Delta B - \frac{1}{B}\mu_i \Delta B \\ &= \frac{m_i v_{\perp,i}^2}{2B}\frac{\Delta B}{B} - \frac{1}{B}\mu_i \Delta B = \frac{1}{B}\mu_i \Delta B - \frac{1}{B}\mu_i \Delta B = 0 \end{aligned} \tag{A.3}$$

where we recognize that $d\vec{S}$ and $\partial\vec{B}/\partial t$ have opposite directions as an ion orbits around the magnetic field oppositely to electrons, $R_{L,i} = v_{\perp,i}/\omega_{c,i}$ and $\omega_{c,i} = qB/m_i c$. This way, we've shown that the magnetic moment of the ions is conserved under a gyro-orbit.

A.2 Flux Freezing

Another important feature is the magnetic field amplification due to the imposed shear motion, that takes place because the magnetic field lines move along with the plasma, because the magnetic flux is frozen to the plasma. This is a central result of ideal magnetohydrodynamics, and there are various ways to derive it. We will choose a simple derivation emphasizing the physical insight of it. The key assumption hereafter is to assume the limit in which the plasma has infinite electrical conductivity (or zero resistivity). This condition is easily achieved in large-scale astrophysical plasmas. The derivation will closely follow the one by Fitzpatrick[1]. We start from the magnetic flux:

$$\Phi_B = \int_S \vec{B} \cdot d\vec{S} \tag{A.4}$$

Through a contour C with a surface S moving along with the plasma. The time derivative of the magnetic flux Φ_B has two contributions as both $\vec{B}$ and the contour C change with the motion of the plasma. The contribution of the magnetic field can be written:

$$\left(\frac{\partial \Phi_B}{\partial t}\right)_B = \int_S \frac{\partial \vec{B}}{\partial t} \cdot d\vec{S} = -\int_S c\nabla \times \vec{E} \cdot d\vec{S} \tag{A.5}$$

While the contour varies along with the plasma flow, so we have to calculate the amount of flux passing through the area this contour creates as it moves. If $d\vec{\ell}$ is an element of C, then the area generated by the flow motion is $\vec{U} \times d\vec{\ell}$, with $\vec{U}$ the bulk velocity of the plasma. This way, the flux passing through this area is simply $\vec{B} \cdot \vec{U} \times d\vec{r}$. Then this contribution can be written:

$$\left(\frac{\partial \Phi_B}{\partial t}\right)_C = \int_C \vec{B} \cdot \vec{U} \times d\vec{r} = \int_C \vec{B} \times \vec{U} \cdot d\vec{r} = \int_S \nabla \times (\vec{B} \times \vec{U}) \cdot d\vec{S} \tag{A.6}$$

[1] `https://farside.ph.utexas.edu/teaching/plasma/Plasma/node87.html`

Where we've used Stoke's Theorem in the last step. Adding these two parts:

$$\left(\frac{\partial \Phi_B}{\partial t}\right) = \left(\frac{\partial \Phi_B}{\partial t}\right)_B + \left(\frac{\partial \Phi_B}{\partial t}\right)_C = -\int_S \nabla \times (c\vec{E} + \vec{U} \times \vec{B}) \cdot d\vec{S} \qquad \text{(A.7)}$$

Now we recognize the term in brackets as the Ohm's Law in the infinite conductivity limit, and we know from ideal MHD that is equal to zero:

$$c\vec{E} + \vec{U} \times \vec{B} = 0 \qquad \text{(A.8)}$$

This way, we obtain the result:

$$\left(\frac{d\Phi_B}{dt}\right) = 0 \qquad \text{(A.9)}$$

Note that the infinite conductivity limit implies that the induction equation is written:

$$\frac{\partial \vec{B}}{\partial t} = \nabla \times (\vec{U} \times \vec{B}) \qquad \text{(A.10)}$$

Where the resistive term is neglected. In the case of our simulation setup, we have an initial magnetic field $\vec{B} = B_0\hat{x}$, and a shear velocity field of the form $\vec{U} = -sx\hat{y}$, so from eq. A.10 we have:

$$\frac{\partial \vec{B}}{\partial t} = \nabla \times (-sxB_0\hat{y} \times \hat{x}) = \nabla \times (-sxB_0\hat{z}) = -sB_0\hat{y} \qquad \text{(A.11)}$$

So that the y component of the magnetic field evolve as $\frac{\partial B_y}{\partial t} = -sB_0$, implying a net amplification of the magnetic field.

A.3 Anisotropic Viscous Heating

One important phenomenon present in our simulations is the heating of the ions produced by the pressure anisotropy. The behaviour is quantified in equation 3.1:

$$\frac{\partial \mathscr{E}_i}{\partial t} = q\Delta p_i$$

where $\mathscr{E}_i$ is the internal energy of the ions, $q = \frac{1}{B}\frac{dB}{dt}$ is the growth rate of the magnetic field, that in our case is related with the shear frequency s, and $\Delta p_i = p_\perp - p_\parallel$. This relation is a result of the nonzero viscous stress that the anisotropy gives rise to, and has the general form $\overleftrightarrow{\sigma}_s : \nabla \vec{U}_s$[2], with $\overleftrightarrow{\sigma}_s$ the traceless part of the pressure tensor $\overleftrightarrow{P}_s$ and U_s is the bulk velocity of the plasma. To derive this relation we have to make use of Vlasov equation and take the trace of its second moment.

The Vlasov equation, in its general form, can be written as eq. 2.1:

$$\frac{\partial f_s}{\partial t} + \frac{\vec{p_s}}{\gamma m_s} \cdot \frac{\partial f_s}{\partial \vec{r}} + q\left(\vec{E} + \frac{\vec{v} \times \vec{B}}{c}\right) \cdot \frac{\partial f_s}{\partial \vec{p_s}} = 0 \tag{A.12}$$

Where the s stands for the particle species. From this equation it is possible to obtain relations for the evolution of macroscopic quantities of the plasma by taking its "moments" , that is, multiplying by successively higher powers of $\vec{v}$ and integrating over velocity space. This way, the zeroth order moment of Vlasov equation can be written:

$$\int d^3v\, \frac{\partial f}{\partial t} + \int d^3v\, \vec{v} \cdot \frac{\partial f}{\partial \vec{r}} + \int d^3v\, q\left(\vec{E} + \frac{\vec{v} \times \vec{B}}{c}\right) \cdot \frac{\partial f}{\partial \vec{p}} = 0 \tag{A.13}$$

With a little of algebra, integration by parts (assuming that $f(\vec{r}, \vec{v}, t)$ decays to zero at infinity sufficiently fast) and recalling that

[2] As a matter of notation, the double dot product here denotes the following: $\overleftrightarrow{A} : \nabla \vec{B} = A_{ij}\frac{\partial B_i}{\partial j}$, where the summation convention is used over repeated indexes.

$$\int d^3v f_s(\vec{r}, \vec{v}, t) = n_s \tag{A.14}$$

$$\int d^3v \ \vec{v} f_s(\vec{r}, \vec{v}, t) = n_s \vec{U}_s \tag{A.15}$$

we obtain:

$$\frac{\partial n_s}{\partial t} + \nabla \cdot (n_s \vec{U}_s) = 0 \tag{A.16}$$

which is nothing more than the continuity equation. Going further, we can calculate the first-order moment:

$$\int d^3v \ \vec{v} \frac{\partial f}{\partial t} + \int d^3v \ \vec{v}\vec{v} \cdot \frac{\partial f}{\partial \vec{r}} + \int d^3v \ \vec{v} \frac{\vec{F}}{m} \cdot \frac{\partial f}{\partial \vec{v}} = 0 \tag{A.17}$$

Following the same procedure as before, recalling now that the stress tensor in the lab frame is:

$$\int d^3v \ \vec{v}\vec{v} f_s(\vec{r}, \vec{v}, t) = \overset{\leftrightarrow}{P}_s \tag{A.18}$$

the momentum equation is obtained:

$$\frac{d(m_s n_s \vec{U}_s)}{dt} = n_s \vec{F} - m_s \nabla \ \overset{\leftrightarrow}{P}_s \tag{A.19}$$

with $d/dt = \partial/\partial t + \vec{U}_s \cdot \nabla$ the usual advective derivative.

Now for the second order moment, we should multiply Vlasov equation by the tensor quantity $\vec{v}\vec{v}$. Fortunately, the relation 3.1 need only the trace of the second moment equation to be calculated. This way, multiplying by $\frac{m_s}{2}\mathrm{Tr}(\vec{v}\vec{v}) = m_s v^2/2$ and integrating:

$$\int d^3v \frac{m_s v^2}{2} \frac{\partial f_s}{\partial t} + \int d^3v \frac{m_s v^2}{2} \vec{v} \cdot \frac{\partial f_s}{\partial \vec{r}} + \int d^3v \frac{m_s v^2}{2} \frac{\vec{F}}{m_s} \cdot \frac{\partial f_s}{\partial \vec{v}} = 0 \tag{A.20}$$

Let's calculate each term separately:

$$\begin{aligned} \int d^3v \frac{m_s v^2}{2} \frac{df_s}{dt} &= \frac{d}{dt} \int d^3v \frac{m_s v^2}{2} f_s \\ &= \frac{dW_s}{dt} \end{aligned} \tag{A.21}$$

with W_s the energy density of the plasma. Now the next one,

$$\begin{aligned} \int d^3v \frac{m_s v^2}{2} \vec{v} \cdot \frac{\partial f_s}{\partial \vec{r}} &= \frac{m}{2} \int d^3v v^2 v_j \frac{\partial f_s}{\partial r_j} \\ &= \frac{\partial}{\partial r_j} \int d^3v v_j \frac{m_s v^2}{2} f_s \\ &= \frac{\partial}{\partial r_j} Q_j = \nabla \cdot \vec{Q}_s \end{aligned} \tag{A.22}$$

With Q_s the energy flux density. Finally,

$$\begin{aligned} \int d^3v \frac{m_s v^2}{2} \frac{\vec{F}}{m_s} \cdot \frac{\partial f_s}{\partial \vec{v}} &= \frac{1}{2} \int d^3v \; v^2 F_j \frac{\partial f_s}{\partial v_j} \\ &= \frac{1}{2} \int d^3v \; v^2 \frac{\partial}{\partial v_j} F_j f_s \\ &= \frac{1}{2} \int d^3v \frac{\partial}{\partial v_j} \left(v^2 F_j f_s\right) - \frac{1}{2} \int d^3v F_j f_s \frac{\partial}{\partial v_j} \left(v^2\right) \\ &= -\frac{1}{2} \int d^3v F_j f_s \frac{\partial}{\partial v_j} \left(v^2\right) \\ &= -F_j \int d^3v f_s v_j \\ &= -F_j n_s U_j \\ &= -\vec{F} \cdot n_s \vec{U}_s \\ &= -\vec{J}_s \cdot \vec{F} \end{aligned} \tag{A.23}$$

Where in the third step we integrated by parts and in the fifth step it was assumed that $\vec{F}$ does not depends on the velocity. Joining all terms we can write:

$$\frac{\partial W_s}{\partial t} + \nabla \cdot \vec{Q}_s - \vec{F} \cdot \vec{J}_s = 0 \tag{A.24}$$

Which is the energy equation in an arbitrary reference frame. What we're interesting to analyse, however, is the energy of the plasma itself, so we can identify the agents of heating. Therefore, we have to express eq. A.24 in the frame of reference moving with the bulk velocity $\vec{U}_s$. Let's focus again in each term individually:

$$\begin{aligned} W_s = \frac{m_s}{2} \int d^3v f_s v^2 &= \frac{m_s}{2} \int d^3u (\vec{U}_s + \vec{u})(\vec{U}_s + \vec{u}) f_s \\ &= \frac{m_s}{2} \int d^3u (U_s^2 + u^2 + 2\vec{U}_s \cdot \vec{u}) f_s \\ &= \frac{n_s m_s U_s^2}{2} + \frac{m_s}{2} \int d^3u f_s u^2 + m_s \vec{U}_s \cdot \int d^3u f_s \vec{u} \end{aligned} \tag{A.25}$$

Note that the third integral in the last step gives the macroscopic average velocity of the plasma, but in this case it gives the average velocity in the reference frame moving with the average velocity, therefore this term is zero. The second integral corresponds to the trace of the stress tensor, from which we define $p_s \equiv \frac{1}{3}\mathrm{Tr}(\overleftrightarrow{P}_s)$:

$$W_s = \frac{n_s m_s U_s^2}{2} + \frac{1}{2}\mathrm{Tr}(\overleftrightarrow{P}_s) = \frac{n_s m_s U_s^2}{2} + \frac{3}{2} p_s \tag{A.26}$$

Now the second term of eq. A.24:

$$
\begin{aligned}
\vec{Q}_s &= \int d^3v \frac{m_s}{2} v^2 \vec{v} f_s \\
&= \int d^3u \frac{m_s}{2} (\vec{u} + \vec{U}_s)^2 (\vec{u} + \vec{U}_s) f_s \\
&= \int d^3u \frac{m_s}{2} (u^2\vec{u} + U_s^2\vec{u} + 2(\vec{u}\cdot\vec{U}_s)\vec{u} + u^2\vec{U}_s + U_s^2\vec{U}_s + 2(\vec{u}\cdot\vec{U}_s)\vec{U}_s) f_s \\
&= \vec{q_s} + \frac{m_s U_s^2}{2} \int d^3u f_s \vec{u} + m_s \int d^3u (\vec{u}\cdot\vec{U}_s)\vec{u} f_s + \frac{m\vec{U}_s}{2} \int d^3u f_s u^2 + \\
&+ \frac{m_s U_s^2}{2} \vec{U}_s \int d^3u f_s + m_s \vec{U}_s \vec{U}_s \cdot \int d^3u \vec{u} f_s \\
&= \vec{q_s} + m_s \int d^3u (\vec{u}\cdot\vec{U}_s)\vec{u} f_s + \frac{m_s\vec{U}_s}{2} \int d^3u f_s u^2 + \frac{m_s U_s^2}{2}\vec{U}_s \int d^3u f_s \\
&= \vec{q_s} + m_s \vec{U}_s \cdot \int d^3u \vec{u}\vec{u} f_s + \frac{m_s\vec{U}_s}{2} \int d^3u f_s u^2 + \frac{m_s n_s U_s^2}{2}\vec{U}_s \\
&= \vec{q_s} + \overleftrightarrow{P}_s \cdot \vec{U}_s + \frac{\vec{U}_s}{2}\mathrm{Tr}(\overleftrightarrow{P}_s) + \frac{m_s n_s U_s^2}{2}\vec{U}_s \\
&= \vec{q_s} + \overleftrightarrow{P}_s \cdot \vec{U}_s + \frac{3}{2} p_s \vec{U}_s + \frac{m_s n_s}{2} U_s^2 \vec{U}_s
\end{aligned} \tag{A.27}
$$

And the divergence of this vector:

$$
\nabla \cdot \vec{Q}_s = \nabla \cdot \vec{q_s} + \nabla \cdot (\overleftrightarrow{P}_s \cdot \vec{U}_s) + \frac{3}{2} \nabla \cdot (p_s \vec{U}_s) + \frac{m_s}{2} \nabla \cdot (n_s U_s^2 \vec{U}_s) \tag{A.28}
$$

where,

$$
\begin{aligned}
\nabla \cdot (\overleftrightarrow{P}_s \cdot \vec{U}_s) &= \frac{\partial}{\partial x_i} (P_{s,ij} U_{s,j}) \\
&= U_{s,j} \frac{\partial P_{s,ij}}{\partial x_i} + P_{s,ij} \frac{\partial U_{s,j}}{\partial x_i} \\
&= (\nabla \cdot \overleftrightarrow{P}_s) \cdot \vec{U}_s + \overleftrightarrow{P}_s \colon \nabla \cdot \vec{U}_s
\end{aligned} \tag{A.29}
$$

$$
\frac{m_s}{2} \nabla \cdot (n_s U_s^2 \vec{U}_s) = \frac{m_s}{2} U_s^2 \nabla \cdot (n_s \vec{U}_s) + \frac{m_s}{2} n_s \vec{U}_s \nabla (U_s^2) \tag{A.30}
$$

$$
\frac{3}{2} \nabla \cdot (p_s \vec{U}_s) = \frac{3}{2} \vec{U}_s \cdot \nabla p_s + \frac{3}{2} p_s \nabla \cdot \vec{U}_s \tag{A.31}
$$

Finally, the energy equation can be written:

$$\frac{\partial}{\partial t}\left(\frac{1}{2}n_s m_s \vec{U}_s + \frac{3}{2}p_s\right) + \nabla\cdot\vec{q}_s + (\nabla\cdot \overset{\leftrightarrow}{P}_s)\cdot\vec{U}_s + \overset{\leftrightarrow}{P}_s\colon \nabla\cdot\vec{U}_s + \frac{m_s}{2}U_s^2\nabla\cdot(n_s\vec{U}_s)$$
$$+\frac{m_s}{2}n_s\vec{U}_s\nabla(U_s^2) + \frac{3}{2}\vec{U}_s\cdot\nabla p_s + \frac{3}{2}p_s\nabla\cdot\vec{U}_s - \vec{F}\cdot\vec{J}_s = 0 \tag{A.32}$$

We can simplify a little bit the previous equation if we sum the momentum equation multiplied by $m_s\vec{U}_s$:

$$m_s n_s \frac{d\vec{U}_s}{dt}\cdot\vec{U}_s + \vec{J}_s\cdot\vec{F} - \nabla\overset{\leftrightarrow}{P}_s\cdot\vec{U}_s = 0 \tag{A.33}$$

Summing eq. A.32 and eq. A.33 and doing the algebra we obtain:

$$\frac{d}{dt}\left(\frac{3}{2}p_s\right) + \frac{3}{2}p_s(\nabla\cdot\vec{U}_s) + \nabla\cdot\vec{q}_s + \overset{\leftrightarrow}{P}_s\colon\nabla\vec{U}_s = 0 \tag{A.34}$$

As a last step, separating the stress tensor in its trace and traceless components: $\overset{\leftrightarrow}{P}_s = p_s\overset{\leftrightarrow}{\mathbb{I}} + \overset{\leftrightarrow}{\sigma}_s$ we have that:

$$\begin{aligned}\overset{\leftrightarrow}{P}_s\colon\nabla\vec{U}_s = P_{s,ij}\frac{\partial U_{s,i}}{\partial x_j} &= (\delta_{ij}p_s + \sigma_{ij})\frac{\partial U_{s,i}}{\partial x_j}\\ &= p_s\frac{\partial U_{s,j}}{\partial x_j} + \sigma_{ij}\frac{\partial U_{s,i}}{x_j}\\ &= p_s\nabla\cdot\vec{U}_s + \overset{\leftrightarrow}{\sigma}_s\colon\nabla\vec{U}_s\end{aligned} \tag{A.35}$$

Finally, we can write

$$\frac{d}{dt}\left(\frac{3}{2}p_s\right) + \frac{5}{2}p_s\nabla\cdot\vec{U}_s + \nabla\cdot\vec{q}_s + \overset{\leftrightarrow}{\sigma}_s\colon\nabla\vec{U}_s = 0 \tag{A.36}$$

Where the quantity $\overset{\leftrightarrow}{\sigma}_s\colon\nabla\vec{U}_s$ finally appears. Note that this term contributes to the energy only if the stress tensor is anisotropic. Sometimes $\overset{\leftrightarrow}{\sigma}_s$ is called the viscous stress tensor, this way pressure anisotropies can act as an effective viscosity macroscopically.

In the case of study of this thesis, we have a collisionless, magnetized plasma subject to a shear motion of the form $\vec{U} = -sx\hat{y}$. Additionally, if the cyclotron frequency of the ions is much larger than the rate at which energy is injected through this shear motion, which is our case[3], the plasma can be considered gyrotropic, i.e., it is isotropic in any direction perpendicular to the direction of the mean magnetic field. We can then separate the pressures into a pressure $p_\perp$ perpendicular to the mean magnetic field, and another one parallel to the mean magnetic field, $p_\parallel$. The geometric configuration considered is depicted in fig. A.1, where we have the frame of reference of the laboratory (unprimed) and the frame of reference moving along with the mean magnetic field (primed). In this case, the term $\overleftrightarrow{\sigma}_s \colon \nabla\vec{U}_s = \sigma_{ij}\frac{\partial U_{s,j}}{\partial x_j} = \sigma_{xy}\frac{\partial U_y}{\partial x}$.

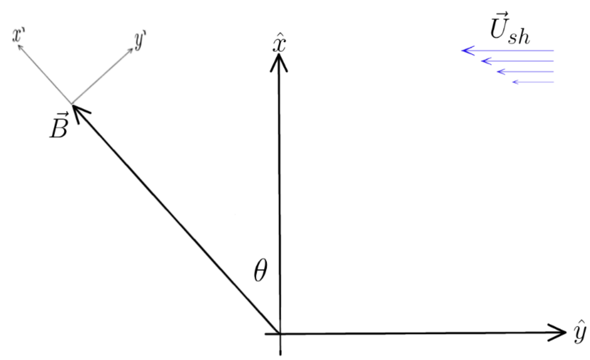

Figure A.1: Geometrical configuration of the plasma in our simulations.

Let's calculate the term P_{xy} then:

[3]Recall that in our simulations $\omega_{c,i}/s \sim 10^3$ with s the shear frequency.

$$
\begin{aligned}
P_{xy} = m_s \int d^3v f_x v_x v_y = m_s \int d^3v f_s (v_{x'} \cos\theta - v_{y'} \sin\theta)(v_{x'} \sin\theta + v_{y'} \cos\theta) \\
&= m_s \cos\theta \sin\theta \left(\int d^3v f_s v_{x'} v_{x'} - \int d^3v f_s v_{y'} v_{y'} \right) \\
&+ m_s \int d^3v f_s v_{x'} v_{y'} (\cos^2\theta - \sin^2\theta) \\
&= \cos\theta \sin\theta (p_{x'} - p_{y'}) + \cos 2\theta \int d^3v m_s v_{x'} y_{y'} \\
&= \cos\theta \sin\theta (p_\perp - p_\|) + \cos 2\theta P_{x'y'} \\
&= \cos\theta \sin\theta (p_\perp - p_\|)
\end{aligned}
\tag{A.37}
$$

Where in the last step $P_{x'y'} = 0$ since, as in the primed frame of reference the system is gyrotropic, the stress tensor is diagonal. Defining the unit vector along the magnetic field $\hat{b} \equiv \vec{B}/B$, in our case we have $\hat{b} = \hat{y}' = -\hat{x}\sin\theta + \hat{y}\cos\theta \equiv \hat{b}_x + \hat{b}_y$. Therefore, we have

$$
\begin{aligned}
\overleftrightarrow{\sigma}_s \colon \nabla \vec{U}_s = \sigma_{xy} \frac{\partial U_x}{\partial y} \hat{x}\hat{y} &= \sin\theta\cos\theta \hat{x}\hat{y} (p_\perp - p_\|) \frac{\partial}{\partial y}(-sy) \\
&= -\hat{b}_x \hat{b}_y (p_\perp - p_\|) \cdot -s \\
&= s(p_\perp - p_\|) \hat{b}_x \hat{b}_y
\end{aligned}
\tag{A.38}
$$

This way, the system has an energy contribution from the pressure anisotropy of the form $\overleftrightarrow{\sigma}_s \colon \nabla \vec{U}_s = s(p_\perp - p_\|)\hat{b}_x \hat{b}_y$, with $s = \frac{1}{B}\frac{dB}{dt}$. Recall that, as in our configuration the mean magnetic field is being amplified by the shear, the anisotropy produced is such that $p_\perp > p_\|$, so the energy contribution from the viscous stress tensor is positive, therefore it heats the plasma.

Appendix B

1D Shear Simulations

It is of interest to understand the assumptions and procedures behind the implementation of the simulations we've run in 1D. In particular, in this section it will be described the coordinate change used to pass from 2D to 1D. For this we will make use of the description of the 2D shear coordinates in the Appendix of [79]. We will call S' the frame of reference used in the 2D simulations and S'' the frame of reference used in 1D simulations. The transformations relating the usual cartesian coordinates and S' are, as stated in [79]:

$$
\begin{aligned}
x' &= x, & y' &= \Gamma(y - vt), \\
z' &= z, & t' &= \Gamma(t - vy/c^2),
\end{aligned}
\tag{B.1}
$$

Where $\Gamma = (1 - v^2/c^2)^{-1/2}$. From these transformations, S'' is given by:

$$
\begin{aligned}
x'' &= x' - \frac{y'st'}{1 + s^2t'^2}, & y'' &= y' \\
z'' &= z', & t'' &= t'
\end{aligned}
\tag{B.2}
$$

Let's derive the relevant equations in S''. In our plasma subject to the shear velocity $\vec{U} = -sx\hat{y}$, initially the mean magnetic field is given by $\langle\vec{B}\rangle = B_0\hat{x}$ and, as seen in section A.2, from flux conservation we have that at later times $\langle\vec{B}\rangle(t) = B_0(\hat{x} - st\hat{y})$. With this and eqs. B.1 and B.2 we can calculate the gradient operator in the Lab (non-shearing) frame in terms of the coordinates of S'', $\nabla = \hat{x}\partial/\partial x + \hat{y}\partial/\partial y$. In addition, as the shear frequency s is expected to be much smaller than the ion gyro-frequency $\omega_{c,i}$, we expect $\vec{U}$ to be nonrelativistic, so that we can set $\Gamma \sim 1$ in eqs. B.1 and in particular $t = t' = t''$. The gradient can be written then as:

$$\begin{aligned}
\frac{\partial}{\partial x} &= \frac{\partial x''}{\partial x}\frac{\partial}{\partial x''} + \frac{\partial y''}{\partial x}\frac{\partial}{\partial y''} \\
\frac{\partial}{\partial x} &= \frac{1}{1+s^2t^2}\frac{\partial}{\partial x''} + st\frac{\partial}{\partial y''} \\
\frac{\partial}{\partial y} &= \frac{\partial y}{\partial x''}\frac{\partial}{\partial x''} + \frac{\partial y''}{\partial y}\frac{\partial}{\partial y''} \\
\frac{\partial}{\partial y} &= -\frac{st}{1+s^2t^2}\frac{\partial}{\partial x''} + \frac{\partial}{\partial y''}
\end{aligned} \tag{B.3}$$

It can be shown that in this frame of reference, by solving the problem in 1D so that $\frac{\partial}{\partial y''} = 0$ and $\frac{\partial}{\partial z''} = 0$, the gradient operator is parallel to $\langle\vec{B}\rangle$. This is desirable as this allows us to set $\vec{k} \parallel \langle\vec{B}\rangle$, so the wavevector of the relevant modes can be resolved in 1D, being this dimension the one that follows the direction of the mean magnetic field at any given time.

Let solve the 1D problem in this frame of reference then. In order to consider only 1 dimension we focus on an arbitrarily narrow and long stripe of plasma confined to the region $0 < y'' < \delta$, with $\delta \to 0$[1] (See fig.)

Now we show the modification Maxwell's equations suffer when going to the S'' frame. Let's calculate first the coordinate derivatives of S' in terms of the coordinates of S'':

[1]Note, however, that making $\delta \to 0$ implies that $x'' = x'$ in eqs. B.2, but the transformation is nevertheless necessary for eqs. B.3 to imply $\vec{k} \parallel \langle\vec{B}\rangle$.

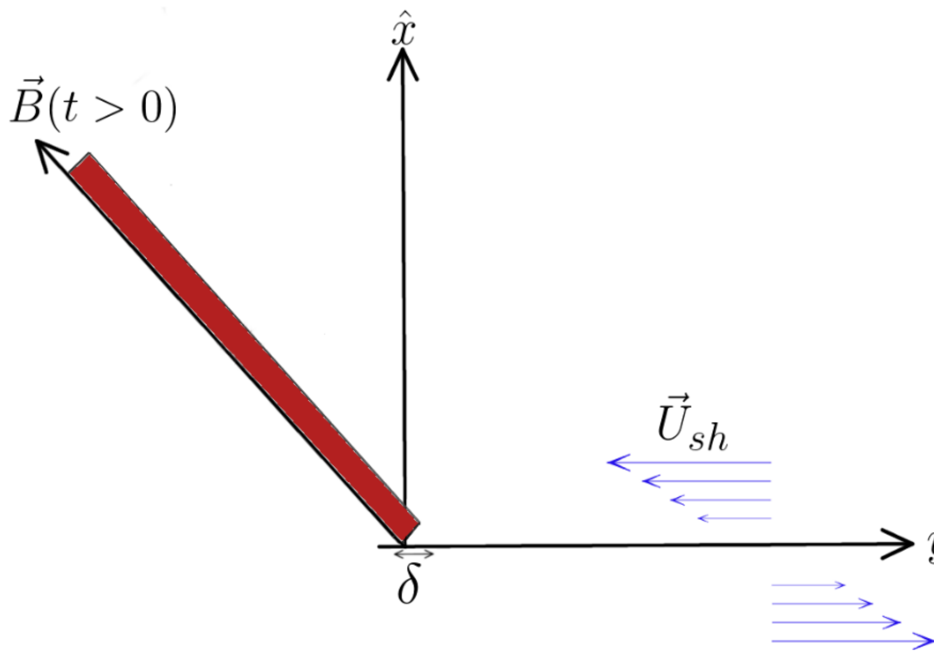

Figure B.1: Depiction of the orientation of the system at a given time $t > 0$. The red shaded region represents the narrow stripe of plasma considered in the 1D problem.

$$\begin{aligned}
\frac{\partial}{\partial t'} &= \frac{\partial}{\partial t''} - sy'' \frac{1 - s^2 t''^2}{(1 + s^2 t^2)^2} \frac{\partial}{\partial x''} \\
\frac{\partial}{\partial x'} &= \frac{\partial}{\partial x''} \\
\frac{\partial}{\partial y'} &= \frac{\partial}{\partial y''} - \frac{st''}{1 + st''^2} \frac{\partial}{\partial x''} \\
\frac{\partial}{\partial z'} &= \frac{\partial}{\partial z''}
\end{aligned} \tag{B.4}$$

This will make easier the modification of Maxwell's equations written in the frame S of the Appendix of [79]. Now we will write Ampère's Law and Faraday's Law in the S'' frame and then impose the 1D condition to them.

According to equation A.26 of [79], the Ampère's Law in the S' frame can be written:

$$\frac{\partial \vec{E}'}{\partial t'} = c\nabla' \times \vec{B}' - 4\pi \vec{J}' - sE'_x\hat{y} - s\left(ct'\frac{\partial \vec{B}'}{\partial y'} + \frac{y'}{c}\frac{\partial \vec{B}'}{\partial t'}\right) \times \hat{x} \tag{B.5}$$

Expressed by components in the S'' frame:

$$\frac{\partial E'_x}{\partial t''} = c\left(\frac{\partial B'_z}{\partial y''} - \frac{st''}{1+s^2t''^2}\frac{\partial B'_z}{\partial x''} - \frac{\partial B'_y}{\partial z''}\right) - 4\pi J'_x \tag{B.6}$$

$$\begin{aligned}\frac{\partial E'_y}{\partial t''} = & -c\frac{1}{1+s^2t''^2}\frac{\partial B'_z}{\partial x''} + c\frac{\partial B'_x}{\partial z''} - sE'_x - sct''\frac{\partial B'_z}{\partial y''} - \\ & - \frac{sy''}{c}\left(\frac{\partial B'_z}{\partial t''} - \frac{sy''(1-s^2t''^2)}{1+s^2t''^2}\frac{\partial B'_z}{\partial x''}\right) - 4\pi J'_y\end{aligned} \tag{B.7}$$

$$\begin{aligned}\frac{\partial E'_z}{\partial t''} = & c\left(\frac{1}{1+s^2t''^2}\frac{\partial B'_y}{\partial x''} + \frac{st''}{1+s^2t''^2}\frac{\partial B'_x}{\partial x''} - \frac{\partial B'_x}{\partial y''}\right) + \\ & + cst''\frac{\partial B'_y}{\partial y''} + \frac{sy''}{c}\left(\frac{\partial B'_y}{\partial t''} - \frac{sy''(1-s^2t''^2)}{1+s^2t''^2}\frac{\partial B'_y}{\partial x''}\right) - 4\pi J'_z\end{aligned} \tag{B.8}$$

And the Faraday's Law, in the frame S', according to eq. A.14 of [79]:

$$\frac{\partial \vec{B}'}{\partial t'} = -c\nabla \times \vec{E}' - sB'_x\hat{y} + s\left(ct'\frac{\partial \vec{E}'}{\partial y'} + \frac{y'}{c}\frac{\partial \vec{E}'}{\partial t'}\right) \times \hat{x} \tag{B.9}$$

And expressed in the S'' frame:

$$\frac{\partial B'_x}{\partial t''} = -c\left(\frac{\partial E'_z}{\partial y''} - \frac{st''}{1+s^2t''^2}\frac{\partial E'_z}{\partial x''} - \frac{\partial E'_y}{\partial z''}\right) \tag{B.10}$$

$$\begin{aligned}\frac{\partial B'_y}{\partial t''} = & c\frac{1}{1+s^2t''^2}\frac{\partial E'_z}{\partial x''} - c\frac{\partial E'_x}{\partial z''} - sB'_x + sct''\frac{\partial E'_z}{\partial y''} \\ & + \frac{sy''}{c}\left(\frac{\partial E'_z}{\partial t''} - \frac{sy''(1-s^2t''^2)}{1+s^2t''^2}\frac{\partial E'_z}{\partial x''}\right)\end{aligned} \tag{B.11}$$

$$\begin{aligned}\frac{\partial B'_z}{\partial t''} = & -c\left(\frac{1}{1+st''^2}\frac{\partial E'_y}{\partial x''} + \frac{st''}{1+s^2t''^2}\frac{\partial E'_x}{\partial x''} - \frac{\partial E'_x}{\partial y''}\right) \\ & - cst''\frac{\partial E'_y}{\partial y''} - \frac{sy''}{c}\left(\frac{\partial E'_y}{\partial t''} - \frac{sy''(1-s^2t''^2)}{1+s^2t''^2}\frac{\partial E'_y}{\partial x''}\right)\end{aligned} \tag{B.12}$$

Appendix C

Acceleration Mechanisms Derivations

In this section the derivation and calculations of the different results of the acceleration mechanisms stated in the Introduction are shown.

C.1 Second-Order Fermi Acceleration

Following the historical line of thought, the original idea of Fermi will be presented, namely, how a particle can gain energy through successive stochastic encounters with "magnetic clouds". The order of the ideas will closely follow the derivation by Vietri [81].

Consider a particle moving with energy E and 3-momentum $\underset{\sim}{p}$ in the laboratory frame and a magnetic cloud moving with velocity $-V$ along the x axis in the lab frame. Let θ be the angle the direction of motion of the particle makes with the velocity of the cloud in the lab frame. We will assume that the rest mass of the cloud is much larger than the rest mass of the particle, therefore the center of momentum reference frame will be the frame of the cloud.

Given these conditions, in the reference frame of the cloud it is fulfilled that the

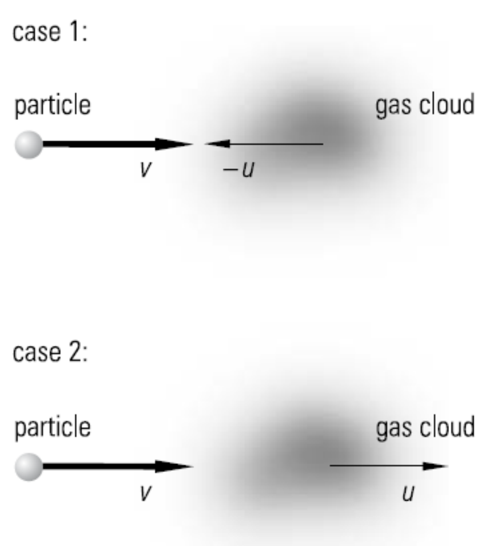

Figure C.1: A schematic picture of the collision of a charged particle and a magnetic cloud seen in the Lab frame. In the first case, a head-on collision is depicted, while in the second case a tail collision is showed. Figure taken from Grupen, 2005[82]

energy of the particle is conserved, and the x component of $\underset{\sim}{p}$, p_x, is reversed in direction (elastic collision). In this section units in which $c = 1$ will be used.

Denoting the quantities in the cloud frame with a bar over them, we can write the energy of the particle before the collision in the reference frame of the cloud, $\overline{E} = -\vec{p} \cdot \vec{U}$, with $\vec{U}$ the 4-velocity of the cloud,

$$\begin{aligned} \overline{E} &= -(E, \underset{\sim}{p}) \cdot (\gamma_V, \gamma_V \underset{\sim}{V}) = \gamma_V E - \gamma_V \underset{\sim}{p} \cdot \underset{\sim}{V} = \gamma_V (E + pV \cos\theta) \\ &= \gamma_V (E + p_x V), \end{aligned} \tag{C.1}$$

with $\gamma_V = \frac{1}{\sqrt{1-V^2}}$ and $p_x = p\cos\theta$ the x-component of the 3-momentum of the particle. In a similar fashion, we can write the energy of the particle in the lab frame as:

$$\begin{aligned} E &= \gamma_V(\overline{E} - \overline{p}V\cos\phi) \\ &= \gamma_V(\overline{E} - \overline{p}_x V), \end{aligned} \tag{C.2}$$

with $\overline{p}_x$ the x-component of the 3-momentum of the particle in the cloud frame before the collision. This quantity can be written as,

$$\overline{p}_x = \gamma_V(p_x + VE) = \gamma_V(p\cos\theta + VE) \tag{C.3}$$

Now, after the encounter, as we have assumed an elastic collision, we have, in the frame of reference of the cloud,

$$\overline{E}_{\text{after}} = \overline{E} \tag{C.4}$$

$$\overline{p}_{x,\text{after}} = -\overline{p}_x \tag{C.5}$$

So writing now the energy after the encounter in the lab frame,

$$\begin{aligned} E_{\text{after}} &= \gamma_V(\overline{E}_{\text{after}} - \overline{p}_{x,\text{after}}V) \\ &= \gamma_V(\overline{E} + \overline{p}_x V) \\ &= \gamma_V(\gamma_V(E + p_x V) + \gamma_V(p_x + VE)V) \\ &= \gamma_V^2 E\left[1 + \frac{2p_x V}{E} + V^2\right] \\ &= \gamma_V^2 E\left[1 + \frac{2pV\cos\theta}{E} + V^2\right] \end{aligned} \tag{C.6}$$

Where in the second step we used eqs.C.4 and C.5. Noting that $p/E = v$, the velocity of the particle in the lab frame,

$$E_{\text{after}} = \gamma_V^2 E\left[1 + 2vV\cos\theta + V^2\right] \tag{C.7}$$

Considering that $V \ll 1$, we can expand this expression keeping terms up to V^2,

$$E_{\text{after}} \cong E(1+V^2)\left[1+2vV\cos\theta+V^2\right] \tag{C.8}$$
$$\cong E(1+2vV\cos\theta+2V^2) \tag{C.9}$$

So the energy gain $\Delta E = E_{\text{after}} - E$:

$$\frac{\Delta E}{E} = 2vV\cos\theta + 2V^2 \tag{C.10}$$

Now, as the collisions are essentially stochastic, it is expected that the clouds velocities are distributed randomly, so we have to average over all possible angles,

$$\left\langle \frac{\Delta E}{E} \right\rangle = \int \frac{\Delta E}{E} P(\cos\theta) d\cos\theta$$

With $P(\cos\theta)d\cos\theta$ the probability distribution of having a collision at an angle θ. This probability is not uniform, however. There's a slightly greater probability to have a head-on collision than a tail one. One can convince oneself of this if we assume that the mean free path of the clouds, call it l_{mfp}, remains constant and independent of energy, then the time between collisions can be expressed:

$$\tau = \frac{l_{\text{mfp}}}{V_{\text{rel}}} \tag{C.11}$$

with V_{rel} is the relative velocity between the particle and the cloud in the direction of the particle's velocity,

$$V_{\text{rel}} = \frac{v + V\cos\theta}{1 + vV\cos\theta} \tag{C.12}$$

Taking $v \to 1$, just for simplicity, then it can be seen that the time of head-on collisions is shorter than the time of tail collisions:

$$\tau_{\text{head-on}} = \frac{l_{\text{mfp}}}{1+V} \tag{C.13}$$

$$\tau_{\text{tail}} = \frac{l_{\text{mfp}}}{1-V} \tag{C.14}$$

So head-on collisions are more frequent than tail ones, therefore head-on encounters have a larger probability. This probability is then proportional to the relative velocity[1],

$$P(\cos\theta)d\cos\theta = CV_{\text{rel}} \tag{C.15}$$

To calculate the proper normalization, we simply impose $\int_{-1}^{1} P(\cos\theta)d\cos\theta = 1$, giving $C = 1/2$,

$$P(\cos\theta)d\cos\theta = \frac{1}{2}V_{\text{rel}} = \frac{1}{2}(1 + V\cos\theta)d\cos\theta \tag{C.16}$$

Then averaging over angles,

$$\left\langle \frac{\Delta E}{E} \right\rangle = \frac{1}{2}\int_{-1}^{1} \frac{\Delta E}{E}(1 + V\cos\theta)d\cos\theta \tag{C.17}$$

$$= \frac{1}{2}\int_{-1}^{1}(2vV\cos\theta + 2V^2)(1 + V\cos\theta)d\cos\theta \tag{C.18}$$

$$= \frac{8}{3}V^2 \tag{C.19}$$

Then we obtain the well-known result,

$$\left\langle \frac{\Delta E}{E} \right\rangle = \frac{8}{3}V^2 \tag{C.20}$$

[1]One here assumes that the particles are isotropically distributed with respect to the cloud, so for a given time interval, the collision rate will depend solely on the relative velocity between the particle and the cloud[83].

Therefore, on average, the particles gain energy at a rate that is second-order in V.

From the dependence given in eq. C.20 it can be shown that, after successive acceleration encounters it can generate a power-law energy distribution. This derivation follows the argument by Grupen [82]. Let's start with eq. C.20 written as:

$$\Delta E = \varepsilon E \tag{C.21}$$

Where $\varepsilon = 8V^2/3$. Let's call E_0 the initial energy of the particle, and so on. Therefore, we can write

$$E_1 = E_0 + \varepsilon E_0 = E_0(1+\varepsilon) \tag{C.22}$$

$$\vdots \tag{C.23}$$

$$E_n = E_0(1+\varepsilon)^n \tag{C.24}$$

With n the number of encounters,

$$n = \frac{\ln(E_n/E_0)}{\ln(1+\varepsilon)} \tag{C.25}$$

Now, there's a finite probability that the particle escapes from the accelerator after an encounter, let's call it P and let's assume it is constant[2]. Then, after one encounter, the probability that the particle hasn't escaped is simply $1-P$, and the number of particles after the first encounter is then $N_1 = N_0(1-P)$, with N_0 the initial number of particles. After the second encounter, then, the number of particles will be $N_2 = N_1(1-P) = N_0(1-P)^2$, and so on, so after n encounters,

[2] In reality, this probability is energy dependent and the higher the energy, the more probable is that the particle escapes. This fact determines the maximum achievable energy in a specific system

$$N_n = N_0(1-P)^n \tag{C.26}$$

This corresponds to the number of particles with energies E_n. Therefore, the number of particles with energies E_n or larger is:

$$\begin{aligned}
N(\geq E_n) &= N(E_n) + N(E_{n+1}) + \ldots + N(E_\infty) && \text{(C.27)}\\
&= N_0 \sum_{m=n}^{\infty} (1-P)^m && \text{(C.28)}\\
&= N_0(1-P)^n \sum_{m=n}^{\infty} (1-P)^{m-n} && \text{(C.29)}\\
&= N_0(1-P)^n \sum_{m=0}^{\infty} (1-P)^m && \text{(C.30)}\\
N(\geq E_n) &= N_0 \frac{(1-P)^n}{P} && \text{(C.31)}
\end{aligned}$$

replacing eq. C.25 in eq. C.31,

$$\begin{aligned}
N(\geq E_n) &= N_0 \frac{1}{P} \left[\left(\frac{E}{E_0} \right)^{\ln(1-P)} \right]^{\frac{1}{\ln(1+\varepsilon)}} && \text{(C.32)}\\
&= N_0 \frac{1}{P} \left[\frac{E}{E_0} \right]^{\frac{\ln(1-P)}{\ln(1+\varepsilon)}} && \text{(C.33)}\\
N(\geq E_n) &= N_0 \frac{1}{P} \left[\frac{E}{E_0} \right]^{-\gamma} && \text{(C.34)}\\
N(\geq E_n) &\propto E^{-\gamma} && \text{(C.35)}
\end{aligned}$$

defining $\gamma = \frac{\ln(1/(1-P))}{1+\varepsilon}$. So we have recovered a power-law energy distribution for a system that undergoes successive acceleration where the energy gain is proportional to the current energy.

C.2 First-Order Fermi Mechanism

In what follows, a derivation of the energy gain and the predicted spectral index of DSA is sketched. The derivation will closely follow the one by Longair [84] and Vietri [81].

Consider a strong shock propagating through a diffuse medium, as the shock wave of a SNR propagating through the ISM. Let's consider a population of high energy particles to be present in the front and behind the shock front. We will assume that the high energy particles are propagating at a speed much larger than the speed of the shock. Usually, the shock front is very thin, its thickness is much smaller than the gyroradius of the particles so they won't notice it at all. Nevertheless, when the particles cross the shock in either direction, they are scattered by the turbulent motion present on both sides of the shock. This produces an isotropization of the velocity distribution in the frame of reference at rest with respect to the shock. A schematic picture is sketched in figure C.2.

Let's stay in the frame of reference comoving with the shock. In this case, we see the upstream moving with velocity U_1 and the downstream moving with velocity U_2 as depicted in figure C.2. From conservation laws for mass, momentum, and energy, let's find stationary solutions. Since the motion is 1D, we can write:

$$\frac{\partial}{\partial x}(\rho u) = 0 \tag{C.36}$$

$$\frac{\partial}{\partial x}(\rho u^2 + P) = 0 \tag{C.37}$$

$$\frac{\partial}{\partial x}\left[\rho u\left(\frac{1}{2}u^2 + w\right)\right] = 0 \tag{C.38}$$

With ρ the density of the fluid, u the velocity along the direction of motion, P the pressure of the fluid and w the enthalpy per unit mass. Considering an ideal gas, we can write the enthalpy as

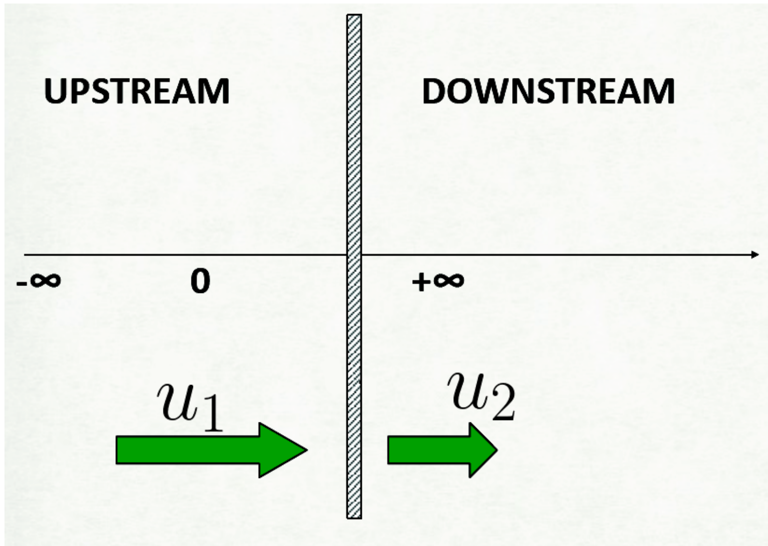

Figure C.2: A shock front propagating through a medium as seen in the reference frame of the shock; as the shock front is moving to the left, the upstream is seen with velocity u_1 and the upstream with velocity u_2. Credit: P. Blasi; `http://www.astro.iag.usp.br/~highenastro/Talks/Lecture_VI_Pasquale_Blasi_1.pdf`

$$w = \frac{\gamma}{\gamma - 1} PV = \frac{\gamma}{\gamma - 1} P\rho^{-1} \tag{C.39}$$

With V the volume per unit mass. Then, the equation for energy balance can be written:

$$\frac{\partial}{\partial x}\left(\frac{1}{2}\rho u^3 + \frac{\gamma}{\gamma - 1} Pu\right) = 0 \tag{C.40}$$

From here we can find the discontinuous solution linking the upstream and the downstream:

$$\rho_1 u_1 = \rho_2 u_2 \tag{C.41}$$
$$\rho_1 u_1^2 + P_1 = \rho_2 u_2^2 + P_2 \tag{C.42}$$
$$\frac{1}{2}\rho_1 u_1^3 + \frac{\gamma}{\gamma-1}P_1 u_1 = \frac{1}{2}\rho_2 u_2^3 + \frac{\gamma}{\gamma-1}P_2 u_2 \tag{C.43}$$

From here we can obtain the following relations:

$$\frac{\rho_2}{\rho_1} = \frac{u_1}{u_2} = \frac{(\gamma+1)M_1^2}{(\gamma-1)M_1^2+2} \tag{C.44}$$
$$\frac{P_2}{P_1} = \frac{2\gamma M_1^2 - (\gamma-1)}{\gamma+1} \tag{C.45}$$
$$\frac{T_2}{T_1} = \frac{[2\gamma M_1^2 - \gamma(\gamma-1)][(\gamma-1)M_1^2+2]}{M_1^2(\gamma+1)^2} \tag{C.46}$$

With $M_1 = u_1/c_{s,1}$ the upstream Mach number, $c_{s,1} = (\gamma P_1/\rho_1)^{1/2}$ the upstream sound speed and T the temperature, obtained from the perfect gas law $P_1V_1/T_1 = P_2V_2/T_2$.

Now for a strong shock, $v_1 \gg c_{s,1}$, so we can write,

$$\frac{\rho_2}{\rho_1} = \frac{u_1}{u_2} = \frac{\gamma+1}{\gamma-1} \tag{C.47}$$
$$\frac{P_2}{P_1} = \frac{2\gamma M_1^2}{\gamma+1} \tag{C.48}$$
$$\frac{T_2}{T_1} = \frac{2\gamma(\gamma-1)}{(\gamma+1)^2}M_1^2 \tag{C.49}$$

Taking $\gamma = 5/3$ for a fully ionized gas, we obtain that $u_2 = \frac{1}{4}u_1$.

Now let's analyze a high energy particle crossing the shock front. The notable feature of considering a shock wave is that a particle will always gain energy when crossing the shock front either from upstream to downstream or the other way around. In the first case, the particle placed in the upstream sees material approaching from the shock with nonrelativistic velocity $u_1 - u_2$ respect to the downstream, in a head-on collision analogous to the galactic cloud moving towards the non-thermal particle. After crossing the shock front, placed in the downstream, the velocity distribution is again isotropized and the particle can now see material approaching the shock front, again with the same velocity $u_1 - u_2$, so in this case the collision is head-on too. In this way, there are only head-on collisions and the particle only gain energy.

Let's calculate the energy gain and obtain that is first order in velocity. Take a relativistic particle with energy $E \sim p$ in the frame comoving with the upstream, then in the downstream frame,

$$E_d = \gamma(E + pV\cos\theta) \tag{C.50}$$

$$= \gamma E(1 + V\cos\theta) \tag{C.51}$$

Now with $V = u_1 - u_2 = -(3/4)u_1$ the velocity of the downstream as seen in the upstream frame and $\gamma = (1 - V^2)^{-1/2}$. In the downstream, the direction of the particle is isotropized and approaches the shock again with the same energy E_d but in general a different angle θ'. Transforming again to the upstream frame,

$$E_u = \gamma E_d(1 - V\cos\theta') \tag{C.52}$$

$$= \gamma^2 E(1 + V\cos\theta)(1 - V\cos\theta') \tag{C.53}$$

Note that the velocity of the upstream as seen in the downstream is now positive. Then the energy gain,

$$\frac{\Delta E}{E} = \gamma^2(V\cos\theta - V\cos\theta' - V^2\cos\theta\cos\theta') \tag{C.54}$$

But with the subtlety that $0 \leq \theta \leq \pi/2$ and $\pi/2 \leq \theta \leq \pi$, as we want the particle to always cross the shock front. To obtain the probability distribution in this case we note that the flux of particles crossing the shock front with an angle θ is $J = nV\cos\theta$, so the probability of a particle crossing the shock front with that angle is:

$$P(\cos\theta)d\cos\theta = \frac{nV\cos\theta}{\int_0^1 nV\cos\theta d\cos\theta} \tag{C.55}$$

$$= 2\cos\theta d\cos\theta \tag{C.56}$$

Applying the proper normalization. Assuming that the shock moves at nonrelativistic velocities $\gamma \sim 1$, and denoting in general $\mu = \cos\theta$ then we can average over the angles:

$$\left\langle \frac{\Delta E}{E} \right\rangle = -\int_0^1 2\mu d\mu \int_{-1}^0 2\mu' d\mu' (V\mu - V\mu' - V^2\mu\mu') \tag{C.57}$$

$$= \frac{2}{3}V + \frac{2}{3}V + \frac{4}{9}V^2 \tag{C.58}$$

$$\approx \frac{4}{3}V \tag{C.59}$$

As we are assuming nonrelativistic velocities, $V^2 \sim 0$. Then in this case, the term first order in velocity doesn't disappear when we average out the angles and now the energy gain is proportional to V.

To obtain the energy spectrum, Bell [4] presented a very elegant argument, which will be here outlined. Consider the flux of particles crossing the shock to the downstream region, J_+, the flux of particles that is sufficiently pitch-angle scattered to re-approach the shock front and cross it again, J_-, and the flux of particles that is advected away from the shock through downstream infinity, J_∞. As we assumed stationary conditions, we must have that:

$$J_+ = J_- + J_\infty \tag{C.60}$$

Then, the probability of the particles to return to the shock and cross it again is simply:

$$P_{\text{return}} = \frac{J_-}{J_+} = \frac{J_-}{J_- + J_\infty} \tag{C.61}$$

To obtain J_- and J_∞, let's recall that the flux of particles that re-enter the shock at an angle θ is $n_0 V \cos\theta$, with n_0 the number density of particles in the downstream region, that remains constant. Then, the average number of particles that cross the shock is given by

$$J_- = \frac{1}{4\pi}\int_0^1 n_0 V \cos\theta d\Omega \tag{C.62}$$

$$= \frac{n}{4} \tag{C.63}$$

Assuming for simplicity that the particles are relativistic. For J_∞, consider that, as the particles are being advected away to the shock area, they are moving away essentially at the fluid velocity, as the particles are tied to the magnetic field lines and these lines, in turn, are frozen in the fluid, so basically $J_\infty = n_0 u_2$. Then the probability reads:

$$P_{\text{return}} = \frac{J_-}{J_- + J_\infty} = \frac{n_0/4}{n_0/4 + n_0 u_2} \tag{C.64}$$

$$= \frac{1}{1 + 4u_2} \tag{C.65}$$

$$\approx 1 - 4u_2 \tag{C.66}$$

Assuming in the last step nonrelativistic fluid velocities. Now replacing this values in eq. C.35 and recalling that

$$\gamma = \frac{\ln(1/(1-P))}{1+\varepsilon} \tag{C.67}$$
$$= \frac{\ln(1/(P_{\text{return}}))}{1+\varepsilon} \tag{C.68}$$

with, in the case of shocks, $\varepsilon = 4V/3$:

$$\ln(1/(1-P)) = -\ln(1-P) \approx P = 1 - P_{\text{return}} = 4u_2 \tag{C.69}$$
$$\ln(1+\varepsilon) = \ln(1+\frac{4}{3}(u_1-u_2)) \approx \frac{4}{3}(u_1-u_2) \tag{C.70}$$

And, recalling that for strong shocks $u_2/u_1 = 1/4$:

$$\gamma = \frac{4u_2}{u_1} = 1 \tag{C.71}$$

Therefore, $N(E) \propto E^{-1}$, and hence, the differential energy distribution becomes:

$$\frac{dN(E)}{dE} \propto E^{-2} \tag{C.72}$$

Obtaining this way the well-known prediction of a power-law energy distribution with spectral index of 2. Note that the derivation is completely independent of the microphysics undergoing in the shock and energization process, it depends just on the ratio of the fluid velocities (sometimes called the compression ratio). Furthermore, this process happens to be faster than the second Fermi one, as the particles crosses the shock at a higher rate than the usual encounters with magnetic clouds.

Bibliography

[1] Enrico Fermi. On the origin of the cosmic radiation. *Phys. Rev.*, 75:1169–1174, 1949.

[2] Katia M. Ferrière. The interstellar environment of our galaxy. *Rev. Mod. Phys.*, 73:1031–1066, Dec 2001.

[3] The Pierre Auger Collaboration. Observation of a large-scale anisotropy in the arrival directions of cosmic rays above 8×10^{18} eV. *Science*, 357(6357):1266–1270, 2017.

[4] A. R. Bell. The acceleration of cosmic rays in shock fronts $- i$. *Monthly Notices of the Royal Astronomical Society*, 182(2):147–156, 1978.

[5] R. D. Blandford and J. P. Ostriker. Particle acceleration by astrophysical shocks. *ApJ*, 221:L29–L32, April 1978.

[6] Ellen G. Zweibel. The microphysics and macrophysics of cosmic rays. *Physics of Plasmas*, 20(5):055501, 2013.

[7] Pasquale Blasi. The origin of galactic cosmic rays. *The Astronomy and Astrophysics Review*, 21(1):70, Nov 2013.

[8] E. Mocchiutti. Direct detection of cosmic rays: through a new era of precision measurements of particle fluxes. *Nuclear Physics B - Proceedings Supplements*, 256-257:161 – 172, 2014. Cosmic Ray Origin - Beyond the Standard Models.

[9] Marius S. Potgieter. Solar modulation of cosmic rays. *Living Reviews in Solar Physics*, 10(1):3, Jun 2013.

[10] Jörg R. Höorandel. A review of experimental results at the knee. *Journal of Physics: Conference Series*, 47(1):41, 2006.

[11] T. K. Gaisser, T. Stanev, and S. Tilav. Cosmic ray energy spectrum from measurements of air showers. *Frontiers of Physics*, 8(6):748–758, Dec 2013.

[12] The IceCube Collaboration, *Fermi*-LAT, MAGIC, *AGILE*, ASAS-SN, HAWC, H.E.S.S., *INTEGRAL*, Kanata, Kiso, Kapteyn, Liverpool Telescope, Subaru, *Swift/NuSTAR*, VERITAS, and VLA/17B-403 teams. Multimessenger observations of a flaring blazar coincident with high-energy neutrino IceCube-170922A. *Science*, 361(6398), 2018.

[13] IceCube Collaboration. Neutrino emission from the direction of the blazar TXS 0506+056 prior to the IceCube-170922A alert. *Science*, 361(6398):147–151, 2018.

[14] T. Jogler and S. Funk. Revealing W51C as a Cosmic Ray Source Using Fermi-LAT Data. *The Astrophysical Journal*, 816(2):100, 2016.

[15] Felix A. Aharonian. Gamma rays from supernova remnants. *Astroparticle Physics*, 43:71 – 80, 2013. Seeing the High-Energy Universe with the Cherenkov Telescope Array - The Science Explored with the CTA.

[16] Damiano Caprioli. Cosmic-ray acceleration in supernova remnants: non-linear theory revised. *Journal of Cosmology and Astroparticle Physics*, 2012(07):038, 2012.

[17] Pasquale Blasi. Nonlinear shock acceleration in the presence of seed particles. *Astroparticle Physics*, 21(1):45 – 57, 2004.

[18] Damiano Caprioli, Horace Zhang, and Anatoly Spitkovsky. Diffusive shock re-acceleration. *Journal of Plasma Physics*, 84(3):715840301, 2018.

[19] D. Caprioli and A. Spitkovsky. Simulations of ion acceleration at non-relativistic shocks. i. acceleration efficiency. *The Astrophysical Journal*, 783(2):91, 2014.

[20] Ellen G. Zweibel and Masaaki Yamada. Magnetic reconnection in astrophysical and laboratory plasmas. *Annual Review of Astronomy and Astrophysics*, 47(1):291–332, 2009.

[21] Kazunari Shibata and Tetsuya Magara. Solar flares: Magnetohydrodynamic processes. *Living Reviews in Solar Physics*, 8(1):6, Dec 2011.

[22] Lorenzo Sironi and Anatoly Spitkovsky. Particle acceleration in relativistic magnetized collisionless electron-ion shocks. *The Astrophysical Journal*, 726(2):75, 2011.

[23] Alexander A. Philippov and Anatoly Spitkovsky. Ab initio pulsar magnetosphere: Three-dimensional particle-in-cell simulations of axisymmetric pulsars. *The Astrophysical Journal Letters*, 785(2):L33, 2014.

[24] Dmitri A. Uzdensky and Anatoly Spitkovsky. Physical conditions in the reconnection layer in pulsar magnetospheres. *The Astrophysical Journal*, 780(1):3, 2014.

[25] M. Lyutikov and R. Blandford. Gamma Ray Bursts as Electromagnetic Outflows. *ArXiv Astrophysics e-prints*, December 2003.

[26] Giannios, D. Prompt GRB emission from gradual energy dissipation. *A&A*, 480(2):305–312, 2008.

[27] Ya-Ping Li, Feng Yuan, and Q. Daniel Wang. A magnetohydrodynamic model for multiwavelength flares from sagittarius A* (i): model and the near-

infrared and x-ray flares. *Monthly Notices of the Royal Astronomical Society*, 468(3):2552–2568, 2017.

[28] David Ball, Feryal Özel, Dimitrios Psaltis, Chi-Kwan Chan, and Lorenzo Sironi. The properties of reconnection current sheets in grmhd simulations of radiatively inefficient accretion flows. *The Astrophysical Journal*, 853(2):184, 2018.

[29] G. Ponti, E. George, S. Scaringi, S. Zhang, C. Jin, J. Dexter, R. Terrier, M. Clavel, N. Degenaar, F. Eisenhauer, R. Genzel, S. Gillessen, A. Goldwurm, M. Habibi, D. Haggard, C. Hailey, F. Harrison, A. Merloni, K. Mori, K. Nandra, T. Ott, O. Pfuhl, P. M. Plewa, and I. Waisberg. A powerful flare from Sgr A* confirms the synchrotron nature of the X-ray emission. *Monthly Notices of the Royal Astronomical Society*, 468(2):2447–2468, 2017.

[30] Maxim Lyutikov, Serguei Komissarov, Lorenzo Sironi, and Oliver Porth. Particle acceleration in explosive relativistic reconnection events and crab nebula gamma-ray flares. *Journal of Plasma Physics*, 84(2):635840201, 2018.

[31] A. Lazarian, G. Eyink, E. Vishniac, and G. Kowal. Turbulent reconnection and its implications. *Philosophical Transactions of the Royal Society of London A: Mathematical, Physical and Engineering Sciences*, 373(2041), 2015.

[32] Elisabete M. de Gouveia Dal Pino and Grzegorz Kowal. *Particle Acceleration by Magnetic Reconnection*, pages 373–398. Springer Berlin Heidelberg, Berlin, Heidelberg, 2015.

[33] N.V. Elkina and J. Büchner. A new conservative unsplit method for the solution of the vlasov equation. *Journal of Computational Physics*, 213(2):862 – 875, 2006.

[34] Lorenzo Sironi and Benoît Cerutti. *Particle Acceleration in Pulsar Wind Neb-*

ulae: PIC Modelling, pages 247–277. Springer International Publishing, Cham, 2017.

[35] R. W. Hockney and J. W. Eastwood. *Computer Simulation Using Particles*. IOP, London, 1988.

[36] Charles K. Birdsall and A. Bruce Langdon. *Plasma physics via computer simulation*. Taylor and Francis, New York, 2005.

[37] Charles K. Birdsall and A. Bruce Langdon. *Plasma physics via computer simulation*, page 356. Taylor and Francis, New York, 2005.

[38] J.P. Boris, R.A. Shanny, United States. Office of Naval Research, and Naval Research Laboratory. *Proceedings: Fourth Conference on Numerical Simulation of Plasmas, November 2, 3, 1970*. Naval Research Laboratory, 1972.

[39] K. Yee. Numerical solution of inital boundary value problems involving maxwell's equations in isotropic media. *IEEE Transactions on Antennas and Propagation*, 14:302–307, May 1966.

[40] J P Verboncoeur. Particle simulation of plasmas: review and advances. *Plasma Physics and Controlled Fusion*, 47(5A):A231, 2005.

[41] Anatoly Spitkovsky. Simulations of relativistic collisionless shocks: shock structure and particle acceleration. *AIP Conference Proceedings*, 801(1):345–350, 2005.

[42] O. Buneman. *Computer Space Plasma Physics*, chapter 3, page 67. Terra Scientific Publishing Company, Tokyo, 1993.

[43] S. Peter Gary, Brian J. Anderson, Richard E. Denton, Stephen A. Fuselier, Michael E. McKean, and Dan Winske. Ion anisotropies in the magnetosheath. *Geophysical Research Letters*, 20(17):1767–1770, 1993.

[44] M. E. McKean, D. Winske, and S. P. Gary. Mirror and ion cyclotron anisotropy instabilities in the magnetosheath. *Journal of Geophysical Research: Space Physics*, 97(A12):19421–19432, 1992.

[45] C. F. Kennel and H. E. Petschek. Limit on stably trapped particle fluxes. *Journal of Geophysical Research*, 71(1):1–28, 1966.

[46] Akira Hasegawa. Drift mirror instability in the magnetosphere. *The Physics of Fluids*, 12(12):2642–2650, 1969.

[47] Pokhotelov O. A., Sagdeev R. Z., Balikhin M. A., and Treumann R. A. Mirror instability at finite ion-larmor radius wavelengths. *Journal of Geophysical Research: Space Physics*, 109(A9), 2004.

[48] S. Peter Gary and Martin A. Lee. The ion cyclotron anisotropy instability and the inverse correlation between proton anisotropy and proton beta. *Journal of Geophysical Research: Space Physics*, 99(A6):11297–11301, 1994.

[49] Daniel Verscharen, Sofiane Bourouaine, Benjamin D. G. Chandran, and Bennett A. Maruca. A parallel-propagating alfvénic ion-beam instability in the high-beta solar wind. *The Astrophysical Journal*, 773(1):8, 2013.

[50] Philip A. Isenberg, Bennett A. Maruca, and Justin C. Kasper. Self-consistent ion cyclotron anisotropy-beta relation for solar wind protons. *The Astrophysical Journal*, 773(2):164, 2013.

[51] A. A. Schekochihin, S. C. Cowley, R. M. Kulsrud, M. S. Rosin, and T. Heinemann. Nonlinear growth of firehose and mirror fluctuations in astrophysical plasmas. *Phys. Rev. Lett.*, 100:081301, Feb 2008.

[52] Mario A. Riquelme, Eliot Quataert, and Daniel Verscharen. Particle-in-cell simulations of continuously driven mirror and ion cyclotron instabilities in high beta

astrophysical and heliospheric plasmas. *The Astrophysical Journal*, 800(1):27, 2015.

[53] D. R. Shklyar. On the nature of particle energization via resonant wave-particle interaction in the inhomogeneous magnetospheric plasma. *Annales Geophysicae*, 29(6):1179–1188, 2011.

[54] D.R. Shklyar. Wave–particle interactions in marginally unstable plasma as a means of energy transfer between energetic particle populations. *Physics Letters A*, 375(14):1583 – 1587, 2011.

[55] Shklyar D. R. Energy transfer from lower energy to higher-energy electrons mediated by whistler waves in the radiation belts. *Journal of Geophysical Research: Space Physics*, 122(1):640–655, 2017.

[56] T. H. Stix. *Waves in plasmas.* American Institute of Physics, 1992.

[57] David Campbell Montgomery and Derek A Tidman. *Plasma kinetic theory.* New York : McGraw-Hill, 1964.

[58] R. C. Davidson and Joan M. Ogden. Electromagnetic ion cyclotron instability driven by ion energy anisotropy in high beta plasmas. *The Physics of Fluids*, 18(8):1045–1050, 1975.

[59] Philip A. Isenberg. A self-consistent marginally stable state for parallel ion cyclotron waves. *Physics of Plasmas*, 19(3):032116, 2012.

[60] R. A. Treumann and W. Baumjohann. *Advanced space plasma physics.* London: Imperial College Press, —c1997, 1997.

[61] Matthew W. Kunz, Alexander A. Schekochihin, and James M. Stone. Firehose and mirror instabilities in a collisionless shearing plasma. *Phys. Rev. Lett.*, 112:205003, May 2014.

[62] J G Kirk and R O Dendy. Shock acceleration of cosmic rays - a critical review. *Journal of Physics G: Nuclear and Particle Physics*, 27(7):1589, 2001.

[63] R. Genzel, R. Schödel, T. Ott, A. Eckart, T. Alexander, F. Lacombe, D. Rouan, and B. Aschenbach. Near-infrared flares from accreting gas around the supermassive black hole at the Galactic Centre. *Nature*, 425:934–937, October 2003.

[64] Daniel P. Marrone, James M. Moran, Jun-Hui Zhao, and Ramprasad Rao. An unambiguous detection of faraday rotation in Sagittarius A*. *The Astrophysical Journal Letters*, 654(1):L57, 2007.

[65] G. Witzel, A. Eckart, M. Bremer, M. Zamaninasab, B. Shahzamanian, M. Valencia-S., R. Schödel, V. Karas, R. Lenzen, N. Marchili, N. Sabha, M. Garcia-Marin, R. M. Buchholz, D. Kunneriath, and C. Straubmeier. Source-intrinsic Near-infrared properties of Sgr A*: Total intensity measurements. *The Astrophysical Journal Supplement Series*, 203(2):18, 2012.

[66] G. Witzel, G. Martinez, J. Hora, S. P. Willner, M. R. Morris, C. Gammie, E. E. Becklin, M. L. N. Ashby, F. Baganoff, S. Carey, T. Do, G. G. Fazio, A. Ghez, W. J. Glaccum, D. Haggard, R. Herrero-Illana, J. Ingalls, R. Narayan, and H. A. Smith. Variability Timescale and Spectral Index of Sgr A* in the Near Infrared: Approximate Bayesian Computation Analysis of the Variability of the Closest Supermassive Black Hole. *ArXiv e-prints*, June 2018.

[67] Andrew Chael, Michael Rowan, Ramesh Narayan, Michael Johnson, and Lorenzo Sironi. The role of electron heating physics in images and variability of the galactic centre black hole sagittarius A*. *Monthly Notices of the Royal Astronomical Society*, 478(4):5209–5229, 2018.

[68] F. Aharonian, A. G. Akhperjanian, A. R. Bazer-Bachi, M. Beilicke, W. Benbow, D. Berge, K. Bernlöhr, C. Boisson, O. Bolz, V. Borrel, I. Braun, F. Breitling, A. M. Brown, P. M. Chadwick, L.-M. Chounet, R. Cornils, L. Costamante,

B. Degrange, H. J. Dickinson, A. Djannati-Ataï, L. O. Drury, G. Dubus, D. Emmanoulopoulos, P. Espigat, F. Feinstein, G. Fontaine, Y. Fuchs, S. Funk, Y. A. Gallant, B. Giebels, S. Gillessen, J. F. Glicenstein, P. Goret, C. Hadjichristidis, D. Hauser, M. Hauser, G. Heinzelmann, G. Henri, G. Hermann, J. A. Hinton, W. Hofmann, M. Holleran, D. Horns, A. Jacholkowska, O. C. de Jager, B. Khélifi, S. Klages, N. Komin, A. Konopelko, I. J. Latham, R. Le Gallou, A. Lemière, M. Lemoine-Goumard, N. Leroy, T. Lohse, A. Marcowith, J. M. Martin, O. Martineau-Huynh, C. Masterson, T. J. L. McComb, M. de Naurois, S. J. Nolan, A. Noutsos, K. J. Orford, J. L. Osborne, M. Ouchrif, M. Panter, G. Pelletier, S. Pita, G. Pühlhofer, M. Punch, B. C. Raubenheimer, M. Raue, J. Raux, S. M. Rayner, A. Reimer, O. Reimer, J. Ripken, L. Rob, L. Rolland, G. Rowell, V. Sahakian, L. Saugé, S. Schlenker, R. Schlickeiser, C. Schuster, U. Schwanke, M. Siewert, H. Sol, D. Spangler, R. Steenkamp, C. Stegmann, J.-P. Tavernet, R. Terrier, C. G. Théoret, M. Tluczykont, C. van Eldik, G. Vasileiadis, C. Venter, P. Vincent, H. J. Völk, and S. J. Wagner. Discovery of very-high-energy γ-rays from the Galactic Centre ridge. *Nature*, 439:695–698, February 2006.

[69] HESS Collaboration, A. Abramowski, F. Aharonian, F. A. Benkhali, A. G. Akhperjanian, E. O. Angüner, M. Backes, A. Balzer, Y. Becherini, J. B. Tjus, and et al. Acceleration of petaelectronvolt protons in the Galactic Centre. *Nature*, 531:476–479, March 2016.

[70] N. I. Shakura and R. A. Sunyaev. Black holes in binary systems. Observational appearance. *A&A*, 24:337–355, 1973.

[71] Quataert Eliot. Radiatively inefficient accretion flow models of sgr A*. *Astronomische Nachrichten*, 324(1):435–443, 2003.

[72] Feng Yuan and Ramesh Narayan. Hot accretion flows around black holes. *Annual Review of Astronomy and Astrophysics*, 52(1):529–588, 2014.

[73] D. B. Melrose. *Instabilities in Space and Laboratory Plasmas*. Cambridge University Press, 1986.

[74] F. K. Baganoff, Y. Maeda, M. Morris, M. W. Bautz, W. N. Brandt, W. Cui, J. P. Doty, E. D. Feigelson, G. P. Garmire, S. H. Pravdo, G. R. Ricker, and L. K. Townsley. Chandra x-ray spectroscopic imaging of sagittarius A* and the central parsec of the galaxy. *The Astrophysical Journal*, 591(2):891, 2003.

[75] Jonathan C. McKinney, Alexander Tchekhovskoy, and Roger D. Blandford. General relativistic magnetohydrodynamic simulations of magnetically choked accretion flows around black holes. *Monthly Notices of the Royal Astronomical Society*, 423(4):3083–3117, 2012.

[76] S M Ressler, E Quataert, and J M Stone. Hydrodynamic simulations of the inner accretion flow of sagittarius A* fuelled by stellar winds. *Monthly Notices of the Royal Astronomical Society*, 478(3):3544–3563, 1753.

[77] Feng Yuan, Eliot Quataert, and Ramesh Narayan. Nonthermal electrons in radiatively inefficient accretion flow models of sagittarius A*. *The Astrophysical Journal*, 598(1):301, 2003.

[78] L. H. S. Kadowaki, E. M. de Gouveia Dal Pino, and C. B. Singh. The role of fast magnetic reconnection on the radio and gamma-ray emission from the nuclear regions of microquasars and low luminosity agns. *The Astrophysical Journal*, 802(2):113, 2015.

[79] Mario A. Riquelme, Eliot Quataert, Prateek Sharma, and Anatoly Spitkovsky. Local two-dimensional particle-in-cell simulations of the collisionless magnetorotational instability. *The Astrophysical Journal*, 755(1):50, 2012.

[80] L.D. Landau and E.M. Lifshitz. *Mechanics*. Butterworth-Heinemann, 1976.

[81] Mario Vietri. *Foundations of high-energy astrophysics*. Theoretical Astrophysics. University Of Chicago Press, illustrated edition, 2008.

[82] Claus Grupen. *Astroparticle Physics*. Springer-Verlag Berlin Heidelberg, 1st edition, 2005.

[83] M. Vereecken and D. Ryckbosch. Schokacceleratie van kosmische stralen in galactische en extragalactische bronnen. Master's thesis, Ghent University, the Netherlands, 2014.

[84] Malcolm S. Longair. *High Energy Astrophysics*. Cambridge University Press, 3rd edition, 2011.